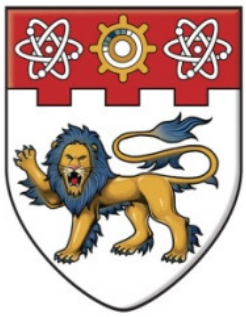

NANYANG TECHNOLOGICAL UNIVERSITY

APATITE ELECTROLYTES:

DESIGN, SYNTHESIS AND MODELING

STEVIN SNELLIUS PRAMANA

SCHOOL OF MATERIALS SCIENCE AND ENGINEERING

2011

APATITE ELECTROLYTES: DESIGN, SYNTHESIS AND MODELING

STEVIN SNELLIUS PRAMANA

School of Materials Science and Engineering

A thesis submitted to the Nanyang Technological University
in partial fulfillment of the requirement for the degree of
Doctor of Philosophy

2011

Acknowledgements

First and foremost, I would like to thank my Lord and Savior, Jesus Christ for giving me life and enabling me to persistently perform my studies. I would like to express my deepest gratitude to my research advisors Assoc. Prof. Tim White and Asst. Prof. Madhavi Srinivasan for their encouragement, guidance and insight throughout my postgraduate studies. In addition, I would also like to thank Prof. Christian Kloc and Asst. Prof. Dong Zhili for their suggestion in the Thesis Advisory Committee.

I am grateful to Dr. Peter R. Slater for his support in the impedance testing at the University of Surrey. In addition, I wish to thank Dr. Cristiano Ferraris, Dr. Tom Baikie, Dr. Martin Schreyer and Dr. Wim Klooster for their assistance in the electron microscopy and diffraction analysis.

Many thanks to the staff of the Facility for Analysis, Characterization, Testing and Simulation (FACTS) – Ms. Jun Guo, Ms. Irene Heng and Mr. Sithu Aung and my colleagues – Dr. Suo Hon Lim, Mr. Hou Ran Low and Ms. Eileen Goh – whose help and encouragement I always appreciate. Finally I thank my family and wife for their continuous prayer and support throughout my PhD studies.

This work was supported through A*STAR SERC Grant 082 101 0021 "*Optimization of Apatite Anion Sublattices in Solid Oxide Fuel Cell Electrolytes*".

To God be the glory!

Abstract

The crystal chemistries of a range of germanate, silicate and rhenate apatites were studied as potential electrolytes for solid oxide fuel cells (SOFCs). While these compounds are often described as complying with the composition $A_{10}(BO_4)_6O_2$ (A = rare earth, alkali earth, alkali and B = germanium, silicon, transition metals), the character of apatite electrolytes is far more interesting. Indeed, it is the underlying complexity and flexibility of these substances that endows them with such promise as ion conductors. In this thesis, the nature of "hybrid" apatites is examined, and the critical role of extrastoichiometric oxygen associated in BO_5 units for facilitating high conductivity with low activation energy considered. Following this approach, a taxonomy of polymorphic and polysomatic apatites is devised that provides a basis for the rationale design of new electrolytes and the optimization of performance. Apatites can be synthesized in various ways, including solid state sintering, sol-gel methods and hydrothermal reactions; but the former is favored since large quantities are readily fabricated for division and multi-technique characterization. X-ray, neutron and electron diffraction were employed to refine crystal structures and locate "interstitial" oxygen, supported by spectroscopic and microscopic methods to identify defects and recognize superlattices. In this manner, correlations between ionic conductivity and crystal chemistry were established.

It was shown that extrastoichiometric oxygen, introduced by selective altervalent replacements of A or B species, plays a more important role in electrolyte performance than vacancies; this is in contrast to the more extensively studied perovskite and fluorite electrolytes where vacancies prove essential. However, the location, abundance and migration of oxygen remains controversial. In this study, these questions were addressed by directly observing oxygen in triclinic $P\bar{1}$ $La_{10}Ge_6O_{27}$ apatite using neutron diffraction and Fourier difference methods to locate the lowest energy position of the mobile entity. Supplementary X-ray absorption and infrared spectroscopies found the coordination of some GeO_4 tetrahedra were transformed to GeO_5 trigonal bipyramids with $La_{10}(GeO_4)_5(GeO_5)O_2$ representing the complete crystal chemical formula; this was the first example of an $A_{10}[(BO_4)_{5+x}(BO_5)_{1-x}]O_2$ hybrid to be described. This compound transformed from

triclinic → monoclinic → hexagonal polymorphs with increasing temperature. In addition, doping with alkaline earth elements (*AE*) created pseudomorphic series such as $[La_{10-x}AE_x][(GeO_4)_{5+x/2}(GeO_5)_{1-x/2}][O_2]$ (AE = Sr, $0 < x < 2$) and $[La_{10-x}AE_x][(GeO_4)_6][O_2][H_\delta]$ (AE = Sr, $2 < x < 5.32$). The introduction of calcium improved ionic conductivity and $La_9Ca(GeO_4)_{5.5}(GeO_5)_{0.5}O_2$ proved optimal with an ideal balance between interstitial oxygen concentration and lowered activation energy for diffusion. These crystallochemical modifications were summarized using the polysomatic nomenclature apatite-(*ABX*)-N*S* where *AB* are the most abundant atoms on these sites, *X* = O for electrolytes, N is the number of layers in the crystallographic repeat, and *S* is the lattice symmetry. For example, $La_{10}Ge_6O_{27}$ at room temperature can be described as apatite-(LaGeO)-2*A*, but above 700°C transforms to apatite-(LaGeO)-2*M* and finally > 800°C apatite-(LaGeO)-2*H* appears. Further crystallographic investigations of sodium-doped apatites, $La_{9.33-x/3}Na_x(SiO_4)_6O_2$ using anomalous scattering of synchrotron X-ray diffraction provided high resolution powder diffraction patterns to explore the possibility of small departures from the hexagonal 2*H* metric and allowed the La/Na partitioning coefficients over the A^{I} and A^{II} sites to be determined.

As BO_5 is the unit principally responsible for high conduction, the fully oxidized apatite $Ba_{10}[(ReO_5)_6]O_2$ was investigated. Although the amount of potentially labile oxygen is five times more abundant in the rhenate, compared to the germanate $La_{10}(GeO_4)_5(GeO_5)O_2$, conductivity was comparable, because the oxygen is more tightly bound to the *B* cation and not readily transported. While the principle of introducing high valence *B* cations to provide a framework reservoir of oxygen appears sound, further adjustment of interstitial oxygen content, lattice symmetry and activation energy will be required to fabricate a superior solid ionic conductor.

It is axiomatic that material functionalities derive from crystal structure and chemistry, and that a thorough understanding of apatite phase relationships and transformations should lead to novel hybrid architectures. Supported by comprehensive characterization tools, the studies reported here provide a scaffold for tailoring apatites with high ionic conductivity. Future investigations should not only seek to expand the selection of chemistries with enhanced oxygen conductivities, but identify inert compositions to minimize reactions with cathode and anode materials. A

fundamental question concerns the prevalence of nanochemical domains, and their possible enhancement or attenuation of oxygen migration; the multiple space groups reported for apatites of notionally the same composition suggest that such features may be present. However, electron microscopy is often of limited use to resolve this matter due to disruption of the structures in high electron fluxes. Alternative approaches may include cryo-microscopy, to minimize the introduction of radiation artifacts, and greater efforts to grow large “single” crystals, where detection of inhomogeneities should prove simpler.

Publications

1 S. S. Pramana, W. T. Klooster and T. J. White, A taxonomy of apatite frameworks for the crystal chemical design of fuel cell electrolytes, *J. Solid State Chem.*, 2008, **181**, 1717-1722.

2 T. Baikie, S. S. Pramana, C. Ferraris, Y. Huang, E. Kendrick, K. S. Knight, Z. Ahmad and T. J. White, Polysomatic apatites, *Acta Crystallogr B.*, 2010, **66**, 1-16.

3 S. S. Pramana, W. T. Klooster and T. J. White, Framework 'interstitial' oxygen in $La_{10}(GeO_4)_5(GeO_5)O_2$ apatite electrolyte, *Acta Crystallogr. B*, 2007, **63**, 597-602.

4 S. S. Pramana, T. J. White, M. K. Schreyer, C. Ferraris, P. R. Slater, A. Orera, T. J. Bastow, S. Mangold, S. Doyle, T. Liu, A. Fajar, M. Srinivasan and T. Baikie, Pseudomorphic $2A \rightarrow 2M \rightarrow 2H$ phase transitions in lanthanum strontium germanate electrolyte apatites, *Dalton Trans.*, 2009, 8280-8291.

5 S. S. Pramana, T. Baikie, E. Kendrick, M. K. Schreyer, P. R. Slater, and T. J. White, Crystal chemistry and optimization of conductivity in 2*A*, 2*M* and 2*H* alkaline earth lanthanum germanate oxyapatite electrolyte polymorphs, *Solid State Ionics*, 2010, **181**, 1189-1196.

6 T. Baikie, S. T. Ooi, S. S. Pramana, Z. Ahmad, P. Yang, M. Avdeev and T. J. White, Resonant powder X-ray diffraction and neutron diffraction study of $La_{9.33-x/3}Na_x(SiO_4)_6O_2$ ($0 \leq x \leq 1$) and $La_{9-x}Na_{1+x}(SiO_4)_6O_{2-2x}(OH)_{2x}$ ($0 \leq x \leq 1$) apatites, *J. Solid State Chem.*, 2010, in preparation.

7 S. S. Pramana, C. Ferraris, M. K. Schreyer, P. R. Slater, T. Baikie, B. Toby, K. Knight, M. Srinivasan and T. J. White, Rhenium apatites: a new class of fuel cell electrolyte, *J. Mater. Chem.*,2010, in preparation.

Table of Contents

List of Tables

List of Figures

List of Abbreviations

AC	Alternating Current
AE	Alkaline Earth
BV	Bond Valence
CBED	Convergent Beam Electron Diffraction
CHP	Combined Heat and Power
CPE	Constant Phase Element
C_s	Spherical Aberration
E_a	Activation Energy
EXAFS	Extended X-ray Absorption Fine Structure
FTIR	Fourier Transformed Infra Red
FWHM	Full Width at Half Maximum
GULP	General Utility Lattice Program
HRPD	High Resolution Powder Diffractometer
HRTEM	High Resolution Transmission Electron Microscopy
MAD	Multiple Wavelength Anomalous Diffraction
MAS	Magic Angle Spinning
ND	Neutron Diffraction
NMR	Nuclear Magnetic Resonance
RE	Rare Earth
SAED	Selected Area Electron Diffraction
SOFC	Solid Oxide Fuel Cell
TEM	Transmission Electron Microscopy
TGA	Thermogravimetric Analysis
TOF	Time-of-Flight
XANES	X-ray Absorption Near Edge Structure
XAS	X-ray Absorption Spectroscopy
XRD	X-ray Diffraction
YSZ	Yttria Stabilized Zirconia
Z	Atomic Number

Chapter 1

Introduction

1.1 Problem Statement

In common with other electrochemical devices, the solid oxide fuel cell (SOFC) is composed of an anode, electrolyte and a cathode. For optimal performance the cell requires an electrolyte with high oxygen transport that remains an ionic conductor in both oxidizing and reducing environments.[1] Oxygen migrates *via* bulk and grain boundary conduction, however determining the precise nature of ion diffusion is not resolved easily, with differentiation further complicated when ionic and electronic conduction occur simultaneously.

Apatite structures are promising SOFC electrolytes,[2,3] in addition to finding potential and actual applications for the remediation of radioactive wastes,[4] catalysis,[5] prostheses[6,7] and brilliant non-toxic dyes.[8] As electrolytes, rare earth silicate[2,9,10] / germanate[11-14] apatites are attractive because they show high oxide conductivity (typically 0.03 Scm^{-1} at 800°C) and low activation energy (1 eV) in all atmospheres.[3] Apatites can be synthesized by solid-state,[14-17] sol-gel[18-20] and hydrothermal reactions,[21-24] but whatever the preparative route, controlling the final composition is difficult. This is a consequence of apatites possessing zeolitic character where large one-dimensional tunnels respond flexibly to chemical substitutions;[25] for example, oxy-, hydroxy- and carbonated-apatite can crystallize from notionally the same starting materials through variation in redox conditions, humidity and temperature.[26] Furthermore, obtaining phase pure, polycrystalline apatite (> 99%) is challenging, especially for more complex chemistries, and tailoring synthesis parameters remains an incompletely developed aspect of the materials science for this group.[17,27]

The crystal chemical formula for conventional hexagonal $P6_3/m$ apatites is $[A^{I}_4][A^{II}_6][(BO_4)_6][X]_2$ where A and B are larger and smaller cations, respectively and X is an anion or oxy-anion. The primary channel is composed of face-sharing $A^{I}O_6$ metaprisms that are corner-connected to BO_4 tetrahedra, with twisting of the triangular metaprism faces allowing adjustment of the tunnel dimensions. From this prototype structure, apatite evolves into more complex varieties where BO_4 is oxidized to BO_5 or reduced to BO_3 in response to oxygen fugacity and to satisfy bond valence requirements.[28] This may be accompanied by symmetry modification from

hexagonal ($P6_3/m$, $P6_3$, $P\bar{6}$, $P6_3cm$), through trigonal ($P\bar{3}$), orthorhombic ($Pnma$), monoclinic ($P2_1/m$, $P2_1/b$, $P2_1$) and triclinic ($P\bar{1}$).[25] It follows that the functionality of these compounds can be adapted by tuning the crystal structure.

Conductivity measurements and theoretical studies have shown that oxygen mobility in apatite is anisotropic, but intra-tunnel oxygen transport has been studied almost exclusively.[29] However, significant oxygen ion conduction perpendicular to the channels in single crystals of $Pr_{9.33}(SiO_4)_6O_2$, $Nd_{9.33}(SiO_4)_6O_2$ and $Sm_{9.33}(SiO_4)_6O_2$ apatites have been reported.[30] Hence, developing a comprehensive description of oxygen diffusion through the electrolyte will provide an essential underpinning for the delivery of fuel cell longevity and reliability.

1.2 Objectives and Scope

The objectives of this research are to:

(i) better understand the generic relationships between ionic conductivity and apatite crystal chemistry; and

(ii) optimize the performance of lanthanum germanate, lanthanum silicate and barium rhenate apatite electrolyte systems.

The scope of this work includes:

(I) Establishing a map of topological distortions to identify structural modifications which favor oxygen conduction through examining:

(I-i) Descriptions that emphasize $A^{I}O_6$ metaprism twisting and BO_4 tetrahedral tilting of the $A_{10}(BO_4)_6X_2$ aristotype;

(I-ii) Oxidized apatites: $A_{10}(BO_5)_6X_2$;

(I-iii) Reduced apatites: $A_{10}(BO_3)_6X_2$;

(I-iv) Hybrid apatites: $A_{10}(BO_4)_{6-x}(BO_5)_xX_2$, $A_{10}(BO_4)_{6-x}(BO_3)_xX_2$ and $A_{10}(BO_5)_{6-x}(BO_3)_xX_2$; and

(I-v) Polysomatic apatites: $A_{5N}B_{3N}O_{9N+6}X_{N\delta}$.

(II) Apatite fabrication through a variety of routes including:

(II-i) Solid state sintering where starting oxides are mixed stoichiometrically before high temperature treatment and extended reaction times to obtain high yield;

(II-ii) Sol-gel methods to obtain nano-crystalline powders *via* low temperature reactions, where alkoxides are often used as a chemical precursor; and

(II-iii) Hydrothermal reactions to produce large single crystals in autoclaves at temperatures ≤ 180°C. In this case, the starting materials must be soluble in aqueous alkaline or acidic media.

(III) Comprehensive characterization by:

(III-i) Powder diffraction using fixed wavelength synchrotron and laboratory X-ray diffraction (XRD), and fixed wavelength and time-of-flight neutron diffraction (ND) that in combination allow the determination of lattice parameters, symmetry, occupancy and interstitial oxygen positions;

(III-ii) Transmission electron microscopy (TEM) to collect nano-scale information by selected area electron diffraction (SAED), convergent beam electron diffraction (CBED) and high resolution transmission electron microscopy (HRTEM) and so examine defect abundance, confirm crystal structures, and validate symmetry; and

(III-iii) Spectroscopic methods where coordination and bonding are probed by X-ray absorption spectroscopy (XAS), Fourier-transformed infrared spectroscopy (FTIR) and nuclear magnetic resonance (NMR) spectrometry.

(IV) Conductivity measurements of sintered pellets by impedance analysis to measure oxygen ion mobility.

(V) Atomistic simulations of apatite structures and prediction of ionic pathways using semi-empirical methods in which:

(V-i) An inter-atomistic potential calculation was used to model the minimum lattice energy and defect structures; and

(V-ii) Bond valence summation was performed to map the static energy landscape.

1.3 Dissertation Overview

The Introduction (Chapter 1) provides the research justification and establishes the objectives and scope that are directed towards a deeper understanding of apatite design and enhanced electrolyte performance.

Chapter 2 reviews the state-of-the-art for solid oxide fuel cell electrolytes, details the crystallochemical flexibility of the apatite family and compares the conduction mechanisms in nonstoichiometric apatites. The taxonomy of apatite frameworks and introduces polymorphic and polysomatic nomenclature is mapped. The space group hierarchy from hexagonal to triclinic symmetry relates the degrees of freedom for $A^{I}O_6$ metaprism twisting with BO_4 tetrahedral tilting. This new systematization provides a rationale for tailoring apatite crystal chemistry – as neutral, oxidized, reduced and hybrid apatites – to optimize oxygen ion mobility.

Chapter 3 describes the synthesis and a suite of characterization techniques for studying electrolytes with particular emphasis on their strengths and limitations for probing crystallographic, mechanistic and functional aspects. Finally, atomistic modeling is discussed as a method of computing lattice energy, defect structures and ion migration pathways.

Chapter 4 experimentally examines the importance of super- or sub-oxygen stoichiometry to attain high conductivity. This was accomplished by tailoring through adjustment of framework and tunnel charge compensation mechanisms. To this end, the following compounds were synthesized:

- $La_{10}Ge_6O_{27}$ containing excess oxygen (Section 4.1);
- $La_{10-x}AE_xGe_6O_{27-x/2}$ (AE = Ca, Sr, Ba) containing excess oxygen and/or vacancy (Sections 4.2 and 4.3);
- $La_{10-x}Na_xSi_6O_{27-x}$ containing excess oxygen and/or vacancy (Section 4.4); and
- $(Ba/Sr)_{10}Re_6O_{32}$, highly oxidized apatite (Section 4.5).

Section 4.1 describes for the first time the direct observation of interstitial oxygen in apatite electrolytes using neutron diffraction and Fourier difference mapping of

oxidized lanthanum germanate $La_{10}Ge_6O_{27}$. In this manner, the oxygen diffusion pathway is correlated with inter-tunnel migration to explain the substantial conduction through the tunnel walls that was reported in single crystal apatites. Polymorphic phase transformations in $La_{10}Ge_6O_{27}$ are examined as a function of temperature and correlated with inflections in ionic conductivity.

Section 4.2 explores pseudomorphic phase transformations in Sr-doped lanthanum germanate apatite and the temperature dependence of polymorphic transitions. The bonding environment around Ge was probed by XAS and FTIR to verify the existence of a GeO_5 polyhedron. In addition, nanoscale homogeneity, ionic conductivity and proton incorporation are also highlighted.

Section 4.3 considers alkaline earth (particularly Ca and Ba) replacement of lanthanum in germanate electrolytes and the effect on crystal structure and ionic conductivity. The variation in A^{I}/A^{II} partitioning of Ca, Sr and Ba was determined by structure refinement with the consequences for oxygen mobility related to changes in the relative size of framework to tunnel. These results are amplified by atomistic modeling of preferred defect structures. It is shown that $La_9AEGe_6O_{26.5}$ delivers enhanced conductivity by providing the optimal combination of activation energy and extrastoichiometric oxygen content.

Section 4.4 describes sodium substituted lanthanum silicate apatites as analyzed by multiple wavelength anomalous X-ray scattering obtained from synchrotron XRD to show that La/Na partitioning over the A^{I}/A^{II} sites is compositionally dependent. Two crystallochemical series are established – $La_{9.33-x/3}Na_x(SiO_4)_6O_2$ ($0 \leq x \leq 1$) and $La_{9-y}Na_{1+y}(SiO_4)_6O_{2-2y}(OH)_{2y}$ ($0 \leq y \leq 1$). While these materials may not be suitable as electrolytes, insight of the proton incorporation and the impact on conductivity were considered.

Section 4.5 resolves the crystal structure of a barium rhenate apatite $Ba_{10}(ReO_5)_6O_2$ electrolyte by SAED and synchrotron powder XRD, and shows it exists as a commensurate supercell, with the rational q vector. Preliminary results show this new class of ion conductor to have relatively high ionic conductivity and are worthy of further development.

Chapter 5 concludes the whole project and proposes future apatite designs that build upon the thorough understanding of the apatite materials class and their phase transformations developed in this thesis. Suggestions are made to exploit these new concepts through addressing correlations of crystal chemistry, ion migration mechanisms and device fabrication.

1.4 Findings and Outcomes

This research leads to several novel outcomes by:

(i) establishing a new descriptive model of apatite taxonomy including hybrids, polymorphs and polysomes which can guide the design of functional electrolytes;

(ii) direct observation of interstitial oxygen in the apatite framework using neutron diffraction *via* Fourier analysis;

(iii) formulating novel apatite oxide ion conductors and describing inter-tunnel and intra-tunnel conduction mechanisms; and

(iv) developing synthesis procedures that yield germanate, silicate and rhenate apatites of high purity to improve conduction.

Chapter 2

Literature Review

2.1 Solid Oxide Fuel Cells

At present, the principal sources of electrical power are fossil fuels including petroleum (36.6%), dry natural gas (23.0%) and coal (27.2%). Because these resources are finite, polluting and contribute to global warming, nuclear, geothermal and wind technologies (13.2%)[31] are becoming increasingly attractive and viable. These considerations are also driving the development of high temperature solid oxide fuel cells (SOFCs) that are electrochemical devices where hydrogen and oxygen react and convert chemical to electrical energy. Designing SOFCs requires a multidisciplinary approach considering a range of parameters, the most important being, electrical conduction, ionic migration, bulk and surficial chemical reactions, heat transfer and materials compatibility. Regardless of the geometrical configuration (planar or tubular), a SOFC is always composed of porous electrodes (anode and cathode), a dense electrolyte, an anodic and cathodic gas channel and two current collectors (Figure 1).[32-35] The operating temperatures for these devices range from as low as ambient to as high as 1000°C largely determined by the electrolyte. When high temperatures are employed, there is a potential to combine heat and power (CHP) to create hybrid systems, especially for inclusion in built environs that presently consume two-thirds of all electricity produced.[33]

The unique advantages of SOFCs over other types of fuel cells are:[34-38]

- the use of non-noble metals and other low-cost materials for large-scale cell component fabrication;
- tolerance to fuel impurities which allows exploitation of less costly and more widely available hydrocarbon fuels to bridge the hydrogen infrastructure gap through internal reforming;
- power-scaling from watts (W) to megawatts (MW) to suit different applications;
- minimal environmental-impact because of ‘near zero’ pollutant emission; and
- a potential life-cycle of 40,000 – 80,000 hours.

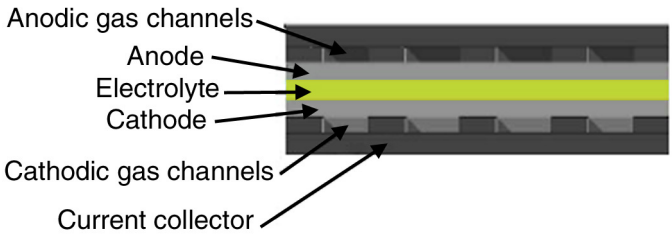

Figure 1 A schematic representation of a flat panel SOFC [Adapted from Bove and Ubertini[39]].

The electrochemical reactions in SOFCs with gaseous H_2 and O_2 (Figure 2) are:

Anodic Reaction

$$H_2 + O^{2-} \rightarrow H_2O + 2\,e^- \quad \textbf{(1)}$$

Cathodic Reaction

$$\tfrac{1}{2}\,O_2 + 2\,e^- \rightarrow O^{2-} \quad \textbf{(2)}$$

Overall Reaction

$$H_2 + \tfrac{1}{2}\,O_2 \rightarrow H_2O \quad \textbf{(3)}$$

The key requirements of the solid electrolyte are good ionic conduction to limit cell impedance, and the absence of electronic conduction, to minimize leakage currents; hence, controlling the mobility of ionic and electronic charge carriers is critical.[34,40] Typically, metals such as Ni, Co, Ru and Pt are used in a reducing environment at the anode, while on the cathode side, doped $LaMnO_3$ perovskite and La-Sr-cobaltite are commonly employed.[1]

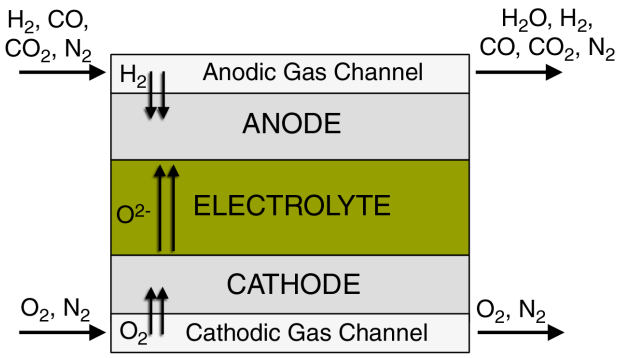

Figure 2 Gas fluxes inside a SOFC [Adapted from Bove and Ubertini[39]].

The benchmark intermediate temperature SOFC electrolyte is the cubic fluorite-phase yttria-stabilized zirconia (YSZ) where conduction is improved by increasing the concentration of oxygen vacancies ($2Zr^{4+} + O^{2-} \rightarrow 2Y^{3+} + \square_{O^{2-}}$) ($\sigma$ = 0.04 Scm^{-1} at 800°C). The optimum concentration of yttria is ~ 8 mol% because at higher levels, defect mobility and conductivity are reduced.[41] The improved conductivity of scandia-stabilized zirconia (0.05 Scm^{-1} at 800°C)[42] is attributed to the smaller lattice mismatch between Zr^{4+} (effective ionic radii = 0.84 Å for VIII coordination) and Sc^{3+} (0.87 Å) compared with Y^{3+} (1.019 Å)[43] resulting in less structural strain and increased mobility. Since the solid electrolyte is in contact with the anode and cathode, several interconnect issues arise. For example, a combination of YSZ electrolyte and $La_{1-x}Sr_xMnO_3$ (LSM) cathode can, depending on the Sr content, result in the formation of $La_2Zr_2O_7$ ($x \leq 0.2$),[44,45] $SrZrO_3$ ($0.3 \leq x \leq 0.4$)[46] or a combination of these phases ($x \geq 0.5$).[44-46] These reaction products detract from the performance of fuel cells because of their lower ionic conductivities.[47]

Compared to zirconia, ceria has higher conductivity particularly at lower temperatures ($\sigma_{(CeO_2)_{0.8}(GdO_{1.5})_{0.2}}$ = 0.09 Scm^{-1} at 800°C),[48] but there is significant electronic conduction for reduced oxygen partial pressures.[40,49] To minimize crystallographic stress and thereby increase ionic conductivity, ceria can be doped with rare-earth metal ions having small size mismatch such as gadolinium and samarium[50] (effective ionic radii for Ce^{3+} (VIII) = 1.143 Å, Gd^{3+} (VIII) = 1.053 Å, Sm^{3+} (VIII) = 1.079 Å)[43]. Although the stability of ceria due to $Ce^{4+} \rightarrow Ce^{3+}$ conversion is inferior to zirconia, the chemical stability of the former with the cathode materials $La_{1-x}Sr_xMnO_3$ (LSM), $La_{1-x}Sr_xCoO_3$ (LSC), $La_{1-x}Sr_xFeO_3$ (LSF), $La_{1-x}Sr_xCo_{1-y}Fe_yO_3$ (LSCF), $LaNi_{1-x}Fe_xO_3$ (LNF) is superior.[51,52] Ceria can also be used as an interlayer between YSZ and the cathode to prevent reaction. Since YSZ and ceria possess the same cubic fluorite structure, inter-diffusion between these phases is deleterious as it promotes the ordering of cations with a reduction in conductivity.[34,53]

Perovskite-type lanthanum gallate ($LaGaO_3$) can be doped with strontium and magnesium to create $La_{1-x}Sr_xGa_{1-y}Mg_yO_3$ (LSGM) with improved low-temperature oxide ion conduction.[54] The conductivity of LSGM depends on dopant concentration[55-58] and is maximized for $La_{0.85}Sr_{0.15}Ga_{0.8}Mg_{0.2}O_3$ (0.15 Scm^{-1} at 800°C)

and $La_{0.8}Sr_{0.2}Ga_{0.85}Mg_{0.15}O_3$ (0.15 Scm^{-1} at 800°C).[55] To increase the conductivity further, a small amount of transition metal dopants such as cobalt and iron can be introduced with the former most effective ($\sigma_{La_{0.8}Sr_{0.2}Ga_{0.8}Mg_{0.15}Co_{0.05}O_3}$ = 0.16 Scm^{-1} at 800°C).[34] However, electron/hole conductivity increases simultaneously leading to an overall degradation of fuel cell performance.[55,56] Table 1 compares various electrolyte conductivities at 800°C.

Table 1 Conductivity for selected electrolytes at 800°C.

Material	Conductivity (S cm^{-1})
Zirconia-types	
8YSZ [41]	$4.3x10^{-2}$
10YSZ [59]	$2.0x10^{-2}$
10ScSZ [42]	$5.2x10^{-2}$
10CaSZ [59]	$9.3x10^{-4}$
9InSZ [60]	$9.3x10^{-3}$
8YbSZ [61]	$6.1x10^{-2}$
Ceria-types	
20GdCeO2 [48]	$9.0x10^{-2}$
$10GdCeO_2$ [62]	$4.9x10^{-2}$
$10YbCeO_2$ [63]	$2.3x10^{-2}$
Lanthanum gallate-types	
$La_{0.85}Sr_{0.15}Ga_{0.8}Mg_{0.2}O_3$ [55]	$1.5x10^{-1}$
$La_{0.8}Sr_{0.2}Ga_{0.85}Mg_{0.15}O_3$ [55]	$1.5x10^{-1}$
$La_{0.9}Sr_{0.1}Ga_{0.8}Mg_{0.2}O_3$ [56]	$1.0x10^{-1}$
$La_{0.8}Sr_{0.2}Ga_{0.8}Mg_{0.15}Co_{0.05}O_3$ [34]	$1.6x10^{-1}$
$La_{0.9}Sr_{0.1}(Ga_{0.8}Mg_{0.2})_{0.95}Co_{0.05}O_3$ [58]	$9.3x10^{-2}$
Apatite-types	
$La_{10}(GeO_4)_5(GeO_5)O_2$ [64]	$3.0x10^{-2}$
$La_8Sr_2(GeO_4)_6O_2$ [64]	$3.0x10^{-5}$
$La_6Sr_4(GeO_4)_6O$ [64]	$1.7x10^{-6}$
$La_{9.33}(GeO_4)_6O_2$ [65]	$1.0x10^{-2}$
$La_{9.33}(SiO_4)_6O_2$ [65]	$2.0x10^{-3}$
$La_{9.5}(GeO_4)_{5.5}(AlO_4)_{0.5}O_2$ [66]	$1.6x10^{-1}$

2.2 Apatite Crystallographic Family

A phase diagram of La_2O_3 – SiO_2 shows that $La_{14}Si_9O_{39}$ or best described as apatite $La_{9.33}Si_6O_{26}$, La_2SiO_5 and $La_2Si_2O_7$ are possible to crystallize depending on the temperature and composition.[67,68] Figure 3 shows the phase diagram of Nd_2O_3 – SiO_2 surrounding the apatite $Nd_{9.33}(SiO_4)_6O_2$.[69] In the analogue lanthanum germanate system, the phase diagram information is more limited and the possible phases in RE_2O_3 (RE = La, Nd and Er) – GeO_2 and Y_2O_3 – GeO_2 are RE_4GeO_8, RE_2GeO_5, $RE_2Ge_2O_7$, $RE_2Ge_3O_9$ and $RE_{9.33}Ge_6O_{26}$.[12,17,70-73]

Apatite can be crystallographically described as an $[A^{I}_4][A^{II}_6][(BO_4)_6][X]_2$ compound that is an anion-stuffed derivative of the $P6_3/mcm$ Mn_5Si_3 alloy type.[74] Apatite has zeolitic character being constructed of an $A^{I}_4(BO_4)_6$ framework that circumscribes [001] channels that adjust in diameter to accommodate the $A^{II}_6X_2$ component. The bore of this conduit is controlled by (001) twisting of the triangular faces of the $A^{I}O_6$ metaprisms through an angle ϕ.[25,75] In this manner, the BO_4 tetrahedra remain essentially undistorted (Figure 4). While $5^o \leq \phi \leq 24^o$ is commonly encountered,[25,75] larger twist angles (as in $Ca_{10}(VO_4)_6F_2$ for example)[76] require the tetrahedron to rotate about $[100]_{hex}$ to furnish acceptable bond valence sums, and in so doing, the lattice symmetry is reduced from hexagonal to triclinic.

White *et al.*[25,75] classified the apatites in different genus as $A_{10}(BO_4)_6X_2$, $A_{10}(BO_3)_6X_2$ and $A_{10}(BO_5)_6X_2$, which will be further elaborated in Section 2.3. In addition, the metaprism twist angle ϕ is a key apatite variable such that larger rotations constrict the tunnel when either the size or abundance of the A^{II} and X atoms decreases, and correlates experimentally derived ϕ with unit cell parameters.[77] Furthermore, possible space groups ($P6_3/m$, $P6_3$, $P\bar{3}$, $P\bar{6}$, $P2_1/m$, $P2_1$ $P6_3cm$ and $Pnma$) in apatite complex chemistries were tabulated according to different atom acceptor sites together with various synthesis routes (solid state, hydrothermal, soft chemistry and sol-gel routes)[25]. Based upon the relationships between space groups the degrees of structural freedom are detailed in Section 2.3.3.

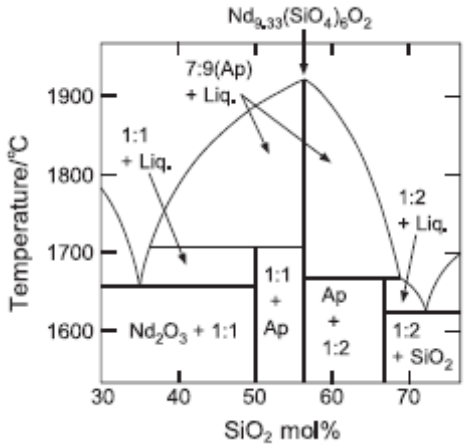

Figure 3 Phase diagram of Nd_2O_3 – SiO_2 [Taken from Higuchi *et al.*[69]].

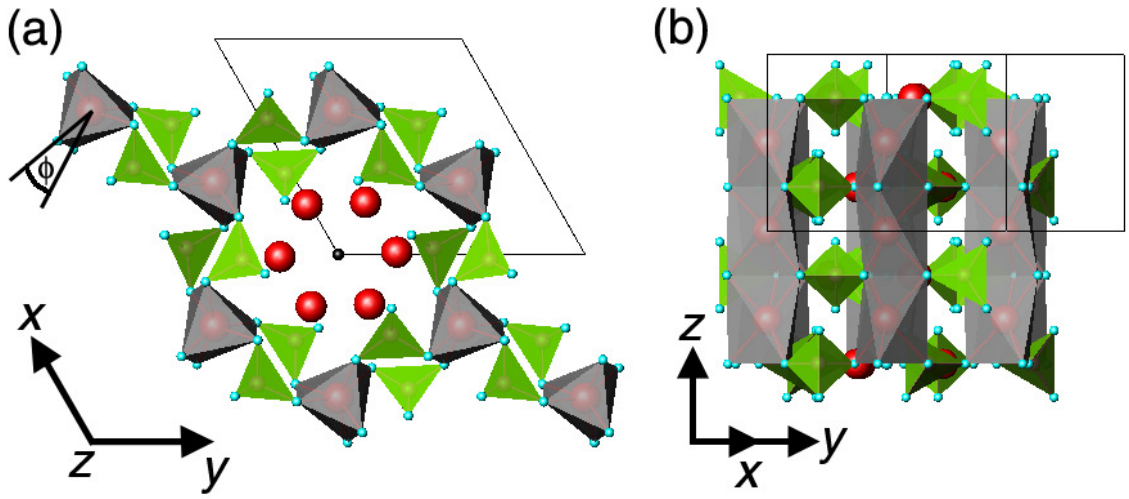

Figure 4 Structure of $P6_3/m$ $La_8Sr_2(GeO_4)_6O_2$ apatite electrolyte[12] projected along (a) [001] and (b) [100]. With respect to the prototype A^{I} = La, Sr; A^{II} = La; B = Ge and X = O.

2.3 Crystallographic Modification of Apatites*

2.3.1 Polymorphic Apatites

Hydroxyapatite ($Ca_{10}(PO_4)_6(OH)_2$) (HAp) is familiar as the idealized inorganic component of bone and teeth,[78] and as noted earlier the architecture of HAp is zeolitic.[25] Columns of CaO_6 metaprisms (a distorted trigonal prism) are hinged by isolated PO_4 tetahedra to create a framework of ideal stoichiometry $[Ca_4(PO_4)_6]^{10-}$ that circumscribes one dimensional channels containing $[Ca_6(OH)_2]^{10+}$ (Figure 5). Many chemical analogues adopt this structural motif and counter-ions of valences from 1+ to 7+ can be incorporated to maintain charge neutrality while the framework flexes topologically to match the tunnel diameter with the abundance and size of its contents.

More than 70 apatite chemical end-members are known whose compositions can be generalized as $\boldsymbol{A_{10}(BO_4)_6X_2}$ where *A* and *B* are larger and smaller cations and *X* are anions.[25,75] This genus is commonly considered the only representative of the apatite family, but in fact, the framework is exceedingly adaptive (Figure 6).

Mimetite is a mineral species with ideal composition $Pb_{10}(AsO_4)_6Cl_2$,[79] but unlike HAp where *B* is of fixed valence (P^{5+}), arsenic may be reduced from As^{5+} to As^{3+}, and the $(AsO_4)^{3-}$ tetrahedra replaced by $(AsO_3)^{3-}$. When reduction proceeds to completion the distinct species $Pb_{10}(AsO_3)_6Cl_2$ finnemanite crystallizes,[80,81] where $[Pb_4(AsO_3)_6]^{10-}$ and $[Pb_6Cl_2]^{10+}$ are the framework and tunnel components respectively. Although fully six oxygens are removed per formula unit the structure remains intact through the stabilizing effects of the stereochemically active lone-pair electrons of As^{3+} and Pb^{2+}.[82-85] Finnemanite can be considered the archetype of the $\boldsymbol{A_{10}(BO_3)_6X_2}$ apatite genus. Finally, oxidized apatites result from the introduction of intermetallic species at the *B*-position.

*This section published substantially as Pramana *et al.* (2008) J. Solid State Chem., **181**, 1717-1722.
†The polysomatic apatite ideas included in Section 2.4 are contained in Baikie *et al.* (2010) Acta Crystallogr B, **66**, 1-16, to which the candidate made a partial contribution.

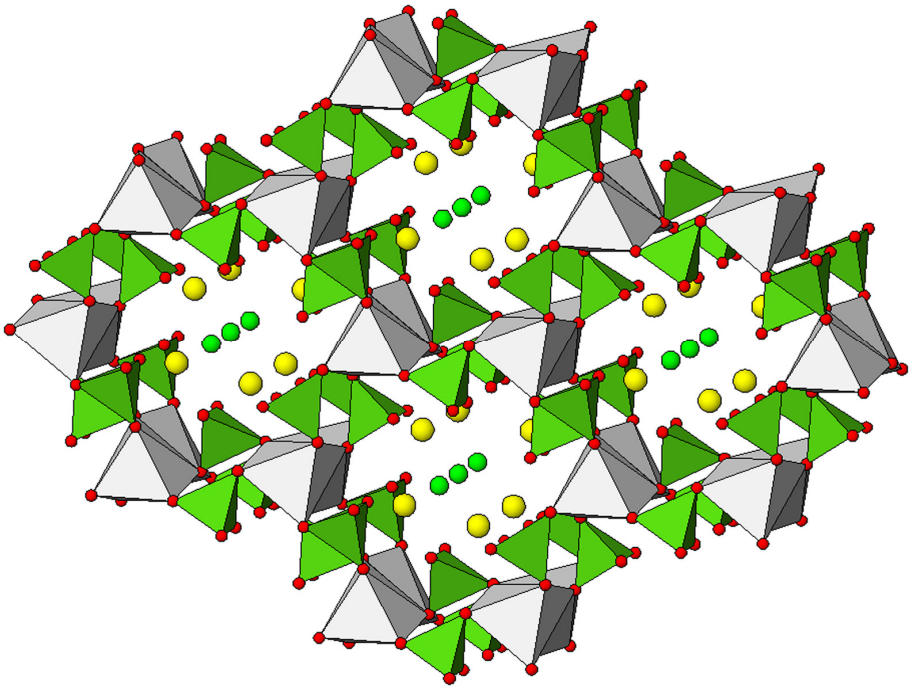

Figure 5 Tunnel structure of the $A_{10}(BO_4)_6X_2$ apatite genus exemplified by the electrolyte $[La_8Sr_2][(GeO_4)_6]O_2$. The grey AO_6 polyhedra are metraprisms containing lanthanum and strontium while the green BO_4 tetrahedra accommodate germanium. The tunnels contain the remaining lanthanum (yellow) and oxygen (green). The stoichiometry of the framework is $[A_4(BO_4)_6]$ while the large tunnels retain $[A_6X_2]$.

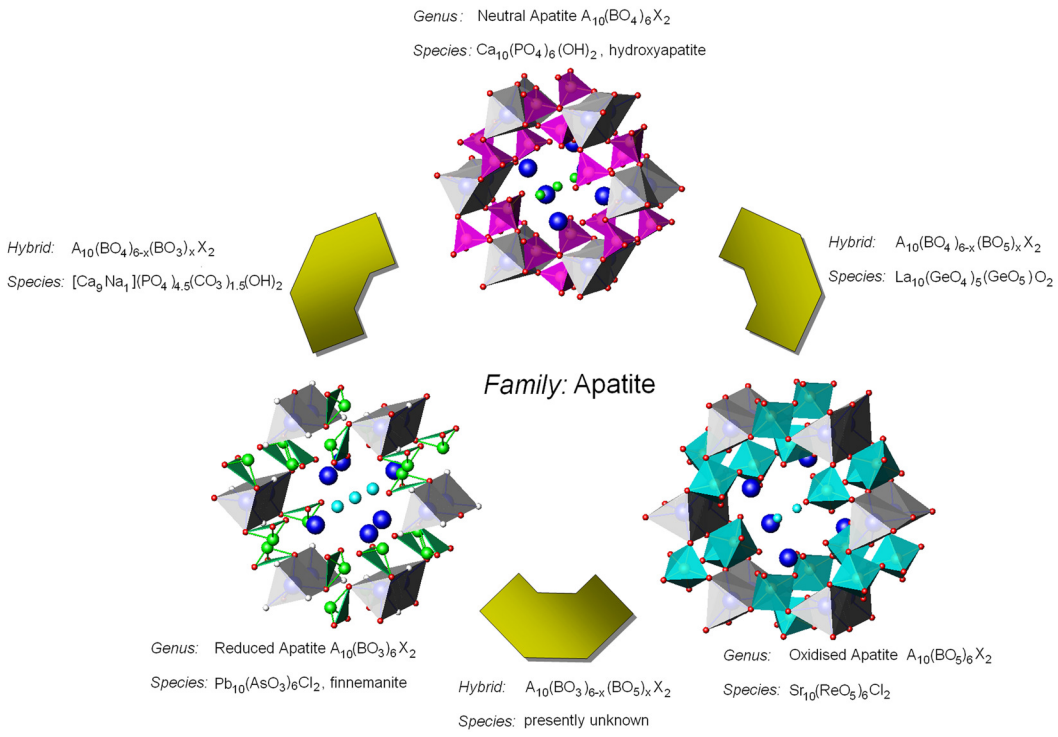

Figure 6 The apatite crystallographic family. In this taxonomy the apatite frameworks are divided into three genera: neutral apatites containing only (BO_4) tetrahedra; reduced apatites made up of (BO_3) units; and oxidized apatites with (BO_5) polyhedra. Hybrid apatites composed of $BO_3/BO_4/BO_5$ provide a means for crystallochemically tailoring the functionality of apatites.

One example is $Sr_{10}(ReO_5)_6Cl_2$ where Re^{7+} is accommodated in BO_5 square pyramidal coordination rather than BO_4 tetrahedra resulting in an $[Sr_4(ReO_5)_6]^{10-}$ framework and $[Sr_6Cl_2]^{10+}$ tunnel contents.[86] About 10 compounds, to date all rhenates and osmates, belong to the $\boldsymbol{A_{10}(BO_5)_6X_2}$ genus.[25,75]

All three apatite genera are hettotypes derived from $P6_3/mcm$ symmetry that describes the structure of many alloys,[87] including $Ca_{10}As_6$, which has an atomic arrangement equivalent to that of mimetite and finnemanite. This common descent of apatites as anion-stuffed alloys not only allows for systematic classification, but also predicates feasible stoichiometries and chemical tailoring of functionality. Moreover, there is in principle no impediment to the creation of apatite hybrids that contain mixtures of BO_3, BO_4, and BO_5 framework elements, as only the oxygen sub-structure is modified without disturbing the cation array. One such hybrid appears when carbonate (CO_3^{2-}) is incorporated in dental enamel and the apatites $[Ca_{10-x}Na_x][(PO_4)_{6-x}(CO_3)_x](OH)_2$ [88] have been synthesized where there is partial replacement of the $(PO_4)^{3-}$ group by $(CO_3)^{2-}$. This compound is an example of a *B*-type carbonate apatite. In this case, charge balance is maintained through the introduction of Na^+ as a framework counter ion by the substitution $Ca^{2+} + PO_4^{3-} \rightarrow Na^+ + CO_3^{2-}$. Another hybrid of this type may participate in the phase transition of mimetite to clinomimetite at ~100°C through the partial reduction of As^{5+} and the inclusion of finnemanite components.[79] Thus, hybrid apatites of the type $\boldsymbol{A_{10}(BO_4)_{6-x}(BO_3)_xX_2}$ exist.

Hybrids containing mixtures of BO_4/BO_5 units were unknown before the recognition that $[La_{10}][(GeO_4)_5(GeO_5)]O_2$ electrolyte apatite contains germanium in both tetrahedral and trigonal bipyramidal coordination to yield a $[La_4(GeO_4)_5(GeO_5)]^{14-}$ framework surrounding $[La_6O_2]^{14+}$ as will be detailed in Section 4.1. This surprising result – it had been thought extra-stoichiometric oxygen was retained in the tunnels rather than the framework[14,29,89-93] – was the first example of an $\boldsymbol{A_{10}(BO_4)_{6-x}(BO_5)_xX_2}$ compound. The structural revision of $La_{10}Ge_6O_{27}$ leads to a picture of this electrolyte with a framework reservoir feeding oxygen ions into the larger tunnels where they can rapidly migrate; this new model also accounted for the frequently overlooked phenomenon of substantial oxygen transport across, as well as along, the tunnels.[30] The implication is that apatite electrolyte performance is mediated not by the

concentration of oxygen ions within the conducting tunnels, but the storage capacity of the framework that can both charge the conduit with O^{2-}, and at the unit cell scale, circumvent tunnel "blockages" by inter-tunnel diffusion, as further developed in Sections 4.2 and 4.3.

Finally, while $\boldsymbol{A_{10}(BO_5)_{6-x}(BO_3)_xX_2}$ hybrids are yet to be reported, it is suggested that derivatives of $Sr_{10}(ReO_5)_6Cl_2$ such as $[Sr_{10-x}Na_x][(ReO_5)_{6-x}(CO_3)_x]Cl_2$, where $Sr^{2+} + (ReO_5)^{3-} \rightarrow Na^+ + (CO_3)^{2-}$ might be prepared and exhibit interesting electrolyte properties. These prospective hybrids and their crystallographic complexity will be considered in more depth in Section 4.5.

2.3.2 Relationship between Twist Angle and Conductivity

The metaprism twist angle (ϕ) (Section 2.2) is often used to quantify the degree of structural distortion of tabular apatite modules that are rotationally twinned along [001], and as explored in the following section, ϕ is a sensitive measure of substitutional mechanisms and stoichiometric deviations.[25] When A^{I} is occupied by a smaller ion, or A^{II} by a larger constituent, ϕ will be more acute, and the tunnel dilates to facilitate more ready transport of mobile oxygen along the channel. Intra-tunnel migration can then, in principle, be enhanced by fabricating relatively large frameworks as recently demonstrated by Kendrick and Slater[94] for $La_8Y_2Ge_6O_{27}$. However, consideration of ϕ alone cannot account for the inter-tunnel conduction that was reported by Nakayama and Higuchi.[30] In addition, an interstitial oxygen must be located between two BO_4 tetrahedra to allow migration to an adjacent channel as described for $La_{10}Ge_6O_{27}$ (see Section 4.1).

2.3.3 Space Group Hierarchy and Degrees of Freedom

As noted in Section 2.2, hexagonal $P6_3/m$ apatite can be described as an anion-stuffed derivative of the $P6_3/mcm$ Mn_5Si_3 $D8_8$ alloy type (Figure 7).[87,95-97] When applied specifically to lanthanum germanate electrolytes, La_5Ge_3 is taken as a hypothetical alloy, where the ordered insertion of oxygen displaces the La^{I} from (1/3 2/3 0) to (1/3

2/3 *z*), and La^{II} and Ge relocated from (*x* 0 1/4) to (*x y* 1/4); these displacements generate $P6_3/m$ symmetry from the $P6_3/mcm$ aristotype. Mismatch between the framework and tunnel ions will flex the structure, and larger mismatch induces transformation to lower symmetries. In this case, the La^{I} at 4*f* (1/3 2/3 *z*) and La^{II} 6*h* (*x y* 1/4) found in $P6_3/m$ reposition in $P2_1/m$ to a 4*f* (*x y z*) site and three 2*e* (*x y* 1/4) sites with loss of the 6_3 screw axis. Both the Ge and O at 6*h* (*x y* 1/4) and O at12*i* (*x y z*) are split to three unique 2*e* (*x y* 1/4) and 4*f* (*x y z*) sites, while the tunnel oxygen moves freely in (*x y*) occupying 2*e* (*x y* 1/4). Interstitial framework oxygen can be introduced, with a further reduction in symmetry to $P\bar{1}$. Consolidating these transformations by considering the metaprisms, conveniently summarizes the increasing structural freedom at lower symmetry (Table 2). A single metaprism is found in both $P2_1/m$ and $P6_3/m$, however in the former, three independent twist angles are possible as the $\bar{6}$ inversion at (1/3 2/3 *z*) is removed. Transformation to $P\bar{1}$ creates 2 metaprisms each with 3 twist angles, and permits the introduction of interstitial oxygen with the creation of GeO_5 trigonal bipyramids that provide low energy pathways for oxygen conduction.

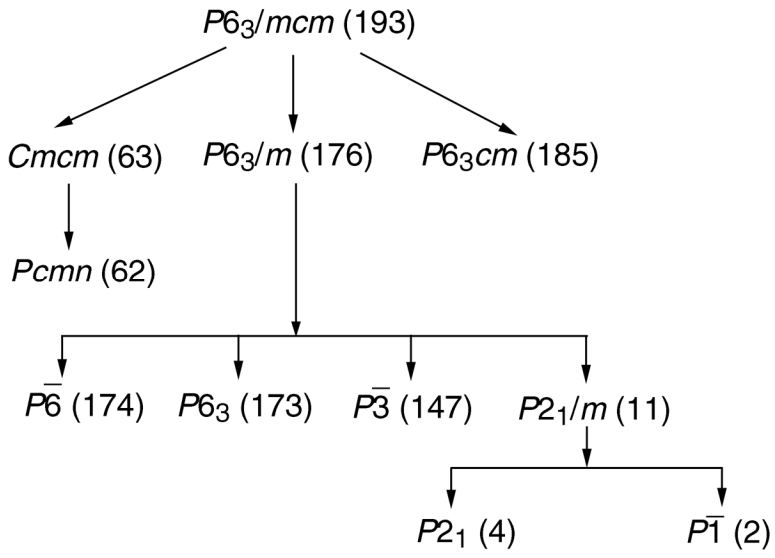

Figure 7 Symmetry relationships for apatite hettotypes [Adapted from Schriewer & Jeitschko[98] and White & Dong[75]].

Table 2 Crystallographic degrees of freedom in apatite polymorphs.

	Space Group	193 $P\,6_3/m\,2/c\,2/m$	176 $P6_3/m$	11 $P\,1\,1\,2_1/m$	4 $P\,1\,1\,2_1$	2 $P\bar{1}$
Metric	Unit cell	$a=b\neq c$ $\alpha=\beta=90°, \gamma=120°$	$a=b\neq c$ $\alpha=\beta=90°, \gamma=120°$	$a\neq b\neq c$ $\alpha=\beta=90°, \gamma\neq 120°$	$a\neq b\neq c$ $\alpha=\beta=90°, \gamma\neq 120°$	$a\neq b\neq c$ $\alpha\neq\beta\neq\gamma$
	Degrees of freedom	2	2	4	4	6
Positions	A^{I}	4*d* (1/3 2/3 0)	4*f* (1/3 2/3 *z*)	4*f* (*x y z*)	2*a* x 2 (*x y z*)	2*i* x 2 (*x y z*)
	A^{II}	6g (*x* 0 1/4)	6*h* (*x y* 1/4)	2*e* x 3 (*x y* 1/4)	2*a* x 3 (*x y z*)	2*i* x 3 (*x y z*)
	B	6g (*x* 0 1/4)	6*h* (*x y* 1/4)	2*e* x 3 (*x y* 1/4)	2*a* x 3 (*x y z*)	2*i* x 3 (*x y z*)
	Framework O	-	6*h* x 2 (*x y* 1/4)	2*e* x 6 (*x y* 1/4)	2*a* x 6 (*x y z*)	2*i* x 6 (*x y z*)
	Degrees of freedom	2	9	27	42	42
Metaprism	Unique metaprism	-	1	1	2	2
	Unique ϕ per metaprism	-	1	3	3	3
	Degrees of freedom	-	1	3	6	6

In general, greater $A^{I}O_6$ metaprism twisting in apatite precedes adjustment to lower symmetry. Metaprism twisting is (00ℓ) planar (except for $P\bar{1}$), and this two-dimensional motion proves analogous to the three-dimensional systematics in ABO_3 perovskites, where BO_6 octahedral tilting creates polymorphic modifications related to chemistry and ionic size. For example, when *A* is much smaller than *B*, BO_6 tilting is larger which favors lower symmetry (viz. $SrTiO_3$ is cubic while $SrZrO_3$ and $CaTiO_3$ are orthorhombic).[99] In addition, adjustments in temperature (high temperature favors high symmetry) and pressure (high pressure favors low symmetry) can promote phase changes as the relative sizes of the ions are modified.[99] In an analogous way, more complete filling of the apatite tunnel (smaller ϕ) promotes high symmetry (e.g. water incorporation in $La_{10-x}\square_x(GeO_4)_6O_{3-1.5x}$),[100] and high temperatures transform triclinic to hexagonal apatite (e.g. $Ca_{10}(VO_4)_6F_2$ and $Ca_{10}(AsO_4)_6F_2$)[101]. In this latter example, in-situ diffraction may reveal a transitory monoclinic phase, as appears to be confirmed from conductivity measurements in $La_{10}(GeO_4)_5(GeO_5)O_2$ (Section 4.1.3).

2.4 Polysomatic Apatites

The potential exploitation of apatite polysomes as electrolytes is beyond the scope of this thesis, however, for completeness a short discussion is included here, in so far as polysome nomenclature will be used, and this description impacts upon the interpretation of the silicate apatite electrolyte properties considered in Section 4.4.

In polysomes, ϕ is usually quite acute, and it is practical to adopt ϕ = 0° as an idealized polysome module having the composition $A^{I}_{2}A^{II}_{3}B_3O_{18}X$ and a thickness of ~3.5 Å with the disposition of trigonal prisms and tetrahedra shown in Figure 8. These modules, or tablets, can occupy a hexagonal unit cell in two orientations, designated the *α*- and *β*-layers, that are rotated 60° with respect to each other, with condensation leading to the elimination of oxygen from the coincident lattice positions. Layers joined without rotation create corner-connected B_nO_{3n+1} ($n = \infty$) tetrahedral strings that can be broken through introducing a rotated layer. Thus, if the modules are placed directly one upon the other in the sequence ... *α*(*α*)*α*... the hypothetical compound $A^{I}_{2}A^{II}_{3}B_3O_9X$ is created that contains continuous chains of corner-connected tetrahedra (Figure 8b). In this case, nine oxygens are duplicated in the coincident lattice – three from two triangular prism faces and one from each of the three tetrahedra at the conjoined module boundary. Alternatively, if every tablet is rotated 60° (rotationally twinned) with respect to its neighbors in the order ...*β*(*αβ*)*α*..., six oxygen per layer pair are duplicated in the trigonal prisms, and the overall composition of the polysome is $A^{I}_{4}A^{II}_{6}B_6O_{24}X_2$. In this configuration, the BO_4 tetrahedra remain isolated and the familiar $[A^{I}_{4}][A^{II}_{6}][(BO_4)_6]X_2$ apatite motif results (Figure 8b).

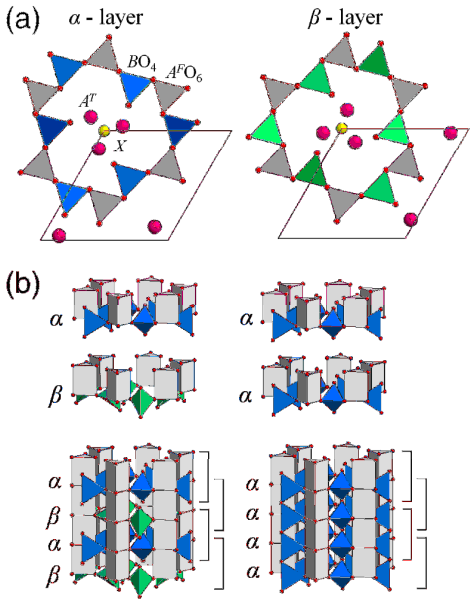

Figure 8 (a) Schematic representation of α and *β*, $A_5B_3O_{18}X_2$ apatite modules (assuming an hexagonal basal plane) that are related by $[001]_{hex}$ 60° rotation twinning. The principle idealization is that the $A^{I}O_6$ polyhedron is represented as a trigonal prism, but in real polysomes, twisting of the triangular faces through an angle ϕ creates metaprisms. (b) Stacking of *α* and *β* modules for the construction of …*β*(*αβ*)*α*… apatite-2*H*, $A_{10}(BO_4)_6X_2$ (left) and the hypothetical structure …*α*(*α*)*α*… apatite-1*H*, $A_5(B_3O_9)X$ (right) polysome endmembers. The coincident lattice where condensation and elimination of oxygen takes place is emphasized by brackets. For clarity the A^{II} and *X* ions are not included [Taken from Baikie *et al.*[102]].

An infinite number of arrangements intermediate to ...$\alpha(\alpha)\alpha$... and ...$\beta(\alpha\beta)\alpha$... are possible, and the ideal compositions of the apatite polysomes can be expressed as $A_{5N}B_{3N}O_{9N+6}X_{N\delta}$ ($2 \leq N \leq \infty$) where N is the number of modules ($A_5B_3O_{18}X_\delta$) in the crystallographic repeat. All the tetrahedral sequences for the polysomes with $N = 2$ to 5 are collated in Table 3 and Figure 9, and evidentially, longer period structures can in principle adopt compositionally equivalent but structurally distinct configurations.

The fundamental crystallographic principles of twist angle adjustment, framework hybridization and polysomatism can operate co-operatively, and when apatite phase space is viewed in total it is evident that substantial opportunities exist to formulate new derivatives through the creation of $A^{I}_4A^{II}_6(BO_3/BO_4/BO_5)_6X_2$ hybrids that may display polysomatic character (Figure 10).

Table 3 Stacking sequences and compositions of polysomatic apatites [Adapted from Baikie *et al.*[102]].

N	Crystallochemical Formulae	Chemical Formulae	Stacking Sequence
2	$A_{10}(BO_4)_6X_{2\delta}$	$A_{10}B_6O_{24}X_{2\delta}$ [(a)]	…$\beta(\alpha\beta)\alpha$…
3	$A_{15}(B_2O_7)_3(BO_4)_3X_{3\delta}$	$A_{15}B_9O_{33}X_{3\delta}$ [(b)]	…$\beta(\alpha\alpha\beta)\alpha$…
4	$A_{20}(B_3O_{10})_3(BO_3)_3X_{4\delta}$	$A_{20}B_{12}O_{42}X_{4\delta}$	…$\beta(\alpha\alpha\alpha\beta)\alpha$…
	$A_{20}(B_2O_7)_6X_{4\delta}$	$A_{20}B_{12}O_{42}X_{4\delta}$ [(c)]	…$\beta(\alpha\alpha\beta\beta)\alpha$…
5	$A_{25}(B_4O_{13})_3(BO_4)_3X_{5\delta}$	$A_{25}B_{15}O_{51}X_{5\delta}$	…$\beta(\alpha\alpha\alpha\alpha\beta)\alpha$…
	$A_{25}(B_3O_{10})_3(B_2O_7)_3X_{5\delta}$	$A_{25}B_{15}O_{51}X_{5\delta}$	…$\beta(\alpha\alpha\alpha\beta\beta)\alpha$…
∞	$A_5(B_3O_9)X_\delta$	$A_5B_3O_9X_\delta$	…$\alpha(\alpha)\alpha$…

[(a)] apatite [(b)] ganomalite [(c)] nasonite

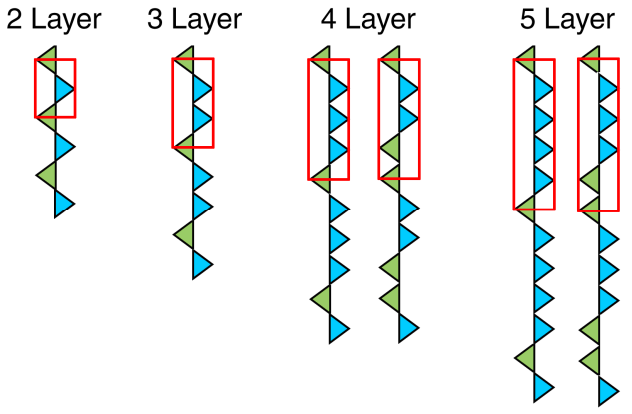

Figure 9 Possible tetrahedral stacking sequences for polysomes with $2 \leq N \leq 5$ [Adapted from Baikie *et al.*[102]].

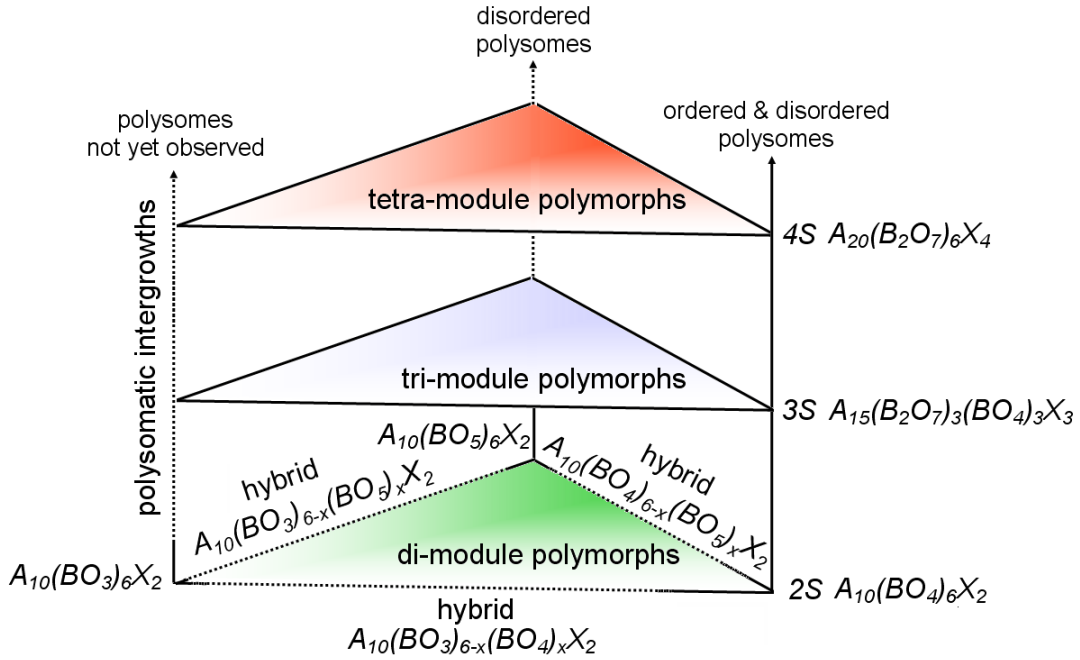

Figure 10 An expanded apatite phase space containing all permutations of polymorphs, pseudomorphs, polysomes and hybrid structures that may be feasible [Taken from Baikie *et al.*[102]].

2.4.1 Apatite Polysome Nomenclature

The key features of polysomatic apatites can be summarized using the nomenclature apatite-(*ABX*)-N*S* where *ABX* are the most abundant atoms on these sites, N is the number of layers in the crystallographic repeat, and *S* is the lattice symmetry.* So, for example, hexagonal hydroxyapatite[78] $Ca_{10}(PO_4)_6(OH)_2$ is hydroxyapatite-(CaPOH)-2*H* while triclinic svabite[76] $Ca_{10}(AsO_4)_6F_2$ would be svabite-(CaAsF)-2*A*. Nasonite[104] with hexagonal symmetry and four layers in its polysomatic repetition can be summarized as nasonite-(PbSiCl)-4*H*. This thesis only considers di-module apatite electrolytes such as $La_{10}(GeO_4)_5(GeO_5)O_2$ that is triclinic $P\bar{1}$ (apatite-(LaGeO)-2*A*) and $La_8Sr_2(GeO_4)_6O_2$ which is hexagonal $P6_3/m$ (apatite-(LaGeO)-2*H*).[28,91]

*This nomenclature is an adaptation of the scheme developed by The Commission on New Minerals, Nomenclature and Classification.[103]

2.4.2 Possible Role of Polysomes in Silicate-Based Electrolytes

From the crystallographic point-of-view it is highly unlikely that *A* cation vacancies, known to be essential for acceptable silicate apatite electrolyte performance, will appear at the A^{I} site rather than A^{II} in $N = 2$ apatites because A^{I} is 'strongly' bonded to the six neighbor oxygens. However, A^{I} substoichiometry can be rationalized in the polysomatic formalization where A^{I} vacancies can be stabilized by condensing BO_4 tetrahedra as B_2O_7 bridging units, to create stable cages as observed in Figure 11.[102] Furthermore, polysomes possess acute ϕ as already noted, which leads to tunnel expansion and higher intra-tunnel oxygen mobility.

While direct crystallographic evidence for BO_4 condensation in electrolytes is presently lacking, ^{29}Si NMR is supportive, with additional chemical shifts belonging to both Si_2O_7 and Si_2O_9 detected in $La_{9.33}\square_{0.67}(SiO_4)_6O_2$.[105] It was proposed that the introduction of interstitial oxygen in apatite correlates with the creation of a La vacancy *via*

$$2La^{3+} + 6(SiO_4)^{4-} \rightarrow 2\square_{La^{3+}} + 3(Si_2O_7)^{6-} + 3\square_{O^{2-}} \quad \textbf{(4)}$$

$$6(SiO_4)^{4-} + 3O_{int}^{2-} \rightarrow 3(Si_2O_9)^{10-} \quad \textbf{(5)}$$

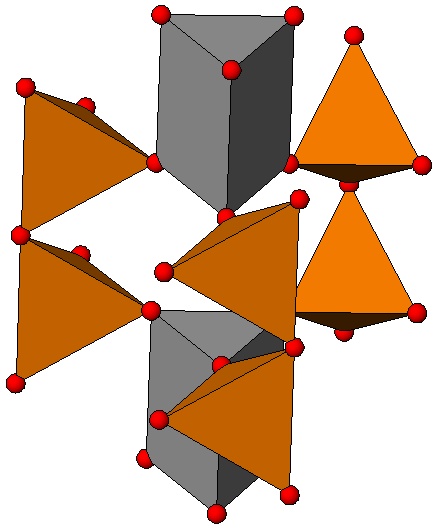

Figure 11 Postulated topology of Si_2O_7 constructed cages surrounding La^{3+} vacancies in the LaO_6 prismatic columns of lanthanum silicate oxyapatite electrolytes.

2.5 Doping Strategies in Apatites

Hexagonal hydroxyapatite $Ca_{10}(PO_4)_6(OH)_2$ which is commonly used in bone replacements is the parent structure, crystallochemically described as $A^{I}_4A^{II}_6(BO_4)_6X_2$.[78] However, it is unsuitable as a SOFC electrolyte because it is essentially stoichiometric and does not contain interstitial and vacancy defects, similar to undoped zirconia and ceria,[34,106] resulting in poor oxygen ion conductivity (σ = $2.0x10^{-6}$ Scm^{-1} at 900°C[107]). Furthermore, it is essential that the *X* anion is O^{2-}, rather than OH^- or a vacancy, for significant ion mobility.

Hence, in order to synthesize an apatite with interstitials[2,9] or vacancies,[30,108] the following altervalent substitutions were used:

$$10Ca^{2+} + 6(PO_4)^{3-} + 2(OH)^- \rightarrow 9.33RE^{3+} + 0.67\square + 6(Si/GeO_4)^{4-} + 2O^{2-} \quad \textbf{(6)}$$

$$10Ca^{2+} + 6(PO_4)^{3-} + 2(OH)^- \rightarrow 10RE^{3+} + 6(Si/GeO_4)^{4-} + 3O^{2-} \quad \textbf{(7)}$$

Among the rare earths (*RE*), lanthanum was chosen because its ionic radius is the largest among rare earth elements and maximally dilate the apatite tunnel to improve oxygen ion conduction.[109,110] The silicate $(SiO_4)^{4-}$ framework was studied in the early development of the electrolytes because of its rigid structure and stability at higher temperature.[2,9] In addition, Slater *et al.*[3,15] and Arikawa *et al.*[111] reported that the germanate $(GeO_4)^{4-}$ analogue of $(SiO_4)^{4-}$ had higher conductivity presumably because of larger ionic radius of Ge compared to Si. However, the Ge-system proved problematical at T > 1300°C due to volatilization of GeO_2.[13,14]

Alkaline earths (*AE*) are often introduced to synthesize a stoichiometric apatite, RE_8AE_2Si/Ge_6O_{26}.[92,112] This prototype can be modified by adjusting the concentration of trivalent rare earths to study the mobility of "excess" oxygen when combined with stoichiometric *A*-cation occupancy. In this case, the RE_8AE_2Si/Ge_6O_{26} stoichiometric structure with low ionic conductivity[3] shows improved performance when oxygen is injected as:

$$AE^{2+} \rightarrow RE^{3+} + \tfrac{1}{2}\, O_{int}^{2-} \quad \textbf{(8)}$$

Alternatively, when high concentrations of AE^{2+} replaces RE^{3+}, oxygen vacancies are introduced and the apatite with an empty tunnel is presumably created, similar to the lacunar apatite $Pb_6Ca_2Na_2(PO_4)_6\square_2$[83] as follows:

$$RE^{3+} + ½\ O^{2-} \rightarrow AE^{2+} + ½\ \square_{O^{2-}} \quad \textbf{(9)}$$

Although the ionic conductivity of the lacunar apatite is very low ($6.5x10^{-9}$ Scm^{-1} at 700°C[83]), partial emptying of the tunnel oxygen may increase the conductivity, in a similar manner to yttria-stabilized zirconia (YSZ) where the oxygen vacancies improve conduction ($2Zr^{4+} + O^{2-} \rightarrow 2Y^{3+} + \square_{O^{2-}}$) as described in Section 2.1. Various alkaline earths with smaller and larger ionic radius relative to La (ionic radius of La^{3+}(VII) = 1.10 Å, Ca^{2+}(VII) = 1.06 Å, Sr^{2+}(VII) = 1.21 Å, Ba^{2+}(VII) = 1.38 Å)[43] were doped to study the different substitution mechanisms and corresponding ionic conductivity in apatites. As the reported ionic conductivity of $La_{10}(GeO_4)_6O_3$ $La_{9.33}\square_{0.67}(GeO_4)_6O_2$ are high (0.08 Scm^{-1} and 0.01 Scm^{-1} at 800°C, respectively)[65,111], the dopant concentration was chosen to optimize the contribution between vacancies and interstitials.

Finally, a fully oxidized apatite $A^{I}_4A^{II}_6(BO_5)_6X_2$ may hypothetically have increased conductivity as it contains six oxygen interstitials per unit cell with the framework conversion from BO_4 to BO_5, as for example in $Ba_{10}(ReO_5)_6O_2$.[113]

2.6 Conduction Mechanisms in Apatite

It is axiomatic that in oxides, ion conductivity is promoted by higher vacancy and interstitial concentrations and that understanding these mechanisms at an atomic level is a pre-requisite for optimizing performance. In apatites specifically, both cation vacancies and excess oxygen lead to larger ion fluxes, with the latter proving most decisive.[3] Defects can be incorporated by adding interstitial oxygen concomitantly with *A*-site vacancies. Some simple mechanisms include:

Oxygen excess

$$2A^{2+} + \square_{O^{2-}} \rightarrow 2A^{3+} + O^{2-} \quad \textbf{(10)}$$

$$2B^{4+} + \square_{O^{2-}} \rightarrow 2B^{5+} + O^{2-} \quad \textbf{(11)}$$

Oxygen deficient

$$2A^{3+} + 3O^{2-} \rightarrow 2\square_{A^{3+}} + 3\square_{O^{2-}} \quad \textbf{(12)}$$

$$2B^{4+} + O^{2-} \rightarrow 2B^{3+} + \square_{O^{2-}} \quad \textbf{(13)}$$

The equilibrium position of interstitial oxygen has to be located before the dynamics of oxygen movement can be studied, and has been determined in various apatite systems by powder neutron diffraction (Table 4).

Computational modeling based upon inter-atomistic potentials predicts that in apatite, intrinsic atomic defects – Frenkel and Schottky – may exist. For example, interstitial oxygen diffusion in non-stoichiometric $La_{9.33}Si_6O_{26}$ apatite is believed to follow a sinusoidal-like pathway along the *c*-axis, by placing the interstitial oxygen in various locations and allowing relaxation. In the stoichiometric $La_8Sr_2Si_6O_{26}$ apatite with *A* sites fully occupied and BO_4 tetrahedra, vacancy migration dominated conduction with a direct linear path between tunnel oxygens and a saddle point in the middle of the tunnel oxygen locations (Figure 12).[29]

Although high ionic conduction has been reported in silicate and germanate apatites, many challenges must be overcome, particularly induced mechanical stress, electrode sintering, electrode and interconnect material failure, fabrication and start-up time.[39]

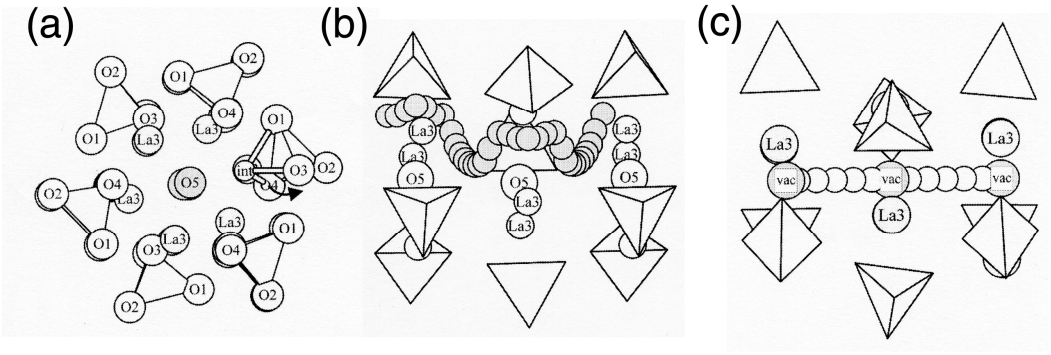

Figure 12 (a) Apatite crystal structure viewed along *c*-axis with the SiO_4 tetrahedra emphasized, (b) interstitial oxygen sinusoidal-like diffusion pathway in $La_{9.33}Si_6O_{26}$ and (c) oxygen vacancy migration along the tunnel in $La_8Sr_2Si_6O_{26}$ [Taken from Tolchard *et al.*[29]].

Table 4 Selected interstitial oxygen position for hexagonal apatites at room temperature.

	x	*y*	*z*
$La_{9.33}(SiO_4)_6O_2$ [29]	0.013	0.233	0.625
$La_{9.33}(SiO_4)_6O_2$ [91]	0.00	0.25	0.58
$La_{9.55}(SiO_4)_6O_{2.32}$ [89]	0.999	0.224	0.580
$La_{9.60}(GeO_4)_6O_{2.40}$ [89]	0.016	0.228	0.606
$La_{9.33}(Si_{0.5}Ge_{0.5}O_4)_6O_2$ [91]	0.005	0.242	0.610
$La_8Sr_2(SiO_4)_6O_2$ [29]	0.013	0.232	0.616
$La_8Sr_2(SiO_4)_6O_2$ [91]	0.005	0.242	0.610
$La_8Sr_2(GeO_4)_6O_2$ [91]	0.005	0.242	0.610
$La_{8.65}Sr_{1.35}(SiO_4)_6O_{2.32}$ [90]	0.014	0.071	0.555
$La_{8.65}Sr_{1.35}(GeO_4)_6O_{2.32}$ [90]	0.009	0.213	0.598
$La_9Sr(Si_{5.5}Al_{0.5}O_{24})O_{2.25}$ [90]	0.015	0.064	0.537
$La_{9.5}\square_{0.5}(Si_{5.5}Al_{0.5}O_{24})O_2$ [90]	0.991	0.221	0.570
$La_{9.5}\square_{0.5}(Ge_{5.5}Al_{0.5}O_{24})O_2$ [66]	0.01	0.21	0.62
$La_{10}(Si_5CoO_{24})O_{2.5}$ [114]	0.051	0.244	0.590

2.7 Conclusion: Optimization of Structure, Functionality and Performance

Polymorphic transformations (driven by change in temperature), pseudomorphic transformations (initiated by compositional adjustments) and polysomatic adaptations (which may stabilize *A* cation substoichiometry) together allow the possibility of designing new hybrid apatite electrolytes. Oxygen mobility can be tuned by controlling the metaprism twist angle and introducing altervalent cation substitutions that favor interstitial and vacancy formation. The crystallochemical manipulations employed in these studies to enhance electrolyte performance are: (i) adjusting the size of the apatite framework, relative to the tunnel, to give acute metaprism twist angles that open intra-tunnel conduction pathways; (ii) exploiting counter-ion substitutions, to accommodate extrastoichiometric oxygen in the framework reservoir, that in turn, reduces activation energy and introduces more mobile oxygen; and (iii) stabilizing *A* cation vacancies in tandem with increasing the concentration of framework oxygen to maximize inter-tunnel conduction. These mechanisms will operate co-operatively. By recognizing these fundamental concepts, strategies for creating structures that deliver optimal performance can be devised.

Chapter 3

Research Methodologies

3.1 Synthesis

In every case, conventional solid state synthesis was used as in general volatilization of components was not significant at T ≤ 1300°C,[13,14] and repeated grinding and firing cycles usually ensure good yields. Not reported here are syntheses by sol gel[18-20] and hydrothermal methods[21-24] which often gave finely divided and small crystallite size and even amorphous products,[115] however these matters were not so suitable for detailed crystallographic analyses that were a focus of this research.

The alkaline earth doped lanthanum germanate apatite powders were synthesized by solid-state reaction (Sections 4.1, 4.2 and 4.3).

$$(5\text{-}x/2)\ La_2O_3 + x\ AECO_3 + 6\ GeO_2 \rightarrow La_{10-x}AE_xGe_6O_{27-x/2} + x\ CO_2\uparrow \quad \textbf{(14)}$$

La_2O_3 (BDH, 99.5%), $CaCO_3$ (Fluka, 99.0%), $SrCO_3$ (Riedel-de Haën, 96%), $BaCO_3$ (Fluka, 98.5%), GeO_2 (Alfa Aesar, 99.999%) were dehydrated for 4 hours at 1000°C, 500°C, 600°C, respectively, after which stoichiometric amounts were manually ground in an agate mortar and pestle and calcined at 1100°C for 16 hours. These powders were reground and sintered at 1300°C for another 16 hours in a platinum crucible.

Synthesis of $La_{9.33}Si_6O_{26}$ (Section 4.4) was by solid state reaction of La_2O_3 (BDH, 99.5%) and SiO_2 (Baker, 99%). In addition, two sodium-substituted $La_{9.33-x/3}Na_xSi_6O_{26}$ apatites (x = 0.5 and 1) together with protonated compounds $La_{9-y}Na_{1+y}Si_6O_{26-\delta}H_\gamma$ (y = 0, 0.5 and 1) were synthesized through the addition of Na_2CO_3 (Alfa Aesar, 99.9%). These starting powders were ground in an agate mortar for 15 mins, pelletized and sintered at 1773 K for 16 h in a platinum crucible.

Electrolyte apatites of notional composition $Ba_{10-x}Sr_x(ReO_5)_6O_2$ (0, 5 and 10) were synthesized by the solid-state sintering (Section 4.5). $BaCO_3$ (Fluka, 98.5%), $SrCO_3$ (Riedel-de Haën, 96%) and Re_2O_7 (Sigma Aldrich, 99%) were manually ground together in stoichiometric proportions in an agate mortar and pestle, followed by sintering in air (600°C/24 h and 120 h) in an alumina crucible.

3.2 Characterization Methodology

A comprehensive characterization methodology of SOFC apatite electrolytes must include (1) quantitative phase analysis, especially the identification of secondary phases that may detract from performance; (2) the recognition of polymorphism as a function of temperature or compositional variation that will modify ion conducting pathways; (3) location of interstitial oxygen and metal vacancies that control the mechanism of ion conduction; and (4) the correlation of crystal chemical properties with ion flux and activation energy for migration.

Extracting these parameters requires a suite of tools that can probe the electrolyte structurally and chemically from atomic to micron scales. This can be accomplished effectively through a combination of diffraction and spectroscopic methods as described below.

3.2.1 Diffraction Methods

3.2.1.1 Laboratory Powder X-ray Diffraction

Laboratory powder X-ray diffraction (XRD) using CuK_α radiation (λ_{av} = 1.54 Å) collimated with a 2.5° soller, 1° divergence and 0.3 mm receiving slits, a secondary graphite monochromator and a scintillation counter (Bruker D8 Advance and Shimadzu XRD-6000) can be employed to extract lattice parameters and the crystallographic motif of heavy elements. While a readily available and simple technique, it is unsuitable for acquiring low atomic number (*Z*) information when both heavy and light elements are present, as the latter are masked by the former. Because the X-rays interact with the orbital electrons, form factors from high *Z* scattering elements will overwhelm the low *Z* elements. Moreover, apatite crystals are often acicular (with extension along *c*), and preferred orientation may modify diffracted intensities in ways that cannot be readily corrected. In these cases, grinding may be beneficial, but can also lead to peak broadening that makes the recognition of lower symmetry metrics difficult. Laboratory XRD can deliver accurate unit cell parameters

for apatite electrolytes, but the geometry of oxygen sub-lattice, which controls ionic conductivity, cannot be extracted with high reliability.

3.2.1.2 Powder Neutron Diffraction

While X-rays interact with the electron density surrounding the atoms, neutrons scatter from the nuclei with the strength of the interaction being isotope dependent. For example ^{1}H, ^{2}H and ^{3}H possess vastly different coherent and incoherent neutron scattering lengths. Because the scattering process of X-rays and neutrons is physically distinct, different combinations of elements in a crystal structure are best studied by one or other type of diffraction.

In apatite electrolytes, the neutron scattering lengths of oxygen and deuterium are large making detection and location relatively easy, as distinct from X-rays. Another fundamental difference is that neutrons are sensitive to nuclear magnetic moment and can be used to investigate magnetic structures, although this attribute is not required for the study of SOFC electrolytes.[116]

3.2.1.2.1 Powder Neutron Diffraction at the High Flux Australian Reactor

Powder neutron diffraction data of $La_{10-x}Sr_xGe_6O_{27-x/2}$ ($0 \leq x \leq 2$) were collected on the High Resolution Powder Diffractometer (HRPD) at the High Flux Australian Reactor (HIFAR) operated by the Australian Nuclear Science and Technology Organization (ANSTO) (Section 4.1). Approximately 15 g of the apatite was loaded into a 12 mm diameter vanadium can that was rotated during data collection. The diffraction data were accumulated at ambient temperature using a neutron wavelength of 1.8834(1) Å from 0.027° to 150.027° 2θ in 0.05° steps.

3.2.1.2.2 Powder Neutron Diffraction at the Indonesia National Nuclear Energy Agency

Neutron powder diffraction data were collected from $La_{10-x}Sr_xGe_6O_{27-x/2}$ (nominal $3 \leq x \leq 6$) using a 32 detector diffractometer installed at the Neutron Scattering Laboratory, Indonesia National Nuclear Energy Agency (BATAN) (Section 4.2). A hot-pressed Ge(331) monochromator with a 89° take-off angle yielding a wavelength of 1.822(1) Å was used. Approximately 6g of sample was loaded into a 12 mm diameter vanadium can. Patterns were collected at ambient temperature over the range of 10 – 150° in 2θ with a step size of 0.05°.

3.2.1.2.3 Temperature Dependent Powder Neutron Diffraction at ISIS

Time-of-flight (TOF) powder neutron diffraction patterns were obtained on the High Resolution Powder Diffractometer (HRPD) at ISIS Pulsed Neutron and Muon Source, Rutherford Appleton Laboratory, UK in the temperature range from 200 to 1000 °C (Section 4.1.3). A 12 mm diameter vanadium can was used to contain 6 g of apatite powder. Data sets (1.0 Å $\leq$ *d*-spacing $\leq$ 2.5 Å) from the back-scattering bank ($2\theta \approx 145°$) were used for the refinement.

3.2.1.3 Synchrotron Powder X-ray Diffraction

Due to the inherent limitations associated with powder neutron diffraction and conventional laboratory based X-ray sources (i.e. peak width, overlapping reflections, low reflection intensity), accurate lattice parameters and absolute occupancy of the elements that have relatively similar *Z* cannot always be satisfactorily determined. These limitations can be overcome in part, by using multiple X-ray wavelengths, high intensity radiation and monochromatic illumination produced by a synchrotron.

Resonant X-ray scattering takes advantage of the variation of the cross section of an atom at energies near its X-ray absorption edge where the strength of the interaction will be drastically altered by anomalous dispersion. When the energy of the incident

X-ray beam is close to an absorption edge, the atomic scattering factor *f* can be expressed in the following form:

$$f(Q, E) = f^{\circ}(Q) + f'(E) + i f''(E) \quad \textbf{(15)}$$

where Q and E are the wave vector and the incident X-ray energy. The first term f° corresponds to the normal scattering factor which is dependent on the atomic number given by the Fourier transform of the electron density in an atom, while *f*' and *f*'' are the real and imaginary components of the resonant dispersion terms. Multiple wavelength anomalous diffraction (MAD) can unambiguously determine the crystallographic site occupancy of elements with similar *Z*.

3.2.1.3.1 Synchrotron Powder X-ray Diffraction at Singapore Synchrotron Light Source

Resonant X-ray scattering was conducted using the X-ray Development and Demonstration Beamline of the Singapore Synchrotron Light Source (SSLS) that operates a Helios 2 storage ring at 700 MeV with a typical stored electron beam current of 300 mA (Section 4.4). The X-ray energy was selected with a Si (111) channel-cut monochromator, blocked to be 1 mm high vertically and focused to be 3.5 mm wide horizontally by a collimating mirror and slit system. This configuration yields an X-ray beam of 0.01° divergence at 8.048 keV. The detector slit was adjusted to be 1 mm high. The diffractometer was a Huber 4-circle system 90000-0216/0, with high-precision 0.0001° step size for the omega and two-theta circles using Bragg-Brentano geometry. The distance from entrance slit to sample centre was 688 mm and that from sample centre to detector 680 mm. The same powders used for the laboratory X-ray diffraction experiments were pressed gently into standard Bruker D5000 sample holders to reduce preferred orientation. In order to maximize the incident and diffracted X-ray intensities, most of the beam path was encapsulated in a plastic tube filled with helium. The typical counting time was 1 s per data point and a step size of 0.02° 2θ defines the FWHM of each reflection by at least 5 or 6 measurements.[117] All samples were scanned over the range 15°-120° 2θ. Prior to Rietveld analysis, the raw data were normalized to the counts recorded by the incident beam monitor.

3.2.1.3.2 Synchrotron Powder X-ray Diffraction at ANKA

High resolution synchrotron powder X-ray diffraction patterns were collected from $La_{10-x}Sr_xGe_6O_{27-x/2}$ (nominal x = 0, 1, 2) at room temperature using the PDIFF beamline at ANKA (Angstromquelle Karlsruhe) with a wavelength of 1.307 Å calibrated against Si (NIST-SRM 640c) and LaB_6 (NIST-SRM 660a) standards (Section 4.2). The samples were loaded into a flat plate holder that was rotated during data accumulation from 8 - 108.2° 2θ in 0.006° steps with a dwell time of 1 s per step.

3.2.1.4 Transmission Electron Microscopy

The wavelength of electrons accelerated to a voltage of 200 kV is 0.0251 Å and much shorter than X-rays commonly used for powder diffraction. In addition, the electron beam is highly coherent and can be focused to small beam diameters, which allows the direct observation of defects and atomic structures. The principles of electron diffraction, in common with other diffraction techniques, accord with Bragg's law. To determine the lattice metric and crystal symmetry, selected area electron diffraction (SAED) and convergent beam electron diffraction (CBED) techniques are often combined. High resolution transmission electron microscope (HRTEM) images are electron interference patterns arising from thin crystals, that at an appropriate defect-of-focus, reflect the projected potential of the structure and can readily distinguish perfect from defective regions. TEM has not been extensively used to study apatite electrolytes because many compositions are electron beam sensitive with micro-domain and nano-scale modulation introduced as artifacts.[118] This issue underlines the importance of growing large and perfect single crystal to unequivocally determine apatite space groups and provide a baseline for characterizing intrinsic extended defects.

Samples for electron diffraction were prepared by grinding under ethanol and drops of the resulting suspension deposited on holey-carbon coated copper-grids. Images were collected using a JEOL-2010 microscope operated at 200 kV and fitted with a low-background Gatan double tilt holder. Crystal were tilted to different zone axes. Simulated images were calculated by the multislice method implemented in *JEMS*[119]

and the structure model obtained by XRD refinement used as input. The principle parameters used were objective aperture diameter of 36 nm^{-1}, spread of focus of 5.5 nm and beam semi-convergence of 1 mrad. Digital filtering and tests for local symmetry were carried out using Fourier filtering methods as implemented in *CRISP*.[120]

3.2.1.5 Rietveld Refinement

The Rietveld refinement method calculates the entire powder pattern using a variety of refinable parameters.[121-125] The calculated intensity $y_i(calc)$ for a mixture of phases is

$$y_i(calc) = \sum_p \left(S_p . \sum_{pH} \left(M_{pH} . A_{pH}(2\theta_i) . P_{pH} . \left| F_{pH}(calc) \right|^2 . LP(2\theta_i) . \Phi_{pH}(2\theta_i) \right) \right) + B_i(obs) \quad (16)$$

at point i of the powder pattern and includes the contributions from all phases p contributing to the powder pattern and all Bragg reflections H of phase p, with the scale factor S_p, the multiplicity M_{pH}, the absorption correction $A_{pH}(2\theta_i)$, the preferred orientation correction P_{pH}, the square absolute value of the structure factor $|F_{pH}(calc)|^2$, the Lorentz-Polarization correction $LP(2\theta_i)$, the normalized profile function $\Phi_{pH}(2\theta_i)$ and the background contribution $B_i(obs)$. The weighted sum of the squared differences between the observed and calculated powder pattern is minimized by refining a set of parameters using a least square method

$$\sum_i w_i \left(y_i(obs) - y_i(calc) \right)^2 ; \quad w_i = \frac{1}{\sigma^2 \left(y_i(obs) \right)} \quad (17)$$

where $\sigma(y_i(obs))$ is the standard deviation in $y_i(obs)$. Many different statistical agreement factors or criteria of fit are used to determine the Rietveld refinement quality such as:

$$R_p = \frac{\sum_i \left| y_i(obs) - y_i(calc) \right|}{\sum_i y_i(obs)} \quad (18)$$

$$R_{wp} = \sqrt{\frac{\sum_i w_i \left(y_i(obs) - y_i(calc)\right)^2}{\sum_i w_i y_i(obs)^2}} \quad (19)$$

$$R_{\exp} = \sqrt{\frac{\sum M - P}{\sum_i w_i y_i(obs)^2}} \quad (20)$$

$$GOF = \chi^2 = \frac{R_{wp}}{R_{\exp}} \quad (21)$$

$$R_B = \frac{\sum_k I_k(obs) - I_k(calc)}{\sum_k I_k(obs)} \quad (22)$$

where M is the number of data points, P is the number of parameters, $I_k(obs)$ and $I_k(calc)$ are the observed and calculated intensities of the k^{th} reflection.[122,125]

The starting refinement model of germanate and silicate apatite used the atomic positions of $La_{10-x}(GeO_4)_6O_{3-1.5x}$ ($9.66 \leq 10 - x \leq 9.75$) in $P\bar{1}$,[14] while $La_8Sr_2(GeO_4)_6O_2$[28] was refined in the $P2_1/m$ space-group and $P6_3/m$ $La_{9.33}Si_6O_{26}$[126], respectively. The fundamental parameters or pseudo-Voigt peak-shape profile[124] as implemented in *TOPAS*[123] and corresponding X-ray form factor or neutron scattering lengths were used. For each data set, a five-coefficient Chebychev polynomial and *1/x* background, a zero error, unit-cell parameters, scale factors and crystal size were refined sequentially. Anisotropic peak broadening was introduced to model the (00ℓ) reflections. The cation positions were refined first, followed by the oxygen positions. Isotropic atomic displacement factors for all atoms were refined in groups as follows: framework A^{I} cations; tunnel A^{II} cations; Ge; and all oxygen (framework, tunnel, interstitial).

Time-of-flight (TOF) neutron data were refined using *GSAS*[127] with a pseudo-Voigt peak-shape combined with a back-to-back exponential peak profile (TOF profile function 3 in *GSAS*). Difference-Fourier maps were generated using *GFOURIER*[128] embedded in *FULLPROF*.[129]

3.2.2 Spectroscopic Methods

3.2.2.1 X-ray Absorption Spectroscopy

As oxygen interstitials and vacancies are essential for substantial ionic conduction, an understanding of coordinative transformations near the mobile ion and its pathway through the bulk is required. While the average structure can be determined by diffraction, the analysis of the local structure including coordination number and inter-atomic bond lengths is necessary to link diffusion with crystal relaxation. X-ray absorption spectroscopy (XAS) gathers this information by examining the oscillations that appear beyond a chosen X-ray absorption edge that arise from interference of an ejected photoelectron wave with the fraction of the wave backscattered from neighbors of the absorbing atom. In X-ray absorption near edge structure (XANES) spectroscopy, the low kinetic energy range (5-150 eV) leads to multiple scattering events, while extended X-ray absorption fine structure (EXAFS) employs energies > 150eV above the absorption edge that result from single scattering events. Fourier transformation of this oscillatory fine structure yields a radial distribution in real space with peaks corresponding to regions of higher electron density surrounding the absorbing atoms. In germanate apatite electrolytes, the interstitial oxygen was located near the apatite framework, relaxing the GeO_4 tetrahedra, and creating GeO_5 trigonal bipyramids.[130] In general, XAS data is often acquired for the *B* atoms in apatites, especially the Ge *K* absorption edges to determine the nature and abundance of interstitial oxygen.

X-ray absorption fine structure (XAFS) spectra from germanate samples were measured at the XAS bending magnet beamline of ANKA using a double crystal monochromator (DCM) with the Si (111) crystal pair. The higher harmonics were reduced by detuning the DCM to 65% of the maximum intensity. The data were accumulated at room temperature from 10953 eV to 12083 eV around Ge *K*-edge using a five element Ge detector. Several scans were collected for each spectrum and averaged. Data analysis followed a standard procedure using WinXAS.[131] The measured absorption spectra were normalized by employing a linear and second polynomial fit to the pre-edge and post-edge regions, respectively. Subsequent

processing included transforming from energy space to momentum (k) space, a seven-segment cubic-spline function fit to extract the XAFS oscillations, and Fourier Transformation (FT) from k space to real (R) space. In this manner, EXAFS over the ranges 2.2-17.5 $Å^{-1}$ in k space were extracted, then k^3 weighted and a Bessel window function applied. The data fitting of the Ge-O first shell only was performed in R-space using the theoretical phase shift and backscattering amplitude extracted from the $La_{9.33}(GeO_4)_6O_2$ model.[12] The inelastic factor, S_o^2 was determined by fitting to standard references and fixed at 0.9.

3.2.2.2 Fourier Transform Infrared Spectroscopy

Fourier transform infrared (FTIR) spectroscopy measures the molecular absorption and transmission characteristics of a material when exposed to infrared radiation. In this manner, resonant frequencies associated with rotation or vibration are easily detected. In this study, distinguishing oxyapatite from hydroxyapatite is essential for confirmation of the mobile carrier type.[132,133] The vibration modes in the apatite framework can also be differentiated; for example, the stretching vibration of GeO_4^{4-} tetrahedra, GeO_5^{6-} trigonal bipyramids and unreacted GeO_2 have distinct frequencies.[134]

Fourier transform infrared (FTIR) absorption was measured from 400 and 4000 cm^{-1} using a Perkin Elmer (Spectrum 2000) spectrophotometer with spectral resolution of 4 cm^{-1}. Translucent pellets were prepared by mixing and pelletizing apatite powder with pre-dried potassium bromide (KBr). Gaussian peak deconvolution was performed using PeakFit 4.12 from 580 – 1000 cm^{-1} by constraining the full width half maximum to be identical.

3.2.2.3 Nuclear Magnetic Resonance Spectroscopy

Nuclear magnetic resonance (NMR) spectroscopy exploits the property that nuclei with odd numbers of protons or neutrons (or both) possess a magnetic moment under the influence of a magnetic field, in addition to their charge, that produce unique

NMR spectra and features (chemical shift and intensity). In polysomatic apatites, the silicate/germanate group can exist as Si/GeO_4, Si/Ge_2O_7, Si/Ge_2O_9, Si/Ge_3O_{10}, Si/Ge_nO_{3n+1} units, each with a unique NMR spectra and chemical shift.[105,135] Furthermore, NMR experiments can deduce the distribution of ligands in non-symmetric crystallographic sites.[133]

The ^{139}La NMR spectra were acquired with a Bruker Avance 400 NMR spectrometer operating at 52.77 MHz from specimens with nominal $x = 0$ and 2. Static spectra were acquired using a two pulse echo sequence (repetition frequency 50Hz) in frequency stepped mode using pulse widths of 20μs with an irradiation bandwidth of 50 kHz. The pulse separation was 150 μs and data acquisition was started 50 μs after the second pulse. The whole echo was collected and Fourier transformed yielding an approximately Gaussian line. The amplitude of the line at the excitation frequency was then plotted as a function of frequency to give the complete spectrum. The step intervals ranged between 25 and 100 kHz and the probe was re-tuned after each step. The reference shift zero was established using an aqueous solution of $La(NO_3)_3$.

The ^{1}H NMR spectra were obtained with a Varian VNMRS spectrometer operating at 399.88 MHz from specimens with nominal $x = 3$, 4 and 5. A background suppression pulse sequence was used, and the signal from the empty rotor was subtracted from the spectra. A spectral width of 100 kHz and acquisition time of 10 ms were used, with a recycle delay of 30 s. Spectral referencing is with respect to tetramethylsilane.

3.2.2.4 Thermogravimetric Analysis

The proton/water content was measured by thermogravimetric analysis (TGA) using a Mettler Toledo TGA/SDTA851. Powders (60 mg) were placed in an alumina crucible and heated in air to 1000 °C at rate of 10 °C/min.

3.2.2.5 Impedance Spectroscopy

In electrochemical devices, including fuel cells, the ionic conductivity can be measured using alternating current (AC) impedance. By measuring impedance as a function of applied frequency and plotting as a Nyquist diagram, the type of conductivity, (i.e. bulk, grain boundary and electrode) can be differentiated. The equivalent circuit diagram shown in Figure 13 is typically used where R_b and R_{gb} is the bulk and grain boundary resistance, respectively, while a constant phase element (CPE) is usually employed to model the non-ideal capacitor which has the phase $0° < \varphi < 90°$. The measured impedances provide information about electrolyte conductivity, activation energy, reaction kinetics and mass-transfer.[136-138]

In this study, impedance was measured from pressed polycrystalline pellets, where resolution and quantification of R_b and R_{gb} is sometimes difficult.[19,139] Single crystal measurements will eliminate the effects of grain boundary resistance. In apatites, the structure is inherently anisotropic and maximum conductivity is assumed to take place along the *c*- axis, but this can only be validated with large crystals. Furthermore, sintered pellets are not fully dense leading to a deterioration of ionic conductivity. Spark plasma sintering can be used to produce pellets of near theoretical density.[140] In general, the activation energy for the powder bulk response will be similar to a single crystal only for isotropic conductors.

Pellets (1.3 cm diameter) for conductivity measurements were prepared as follows: the powders were ball milled (350 rpm, Fritsch Pulverisette 7 Planetary Mill) for 2 hours before pressing at 8000 kg cm^{-2}. The pressed pellets were then heated at 1400 °C for 2 hours to achieve 80-90% of theoretical density. Both sides of the pellet were coated with Au paste and then heated to 700 °C for 1 hour to ensure bonding to the pellet. Conductivity measurements were made in air from 370 °C to 860 °C using AC impedance spectroscopy (Hewlett Packard 4182A impedance analyzer, frequency range 10 Hz to 13 MHz, applied voltage 0.1 V). Due to the difficulty in resolving bulk and grain boundary semicircles, total conductivities are reported.[19,139]

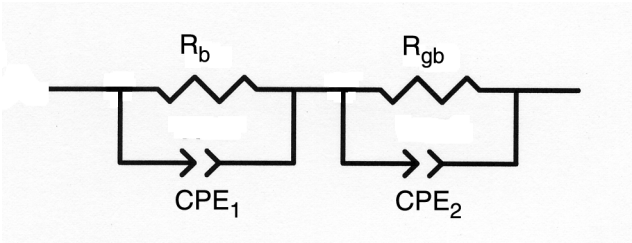

Figure 13 Equivalent circuit of the electrolyte response in the AC impedance measurement.

3.3 Atomistic Modeling

During atomistic modeling, energy minimization is employed to locate preferred atomic positions, by considering interactions between the ions represented in terms of a long-range Coulombic term combined with short-range repulsive and van der Waals interactions. The Buckingham potential is used for the short-range factor:

$$V_{ij}(r_{ij}) = A\exp\left(-\frac{r_{ij}}{\rho}\right) - \frac{C}{r_{ij}^6} \quad \textbf{(23)}$$

where r is the inter-atomic distance and A, ρ and C are empirical parameters.

The calculation of defect energies uses a shell model[141] to describe polarizability. Following the Mott-Littleton approach,[142] the lowest energy interstitial and vacancy sites are located by dividing the crystal into inner and outer regions. The inner region contains the defect, where the ions immediately surrounding the defect are relaxed explicitly, while the outer region is relaxed by quasi-continuum methods.[29,143,144] This semi-empirical atomistic modeling technique embedded in the General Utility Lattice Program (GULP)[145] can compute the lattice energy and defect structures, and examine the mechanistic features of oxygen ion transport in oxy-apatite at the atomic level.

Alternatively the bond valence (BV) approach uses correlations between the bond length and strength of chemical bonds in crystal chemistry to locate preferred ion migration pathways[146-148] such that:

$$s = \left(\frac{R}{R_o}\right)^{-N} \quad \textbf{(24)}$$

$$s = \exp\left(\frac{R_o - R}{b}\right) \quad \textbf{(25)}$$

In the generalized empirical bond valence parameters/bond lengths for cations and anions R_o,[149] a universal parameter (b = 0.37 Å)[150] and sometimes the order N are chosen to ensure that the sums of the bond valences (s) around all the ions are the same as their formal charges.[147] This technique can be applied to check if the modeled structure has fallen to a false minimum that contains significant under-bonded or over-bonded metal-centered oxygen polyhedra.

In practice, it is difficult to select a cut-off radius for the BV calculation, especially for distorted polyhedra, and thus bond softness and higher coordination shell contributions are introduced.[148] The approach is well suited for predicting Li^+ and Ag^+ ion migration pathways in $La_{2/3-x}Li_{3x}TiO_3$[151,152] and AgI[153] by assuming that immobile ions define an essentially static energy landscape for the mobile ions,[147,151] but this is not the case in apatites. For example, BV summing can only model the intra-tunnel O^{2-} diffusion path in $La_8Sr_2Si_6O_{26}$ apatite due to this limitation. Interstitial oxygen locations and movements cannot be investigated because the surrounding SiO_4 tetrahedra will distort and relax to form the SiO_4-SiO_5 units.

3.4 Conclusion: The Case for Integrated Synthesis, Characterization, Modeling and Testing

Where polycrystalline apatite electrolytes are characterized, as in this study, establishing unequivocal relationships between structure and functionality proves challenging due to the need to deconvolute the influences of secondary phases, grain boundary and pore effects, and chemical heterogeneity. While an imperfect solution, this research has used multiple experimental methods to obtain a consensus for describing the electrolytes studied. By examining the materials over a range of scales (nm to cm), the properties extracted can be considered reliable, and used to guide electrolyte design and synthesis.

In this work, polycrystalline apatites were usually prepared by solid-state sintering from the binary oxide/carbonate starting materials. The synthesis parameters (e.g. sintering temperature and time, alkali and alkaline-earth doping concentrations) were

varied systematically to relate crystal structure to conduction phenomena. While XAS, FTIR and NMR spectroscopy, and HRTEM provide more direct information of the local, atomic arrangement and coordination, care was taken to ensure that the data interpretation was consistent with X-ray and neutron diffraction that average rather large volumes. These experimental investigations provide a “static” description, and were supplemented by semi-empirical modeling to give a dynamic sense of ion migration. Finally impedance testing of oxide ion conductivity was introduced to establish clear linkages between materials processing, crystal chemistry and functionality.

Chapter 4

Results and Discussion

4.1 Extrastoichiometric Framework Oxygen in Germanate Apatite – 2*A*, 2*M* and 2*H* Electrolytes*

4.1.1 Historical Presumptions of Interstitial Oxygen Incorporation

Until recently, it has been generally assumed based on conductivity measurements,[9,15] crystallographic investigations[3,9] and semi-empirical simulations,[29] that in apatite electrolytes mobile interstitial oxygen appeared exclusively in the [001] tunnel close to the *X* anion position (Figure 14). However, these early models could not readily account for ion conduction across, as well as along, the tunnels. Nor was there a clear understanding of the manner in which extrastoichiometric oxygen lead to changes in symmetry. This situation arose, in part, because most studies focused on silicate apatites where arguably less oxygen can be incorporated, compared to germanate analogues, and the growth of single crystals was challenging.

A substantial advance in understanding was provided by León-Reina *et al.*[14] who showed that $La_{10-x}Ge_6O_{27-3/2x}$ adopts $P6_3/m$ symmetry across the compositional range $9.52 \leq 10 - x \leq 9.60$ with a phase transformation to triclinic $P\bar{1}$ at higher lanthanum contents ($9.66 \leq 10 - x \leq 9.75$). In a subsequent investigation of $La_{9.55}Si_6O_{26.32}$ and $La_{9.60}Ge_6O_{26.40}$ using neutron diffraction,[89] excess scattering in the tunnels was attributed to crystallographic sites containing interstitial oxygen at rather small occupancy factors (<0.05) in agreement with atomistic simulation.[29]

*This section published substantially as Pramana *et al.* (2007) Acta Crystallogr. B, **63**, 597-602.

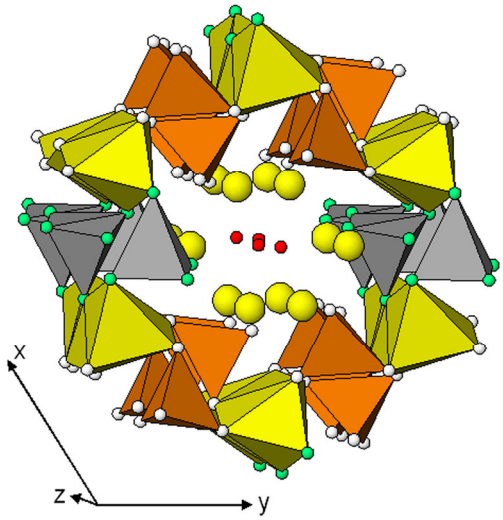

Figure 14 An [001] polyhedral representation of triclinic $La_{10}(GeO_4)_5(GeO_5)O_2$ apatite emphasizing the average structure in which face-sharing LaO_6 metaprisms (yellow) are corner connected to GeO_4 tetrahedra (brown) and GeO_5 trigonal bipyramids (grey) to create an adaptable framework. The [001] channel contains La3, La4, La5 (yellow) and O13 (red). Metaprism twisting adjusts the channel diameter as a function of stoichiometry.

Comparing the anion sublattices for a range of germanate and silicate analogues suggested that low concentrations of interstitial oxygens reside nearer the framework walls of the former, but are forced towards the tunnel centre in the latter.[29,66,89,91,114] For stoichiometric $La_8Sr_2(SiO_4)_6O_2$ oxygen ion migration through the tunnel by a 'vacancy' mechanism was calculated to be energetically favorable, while in nonstoichiometric $La_{9.33}Si_6O_{26}$ an 'interstitial' movement was preferred.[29] Indeed, both conductivity measurements and theoretical studies have focused almost solely on intra-tunnel oxygen transport. However, Nakayama and Higuchi[30] reported significant oxygen ion conduction perpendicular to the channels in single crystals of $Pr_{9.33}Si_6O_{26}$, $Nd_{9.33}Si_6O_{26}$ and $Sm_{9.33}Si_6O_{26}$.

This section describes the structure of lanthanum strontium germanate apatites containing excess oxygen, that contrary to common understanding, is most frequently located within the channel walls, rather than near the channel center.

4.1.2 Crystal Structure of $La_{10-x}Sr_x(GeO_4)_{5+x/2}(GeO_5)_{1-x/2}O_2$

It is evident that "$La_{10}(GeO_4)_6O_3$" with $x = 0$, contains an extra anion as compared to the nominal $A_{10}(BO_4)_6X_2$ formulation and in terms of descriptive crystallography, this oxygen might be located within the channels (the conventional view) or through conversion of the BO_4 tetrahedron to a BO_5 polyhedron (as in $Ba_{10}(ReO_5)_6Cl_2$ for example).[86] Rietveld analysis of powder neutron diffraction data for $La_{10}Ge_6O_{27}$ converged successfully in the lower symmetry $P\bar{1}$ rather than $P6_3/m$, as would be expected if the framework was large relative to the tunnel contents. Fourier difference (001) sections through the tunnel confirmed that two central oxygen atoms (the *X* sites) sufficiently accounted for all the scattering in this region. Similar mapping of the framework clearly revealed the remaining oxygen was located statistically at 'interstitial' positions between the $Ge3O_4$ tetrahedra with an average occupancy of 0.5 (Figure 15a).

In order to obtain reasonable Ge-O bond distances, the Ge3 atom was disordered over a nearby Ge3a site. The final crystallographic parameters distribute the interstitial oxygen O14 over 2*i* Wyckoff positions at the fractional co-ordinates ±(0.028, 0.477, 0.511) leading to a more appropriate description of this apatite as $La_{10}(GeO_4)_5(GeO_5)O_2$, rather than $La_{10}(GeO_4)_6O_3$, since the latter implies the extra oxygen is located in the channel (Table 5). Lowering the symmetry of this apatite-2*A* polymorph to *P*1 did not significantly improve the residual factors, while attempts to fit the data to previously reported models[90] containing tunnel oxygen interstitials yielded inferior refinements.

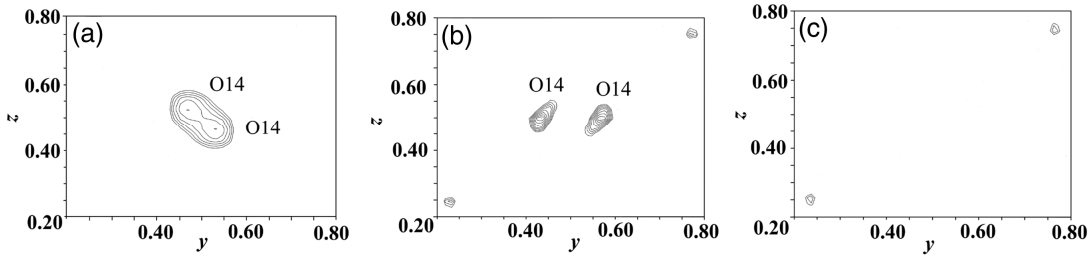

Figure 15 Nuclear density maps of the regions where framework interstitial atoms appear for (a) $[La_{10}][(GeO_4)_5(GeO_5)]O_2$, (b) $[La_9Sr][(GeO_4)_{5.5}(GeO_5)_{0.5}]O_2$, and (c) $[La_8Sr_2][(GeO_4)_6]O_2$. The concentration of extra-stoichiometric oxygen increases with higher La^{3+} content to achieve charge balance. Similar mapping around the tunnel-centre where excess oxygen is normally presumed resident did not reveal additional atoms. The slight shifts in O(14) convert the GeO_5 trigonal bipyramids in $[La_{10}][(GeO_4)_5(GeO_5)]O_2$ to square pyramids in $[La_9Sr][(GeO_4)_{5.5}(GeO_5)_{0.5}]O_2$.

Table 5 Unit cell parameters, fractional atomic coordinates, occupancies and isotropic thermal displacements of $La_{10}(GeO_4)_5(GeO_5)O_2$.

R_{wp} †	0.050	a (Å)	9.9346(7)
S_{wp}	0.5	b (Å)	9.9132(7)
R_b	0.014	c (Å)	7.3021(5)
Number of reflections	1402	α (°)	90.960(5)
Number of parameters	106	β (°)	88.079(5)
Radiation	Neutron	γ (°)	120.890(4)
Wavelength (Å)	1.8834(1)	V (Å^3)	616.79(8)

Atom	x	y	z	occupancy	B (Å^2)
La(1)	0.341(1)	0.641(1)	0.006(2)	1	0.2(2)
La(2)	0.302(1)	0.667(1)	0.508(2)	1	0.2(2)
La(3)	0.235(1)	0.993(1)	0.241(2)	1	0.4(1)
La(4)	0.010(1)	0.251(1)	0.264(2)	1	0.4(1)
La(5)	0.771(1)	0.797(1)	0.228(2)	1	0.4(1)
Ge(1)	0.398(1)	0.370(1)	0.282(2)	1	0.2(1)
Ge(2)	0.614(1)	0.015(1)	0.254(2)	1	0.2(1)
Ge(3a)	0.992(3)	0.597(3)	0.231(3)	0.5	0.2(1)
Ge(3b)	0.936(3)	0.574(3)	0.257(3)	0.5	0.2(1)
O(1)	0.293(2)	0.465(2)	0.281(2)	1	0.62(9)
O(2)	0.502(2)	0.818(2)	0.258(2)	1	0.62(9)
O(3a)	0.212(4)	0.701(5)	0.207(5)	0.5	0.62(9)
O(3b)	0.149(4)	0.665(4)	0.202(5)	0.5	0.62(9)
O(4)	0.615(2)	0.484(2)	0.295(2)	1	0.62(9)
O(5)	0.529(2)	0.135(2)	0.231(2)	1	0.62(9)
O(6a)	0.882(4)	0.389(4)	0.201(5)	0.5	0.62(9)
O(6b)	0.824(4)	0.388(4)	0.240(5)	0.5	0.62(9)
O(7)	0.362(2)	0.278(2)	0.060(2)	1	0.62(9)
O(8)	0.769(2)	0.052(2)	0.094(2)	1	0.62(9)
O(9a)	0.885(4)	0.637(4)	0.069(5)	0.5	0.62(9)
O(9b)	0.914(4)	0.661(5)	0.020(5)	0.5	0.62(9)
O(10)	0.676(2)	0.778(2)	0.549(2)	1	0.62(9)
O(11)	0.252(2)	0.901(2)	0.558(2)	1	0.62(9)
O(12a)	0.068(4)	0.300(4)	0.577(5)	0.5	0.62(9)
O(12b)	0.017(3)	0.204(4)	0.615(4)	0.5	0.62(9)
O(13)	0.004(2)	0.020(3)	0.237(3)	1	2.9(4)
O(14)	0.028(4)	0.477(4)	0.511(5)	0.5	0.62(9)

4.1.3 Polymorphic Transformations and Conductivity of $La_{10}(GeO_4)_5(GeO_5)O_2$

As $La_{10}(GeO_4)_5(GeO_5)O_2$ is heated from 200 to 1000°C, the Bragg peaks observed by powder neutron diffraction become progressively narrower and more intense (Figure 16), indicating that the symmetry is higher at elevated temperature. Figure 17 and Table 6 show the trend in unit cell parameters with temperature similar to the work by León Reina *et al.*.[154] Inflection points in *a* and *b* indicate that there are three distinct regions attributable to the polymorphic transition (triclinic 2*A* (T < 700°C) → monoclinic 2*M* (700°C < T < 800°C) → hexagonal 2*H* (T > 800°C). This analysis is supported by consideration of the interaxial angles α, β, γ and the unit cell volume. However, the discontinuity in *b* is not significant (within the accuracy of the refinement), and as the structure dilates, the transformation is anisotropic in the *ac* plane through the co-operative movement of the interstitial oxygen with the surrounding GeO_4 to create Ge_2O_9 polyhedra. This changes the metaprism twist angle (ϕ) which leads to larger metrical changes in the (001) basal plane.

These polymorphic transformations are consistent with inflections in conductivity measurements. As it was not possible to resolve bulk and grain boundary contributions, the total conductivity values are presented (Figure 17d). $La_{10}(GeO_4)_5(GeO_5)O_2$ (x = 0) showed typical behavior of a triclinic phase where relatively poor conductivity at low temperatures (2.50×10^{-5} Scm^{-1} at 500°C) is greatly improved when apatite-2*A* transforms to apatite-2*H* (3.02×10^{-2} Scm^{-1} at 800°C).[100,111] In the absence of a phase change the conductivity should vary linearly with temperature. However, a close inspection of the data suggests that for x = 0, there are three linear regions consistent with phase transformations; it is proposed that 2*A* to 2*M* conversion takes place at 620°C, followed ultimately by a 2*H* polymorph at 780°C (Figure 17d).

Table 6 Lattice parameters for $La_{10}(GeO_4)_5(GeO_5)O_2$ as a function of temperature. All refinements were carried out in $P\bar{1}$, but within error, the cell is hexagonal above 800°C, and monoclinic from 700 to 800°C. This phase transformations are expected as a consequence of framework adaptation in accordance with space group hierarchy.

Temperature (°C)	*a* (Å)	*b* (Å)	*c* (Å)	*α* (°)	*β* (°)	*γ* (°)	Volume (Å^3)
200	9.9519(2)	9.9305(2)	7.3163(1)	90.96(1)	88.10(1)	120.85(1)	620.39(1)
400	9.9633(4)	9.9446(4)	7.3291(2)	90.95(1)	88.19(1)	120.78(1)	623.55(2)
500	9.9752(2)	9.9544(2)	7.3360(1)	90.91(1)	88.26(1)	120.75(1)	625.74(1)
600	9.9850(2)	9.9652(2)	7.3434(1)	90.86(1)	88.34(1)	120.71(1)	627.96(1)
700	9.9952(5)	9.9787(4)	7.3521(3)	90.74(1)	88.50(1)	120.65(1)	630.63(3)
800	9.9795(4)	9.9789(5)	7.3615(1)	90.26(1)	89.67(1)	120.01(1)	634.79(2)
900	9.9940(1)	9.9939(1)	7.3719(1)	90.00(1)	89.96(1)	120.00(1)	637.65(1)
1000	10.0101(1)	10.0099(1)	7.3773(1)	90.00(1)	89.99(1)	120.00(1)	640.19(1)

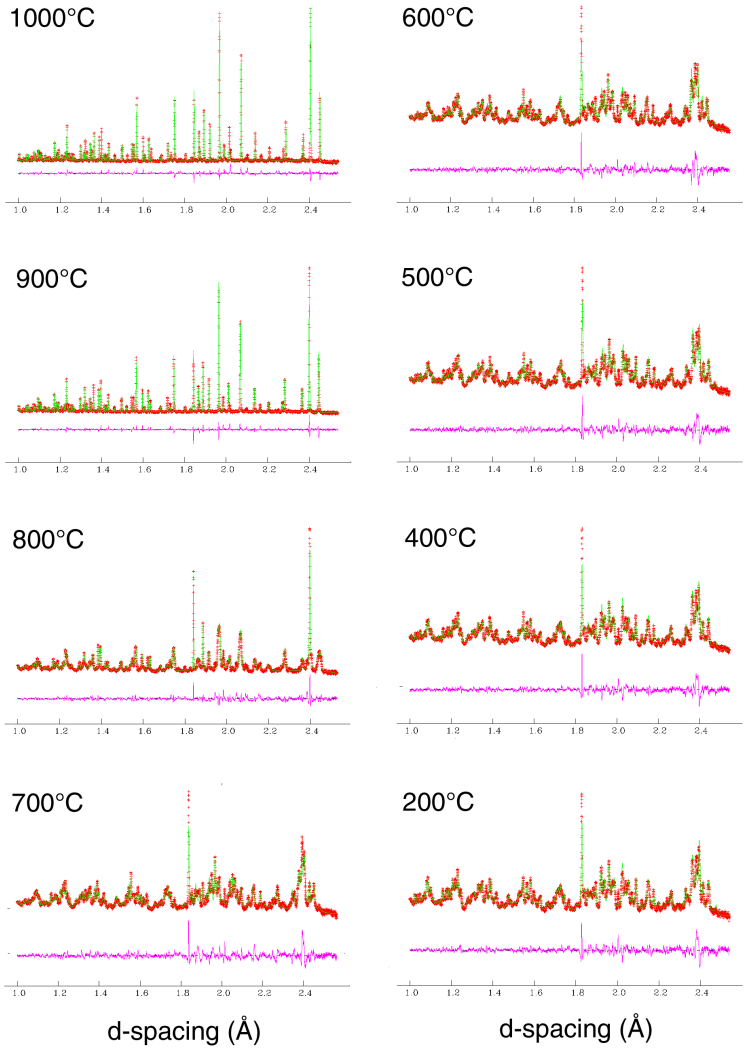

Figure 16 Rietveld refinement of neutron diffraction data of $La_{10}(GeO_4)_5(GeO_5)O_2$ as a function of temperature.

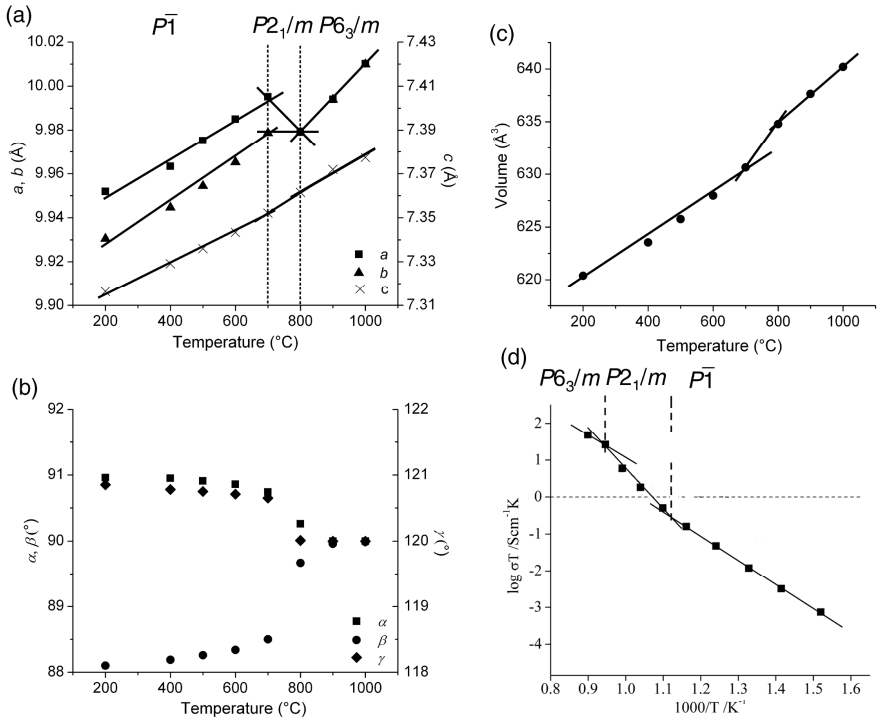

Figure 17 Temperature driven polymorphic phase transitions in $La_{10}(GeO_4)_5(GeO_5)O_2$ as reflected by changes in (a) lattice parameters (*a*, *b* and *c*), (b) interaxial angles α, β and γ, (c) unit cell volume and (d) variation of conductivities.

4.1.4 Pseudomorphic Transformations of $La_{10-x}Sr_x(GeO_4)_{5+x/2}(GeO_5)_{1-x/2}O_2$ (x = 1, 2)

The crystallographic transformations of $La_{10}(GeO_4)_5(GeO_5)O_2$ as a function of temperature, are strictly polymorphic in nature, because within the limit of detection no change in composition is involved. However, similar changes are promoted by adjusting chemistry through the incorporation of Sr. In this work, these phase changes are referred to as pseudomorphic.

According to framework taxonomy it is predicted that the additional oxygen in the intermediate apatite $La_9SrGe_6O_{26.5}$ (x = 1) will be tenanted entirely in the channel walls as $[La_9Sr_1][(GeO_4)_{5.5}(GeO_5)_{0.5}]O_2$ rather than occupy the tunnel as $[La_9Sr_1][(GeO_4)_6]O_{2.5}$. A combination of nuclear density mapping and structure refinement confirmed this presumption with the interstitial oxygen (also O14) positioned at ± [0.02(2), 0.45(2), 0.50(2)] with an occupancy of 0.25 (Tables 7 and 8, Figures 15b and 18). This pseudomorph as detailed in Section 4.2 adopts an apatite – 2*A* structure. The x = 2 neutral apatite $[La_8Sr_2][(GeO_4)_6]O_2$ is monoclinic apatite –

2*M*. All the strontium atoms partition to the framework with the tunnel sites solely occupied by lanthanum, and consequently, the complete crystallochemical formula can be expressed as $[La_2Sr_2][La_6][(GeO_4)_6]O_2$. For this compound, neutron data were adequately refined in hexagonal $P6_3/m$, but high resolution X-ray diffraction revealed a small, but unequivocal, distortion to a monoclinic metric (see Section 4.2). As expected, nuclear density mapping provided no evidence of excess oxygen within the tunnels or framework (Figure 15c).

Table 7 Crystal chemical data for apatite $La_{10-x}Sr_x(GeO_4)_{5+x/2}(GeO_5)_{1-x/2}O_2$ electrolytes.

	$La_{10}(GeO_5)(GeO_4)_5O_2$		$La_9Sr(GeO_5)_{0.5}(GeO_4)_{5.5}O_2$		$La_8Sr_2(GeO_4)_6O_2$	
	phase #1	phase #2	phase #1	phase #2	phase #1	phase #2
wt.%	64(1)	36(1)	67(1)	33(1)	46(1)	54(1)
a (Å)	9.9481(2)	9.9322(6)	9.9078(2)	9.8637(3)	9.9039(1)	9.9102(2)
b (Å)	9.9210(2)	9.9171(5)	9.8996(3)	9.9066(3)	9.9159(2)	9.9265(1)
c (Å)	7.3041(1)	7.3030(3)	7.3167(1)	7.3162(2)	7.3155(1)	7.3230(1)
α (°)	90.94(1)	90.81(1)	90.27(1)	89.54(1)	90	90
β (°)	88.03(1)	88.63(1)	89.65(1)	89.45(1)	90	90
γ (°)	120.93(1)	120.54(1)	120.00(1)	119.76(1)	120.00(1)	120.00(1)
Volume (Å^3)	617.99(2)	619.35(7)	621.50(3)	620.49(3)	622.19(2)	623.86(2)

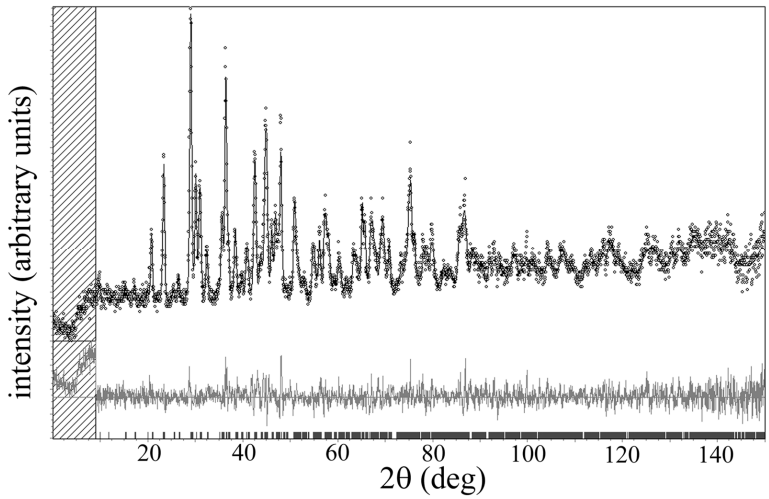

Figure 18 Rietveld plot of the neutron diffraction data of $[La_9Sr][(GeO_4)_{5.5}(GeO_5)_{0.5}]O_2$ collected at room temperature. The observed intensity data are shown by dots, with the solid line representing the calculated intensity. Differences between observed and calculated intensities are plotted beneath. Vertical markers indicate the Bragg reflections.

Table 8 Unit cell parameters, fractional atomic coordinates, occupancies and isotropic thermal displacements of $[La_9Sr][(GeO_4)_{5.5}(GeO_5)_{0.5}]O_2$.

R_{wp} †	0.097	a (Å)	9.875(2)
S_{wp}	0.6	b (Å)	9.893(2)
R_b	0.018	c (Å)	7.308(1)
Number of reflections	2796	α (°)	89.90(3)
Number of parameters	101	β (°)	89.59(2)
Neutron wavelength (Å)	1.4925(1)	γ (°)	119.96(2)
		V (Å^3)	618.5(2)

Atom	x	y	z	occupancy	B (Å^2)
La/Sr1	0.333(4)	0.675(5)	0.009(5)	0.75/0.25	1.0(3)
La/Sr2	0.300(3)	0.645(5)	0.502(4)	0.75/0.25	1.0(3)
La3	0.232(4)	0.991(3)	0.241(5)	1	0.7(2)
La4	0.012(3)	0.227(3)	0.246(5)	1	0.7(2)
La5	0.742(3)	0.763(4)	0.245(4)	1	0.7(2)
Ge1	0.423(3)	0.378(3)	0.251(4)	1	0.1(2)
Ge2	0.629(3)	0.027(3)	0.260(4)	1	0.1(2)
Ge3a	0.996(4)	0.617(5)	0.249(6)	0.75	0.1(2)
Ge3b	0.92(1)	0.59(1)	0.30(1)	0.25	0.1(2)
O1	0.296(5)	0.487(5)	0.251(7)	1	0.3(1)
O2	0.521(5)	0.840(4)	0.264(6)	1	0.3(1)
O3a	0.185(6)	0.705(6)	0.253(8)	0.75	0.3(1)
O3b	0.14(2)	0.64(2)	0.21(2)	0.25	0.3(1)
O4	0.592(4)	0.470(5)	0.255(7)	1	0.3(1)
O5	0.529(5)	0.145(5)	0.245(6)	1	0.3(1)
O6a	0.882(7)	0.387(6)	0.224(7)	0.75	0.3(1)
O6b	0.78(2)	0.34(2)	0.23(2)	0.25	0.3(1)
O7	0.346(5)	0.252(5)	0.056(4)	1	0.3(1)
O8	0.787(4)	0.080(5)	0.095(5)	1	0.3(1)
O9	0.904(5)	0.656(5)	0.077(5)	1	0.3(1)
O10	0.680(5)	0.777(4)	0.532(5)	1	0.3(1)
O11	0.251(6)	0.916(6)	0.560(6)	1	0.3(1)
O12a	0.058(6)	0.351(6)	0.555(8)	0.75	0.3(1)
O12b	0.01(2)	0.24(1)	0.59(2)	0.25	0.3(1)
O13	0.990(6)	0.997(6)	0.257(8)	1	0.5(5)
O14	0.02(2)	0.45(2)	0.50(2)	0.25	0.3(1)

For $[La_9Sr][(GeO_4)_{5.5}(GeO_5)_{0.5}]O_2$, the five-coordinate Ge polyhedron is best described as a square pyramid (GeO_5) (Figure 19). The Ge1-O4 bond distance is rather short (1.45(4)Å), however the Ge bond-valence sum gives 4.02 v.u. for this very distorted tetrahedron. Taken together, these results confirm that limited extra-stoichiometric oxygen resides in the tunnels due to bond-valence constraints, while there is a strong preference for 'interstitial' oxygen to concentrate within the framework.

$La_9Sr(GeO_4)_{5.5}(GeO_5)_{0.5}O_2$ (x = 1) shows similar behavior (inflection points at 660°C and 880°C) but with higher conductivity at lower temperature (2A) than the x = 0 electrolyte, most likely because disordered GeO_5 groups require less energy to

mobilize the "interstitial" oxygen. However, at high temperature, when both the $x = 0$ and 1 phases are hexagonal, the former exhibits higher conductivity because of the higher abundance of mobile oxygen. Hence these two factors – transient oxide ion concentration and activation energy – are crucial to optimize electrolyte performance (see Section 4.3.4). Monoclinic $La_8Sr_2(GeO_4)_6O_2$ ($x = 2$) exhibited lower conductivities (3.01 x 10^{-5} Scm^{-1}) (Table 9), typical of stoichiometric $A_{10}(BO_4)_6O_2$ systems,[91] and may be converted to a 2*H* polymorph at 490 °C, although further confirmation would be needed. $La_7Sr_3(GeO_4)_6O_2H_\delta$ shows a phase transition from 2*M* to 2*H* polymorph at 590 °C. $La_6Sr_4(GeO_4)_6O_2H_\delta$ ($x = 4$) is hexagonal and is the poorest ion conductor (1.75 x 10^{-6} Scm^{-1} at 800°C) but shows a linear change throughout as no phase change is involved. Details concerning the $x \geq 4$ compounds will be explored in Section 4.2. The activation energies for $x = 2$ and 4 are 0.83 eV and 1.72 eV, respectively. The lower activation energy for the former correlates with the higher symmetry and the observation of co-existing non-stoichiometric phases (see Section 4.2.3.2), both with low levels of interstitial oxide ions. The very high activation energy for the $x = 4$ phase is consistent with the lack of interstitial oxide ion defects, which are required to promote conductivity in these apatite systems.

4.1.5 Oxygen Conduction Mechanisms in $La_{10}(GeO_4)_5(GeO_5)O_2$

In $La_{10}(GeO_4)_5(GeO_5)O_2$ the framework interstitial oxygen that disorder over two symmetry-related sites ~0.90 Å apart promote co-operative displacements of the Ge3, O3, O6, O9 and O12 atoms to create additional split crystallographic sites all with an occupancy factor of 0.5. This structural model permits the re-analysis of oxygen migration in SOFC apatites. The Ge3a is displaced 0.51(4) Å towards the face of the tetrahedron to create a Ge3b position that bonds with O14 and forms a distorted $Ge3bO_5$ trigonal bipyramid (Figure 19). While Ge3-O3, O6, O9, O12, O14 bond lengths range from 1.88 - 2.01 Å, the framework O14 extends the Ge3b-O12b bond to 2.21 Å, pushing the O12b 0.87(5) Å towards the tunnel centre (Table 10).

The close approach of the O14 site pairs and the co-operative distortion of the GeO_5 polyhedra facilitate migration across the framework wall by rotation of the polyhedron to satisfy bond length requirements. During ion migration it is believed

that O14 displaces O12a/O12b, rather than O3a/O3b, O6a/O6b or O9a/O9b which are more strongly bonded to the lanthanum-metaprism framework (La1 and La2) (Table 10), in a manner that provides a clear pathway for the oxygen mobility along [010].

Tolchard *et al.*[29] predicted using semi-empirical methods that the lowest energy route for vacancy migration in $La_8Sr_2(SiO_4)_6O_2$ was along the tunnel with saddle-points between the O13 tunnel positions. Similarly, for O12b to move through the framework and across the tunnel an 'intermediate' position / saddle-point is required at around (0, 0, 0.5) between the statistically occupied O13 sites. The distance between O12b – (0, 0, 0.5) is about 2.10 Å. The sinusoidal-like ionic movement in the *b*-direction across the channels can be described by the motion ... O12b/O12a – O14a/O14b – O12b/O12a – (0, 0, 0.5) – O12b/O12a ... (Figure 20).

Table 9 Selected conductivities (S cm^{-1}) for $La_{10-x}(GeO_4)_{5+x}(GeO_5)_xO_2$ at 800°C.

$x = 0$	$x = 1$	$x = 2$
3.02×10^{-2}	7.35×10^{-3}	3.01×10^{-5}

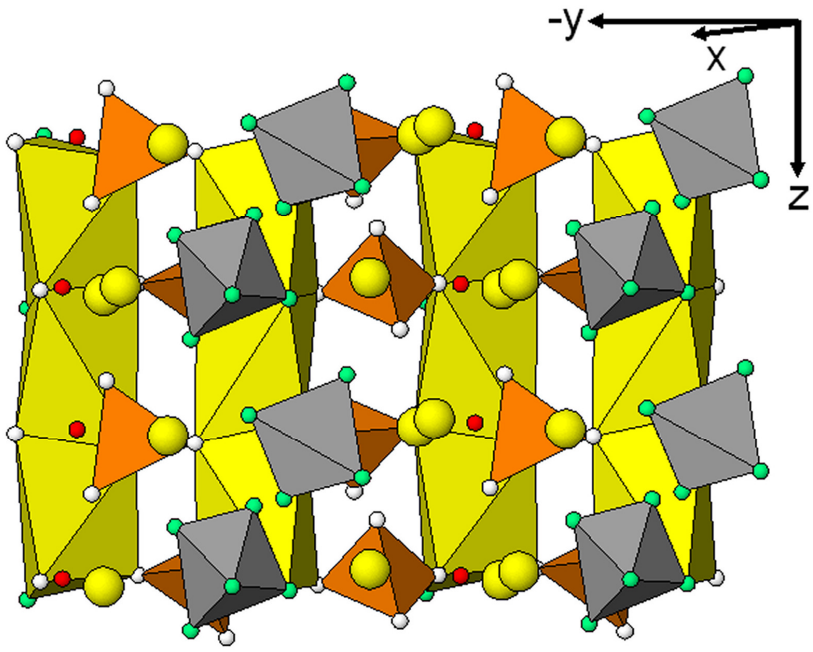

Figure 19 A polyhedral drawing demonstrating the conversion of GeO_4 tetrahedra (brown) to GeO_5 trigonal bipyramids and square pyramids (grey) in $[La_{10}][(GeO_4)_5(GeO_5)]O_2$ and $[La_9Sr][(GeO_4)_{5.5}(GeO_5)_{0.5}]O_2$, respectively, through the inclusion of the framework 'interstitial' oxygen O14 at occupancy 0.5. The LaO_6 metaprisms (yellow) are evidently distorted. The O13 tunnel oxygen is shown in red.

Table 10 Selected bond distances (Å) for $La_{10-x}Sr_x(GeO_4)_{5+x/2}(GeO_5)_{1-x/2}O_2$.

	$x = 0$	$x = 1$		$x = 0$	$x = 1$
La1–O3a	2.18(5)	2.41(6)	La5–O13	2.24(2)	2.39(4)
La1–O6b	2.39(4)	2.1(2)	La5–O7	2.42(2)	2.35(4)
La1–O3b	2.45(4)	2.3(2)	La5–O12b	2.43(4)	2.8(2)
La1–O2	2.50(2)	2.57(4)	La5–O10	2.47(2)	2.20(4)
La1–O1	2.55(2)	2.45(5)	La5–O9a	2.62(5)	2.62(6)
La1–O9	2.57(3)	2.99(4)	La5–O12a	2.69(5)	3.10(7)
La1–O5	2.57(2)	2.45(4)	La5–O4	2.71(2)	2.51(4)
La1–O6a	2.60(4)	2.56(6)	La5–O8	2.74(2)	3.14(5)
La1–O4	2.63(2)	2.71(5)	La5–O2	2.79(2)	2.65(6)
La1–O7	2.66(2)	2.91(5)	Average	2.57	2.64
Average	2.51	2.55			
			Ge1–O1	1.73(3)	2.02(6)
La2–O6b	2.11(4)	2.1(2)	Ge1–O4	1.86(2)	1.45(4)
La2–O14	2.38(3)	2.5(1)	Ge1–O7	1.80(1)	1.79(3)
La2–O3a	2.49(4)	2.39(8)	Ge1–O10	1.76(2)	2.08(4)
La2–O2	2.51(2)	2.69(4)	Average	1.79	1.84
La2–O4	2.53(2)	2.61(7)			
La2–O1	2.55(2)	2.39(5)	Ge2–O2	1.68(2)	1.62(3)
La2–O6a	2.63(4)	2.59(7)	Ge2–O5	1.79(2)	1.86(6)
La2–O11	2.63(3)	2.99(7)	Ge2–O8	1.79(2)	1.82(4)
La2–O5	2.66(2)	2.67(5)	Ge2–O11	1.81(2)	1.68(5)
La2–O3b	2.73(4)	2.6(2)	Average	1.77	1.75
La2–O14	2.83(4)	2.8(2)			
Average	2.55	2.58	Ge3a–O3a	1.88(4)	1.62(7)
			Ge3a–O6a	1.78(5)	1.98(7)
La3–O13	2.44(3)	2.41(8)	Ge3a–O9	1.79(5)	1.71(7)
La3–O12b	2.47(3)	2.6(1)	Ge3a–O12a	1.97(5)	1.61(8)
La3–O8	2.47(2)	2.54(4)	Average	1.86	1.73
La3–O10	2.49(2)	2.61(4)			
La3–O5	2.50(2)	2.55(5)	Ge3b–O3b	1.85(3)	2.12(21)
La3–O11	2.54(2)	2.48(5)	Ge3b–O6b	1.60(3)	2.25(16)
La3–O7	2.77(2)	2.61(5)	Ge3b–O9	2.01(4)	1.77(10)
La3–O3a	2.79(5)	2.63(7)	Ge3b–O12b	2.21(5)	1.68(16)
La3–O3b	2.92(4)	3.2(2)	Ge3b–O14	1.88(4)	1.74(19)
Average	2.60	2.63	Average	1.91	1.91
La4–O13	2.27(3)	2.19(6)	Split sites		
La4–O6a	2.36(5)	2.49(8)	Ge3a–Ge3b	0.51(4)	0.78(12)
La4–O12a	2.36(4)	2.51(6)	O3a–O3b	0.54(5)	0.67(14)
La4–O1	2.51(2)	2.70(4)	O6a–O6b	0.62(4)	0.87(15)
La4–O8	2.53(2)	2.26(3)	O9a–O9b	0.44(4)	0
La4–O11	2.56(2)	2.65(5)	O12a–O12b	0.87(5)	1.03(14)
La4–O12b	2.63(3)	2.5(1)			
La4–O9	2.64(4)	2.57(4)			
La4–O14	2.79(4)	2.9(2)			
La4–O6b	2.80(5)	3.0(2)			
Average	2.55	2.58			

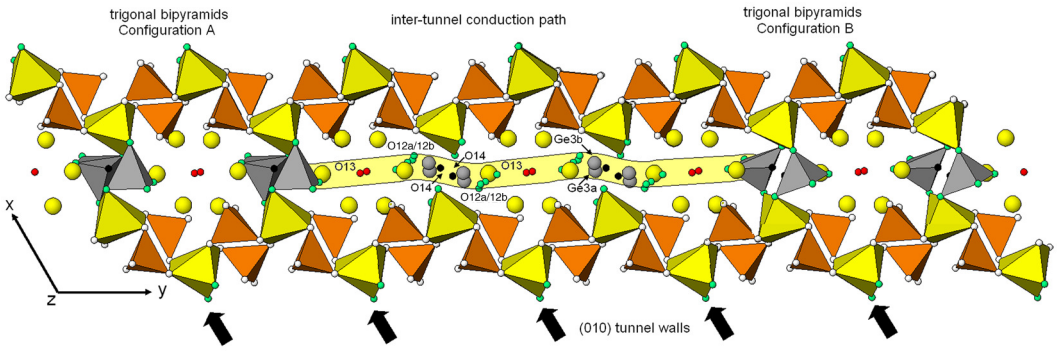

Figure 20 Proposed inter-tunnel migration path for oxygen in $La_{10}(GeO_4)_5(GeO_5)O_2$. The two configurations (A and B) of the GeO_5 trigonal bipyramids (grey) are emphasized at left and right where the complete framework is shown. In the central portion of the drawing all the statistically occupied germanium (Ge3a/Ge3b) and oxygen (O12, O13, O14) sites are included to demonstrate the feasibility of creating an ion migration (yellow band). Note that O12a/O12b is displaced towards the centre of the tunnel with ion movement proposed to take place through a saddle-point (0, 0, 0.5) between the O13 (0.004, 0.020, 0.237) atoms.

In combination with the model of Tolchard *et al.*[29] this new mechanism explains why ions can be transported both within and between tunnels. The comparatively large displacement parameter for O13 may be caused by anisotropy in thermal motion or even static displacement[93] consistent with intra- and inter-tunnel migration. It can also be postulated that the high concentration of framework 'interstitial' oxygen provides a reservoir of oxygen ions that move to the large tunnels where they more easily migrate through the structure. It is of interest that Kharton *et al.*[155] in a Mössbauer spectroscopic analysis of $La_{10}Si_5FeO_{26.5}$ electrolytes reported partial conversion of the tetrahedra to 5-coordination for a sample showing the highest oxygen conduction. Further study will be required to validate this ion migration mechanism and also the role of microstructural defects. In this regard, it is noted that at the unit cell scale the crystallochemical properties of apatites can be surprisingly intricate. It has recently been shown that natural and synthetic apatites form nanometric domains to accommodate local changes in stoichiometry,[118,156] although their recognition by high resolution transmission electron microscopy can be compromised due to the accumulation of electron beam damage. Such fine features are not readily detected by powder diffraction. Moreover, single value decomposition analysis of Rietveld parameters has shown unreliable convergence of apatite structures during refinement and therefore more sophisticated methods of geometric parameterization and *ab initio* simulation are required.[157,158] Concerning the present data, the possibility of non-stoichiometry within the La1/La2O_6 metaprisms could not be satisfactorily analyzed and should not be discounted.

It has previously been shown that superior oxygen conductivity is achieved by light doping ($x \leq 0.5$) of $[La_{10-x}Sr_x][(GeO_4)_{5+x/2}(GeO_5)_{1-x/2}]O_2$ with strontium, however the origin of the enhanced conductivity could not then be addressed.[111] It now appears that slightly sub-stoichiometric oxidised apatites provide facile pathways to inject oxygen into the conducting channels. Fully stoichiometric $[La_{10}][(GeO_4)_5(GeO_5)]O_2$ apatite, while a substantially better ion conductor than the neutral apatite $[La_8Sr_2][(GeO_4)_6]O_2$, is less disposed to release oxygen into the channel than oxidised strontian compounds because of the limited availability of empty interstitial sites to accommodate transitory O^{2-} ions.[3,16] These ideas are developed in greater detail in Section 4.3 where a range of alkaline earth doped lanthanum germanate apatite electrolytes are studied.

4.1.6 Conclusion: $La_{10}Ge_6O_{27}$ – A New Electrolyte Prototype

This structural study provides a basis for correlating conductivity measurements and atomistic simulations with crystallochemical analysis as described in Sections 4.2 and 4.3, in particular, the possible transformations when dopants are introduced. It is common practice to introduce oxygen by replacing large divalent *A*-cations (e.g. Ca, Sr, Ba) with trivalent rare earth elements, but such syntheses can yield cation-deficient apatites such as $La_{9.33}\square_{0.67}(GeO_4)_6O_2$ whose ion fluxes are not optimal. Less attention has been paid to the use of transition metals,[16,159] but their incorporation can enhance conduction,[160] and Mössbauer spectroscopy of $La_{10}Si_5FeO_{26.5}$ was consistent with partial conversion of iron tetrahedra to 5 co-ordination,[155] so that this electrolyte should be described as $[La_{10}][(SiO_4)_5(Fe^{3+}O_4)_{0.5}(Fe^{3+}O_5)_{0.5}]O_2$. Indeed, the introduction of smaller cations such as Al^{3+} and B^{3+} which favor penta-coordination generally improves conduction.[16] It may be feasible to regulate elevated oxygen levels through the addition of highly oxidised *B*-cations such as Re^{7+}. For example, doping $[La_{10}][(GeO_4)_5(GeO_5)]O_2$ according to the coupled substitution $La^{3+} + (GeO_4)^{4-} \rightarrow Ba^{2+} + (ReO_5)^{3-}$ could produce the hybrid apatites $[La_{10-x}Ba_x][(GeO_4)_{5-x}(ReO_5)_x(GeO_5)]O_2$ with potentially superior control of oxygen content during synthesis and higher conductivity even at low rhenium levels. Preliminary results from rhenium-bearing apatites are presented in Section 4.5.

4.2 Pseudomorphic Transformations in Lanthanum – Strontium Germanates*

4.2.1 Pseudomorphic Adaptations

The polymorphic $2A \rightarrow 2M \rightarrow 2H$ transformations of $La_{10}(GeO_4)_5(GeO_5)O_2$ as a function of increasing temperature were described in Section 4.1. The driver for these phase changes was the reduction in size mismatch of the framework and tunnel contents as the material is heated. At ambient, the large framework must collapse partially through metaprism twisting that leads to rotation of the BO_4/BO_5 polyhedra and a reduction in symmetry to $P\bar{1}$. It is noted that the presence of a BO_5 unit is not critical to stabilizing the $2A$ form, and for example, svabite $Ca_{10}(AsO_4)_6F_2$ is triclinic purely because ϕ is a relatively large 24.2°.[76] The polymorphic sequences are reversible and high symmetry $P6_3/m$ apatites generally provide superior oxygen mobility.[94] Therefore, modifying the chemistry of lanthanum germanate oxyapatites to favor the hexagonal metric may prove advantageous.

As already considered the partial substitution of La by Sr can stabilize $P6_3/m$ compounds, although this will lead to a reduction in interstitial oxygen content, and it is feasible to use chemical tuning to select $2A/2M/2H$ structures. These phases are referred to here as pseudomorphs, rather than polymorphs, as strictly the latter term is reserved for compositionally identical phases. It is also believed that the activation energy for ion migration is dependent on cell symmetry.[16,111]

*This section published substantially as Pramana *et al.* (2009) Dalton Trans., **39**, 8280-8291.

4.2.2 Apatite Phase Regions

4.2.2.1 Lattice Metric

The refined unit cell constants derived from laboratory powder X-ray diffraction show clear discontinuities associated with the triclinic, monoclinic and hexagonal pseudomorphic regions (Figure 21), whose structure refinements are described in Section 4.2.3.

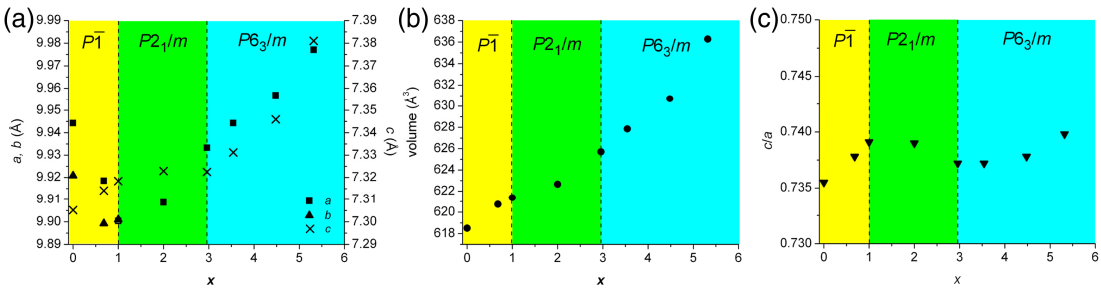

Figure 21 (a) Unit cell parameters, (b) volume and (c) c/a of $La_{10-x}Sr_xGe_6O_{27-x/2}$ refined from laboratory powder XRD. Error bars are smaller than the symbols.

As expected, the unit cell volume dilates as strontium displaces lanthanum [Sr^{2+}(VII) = 1.21Å and La^{3+}(VII) = 1.10Å][43], but is segmented into three regions. In the triclinic 2*A* region, *a* and *b* decrease while *c* increases linearly, as Sr is introduced to a limit near $La_9Sr_1(GeO_4)_{5.5}(GeO_5)_{0.5}O_2$. At higher Sr content, the monoclinic 2*M* cell shows an expansion of *a*~*b* while *c* is relatively constant. In Sr-rich apatites, Vegard's law is obeyed, but Sr_2GeO_4 appears as a second phase in $La_{10-x}Sr_xGe_6O_{27-x/2}$ ($x \geq 2.96$) with its content rising with increasing Sr addition (Figure 22). Replacing La by Sr up to *x*~ 5.32, and with ~ 23(1) wt.% of Sr_2GeO_4 as a co-existing phase, showed the apatite had not reached its solid solution limit as the lattice parameters continued to dilate.

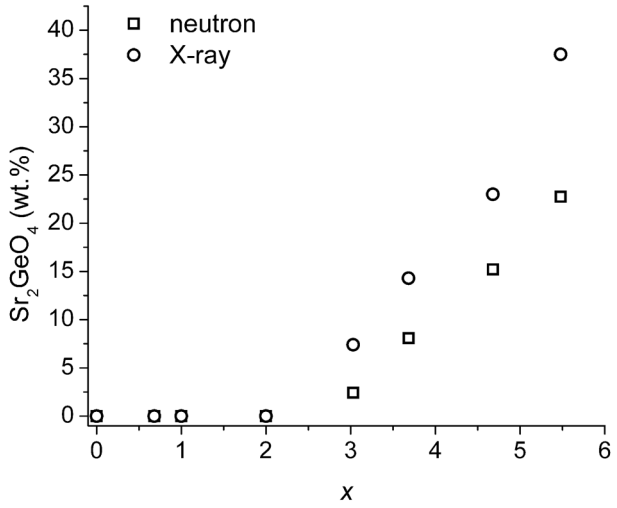

Figure 22 Second phase Sr_2GeO_4 formed as a function of *x*.

4.2.2.2 NMR

The change in symmetry as Sr displaces La was qualitatively evident in ^{139}La magic angle spinning (MAS) NMR resonances with $[La_{10}][(GeO_4)_5(GeO_5)]O_2$ showing a relatively narrow distribution of electric field gradients indicating that La is more tightly confined about a mean crystallographic position compared to $La_8Sr_2(GeO_4)_6O_2$ (Figure 23).

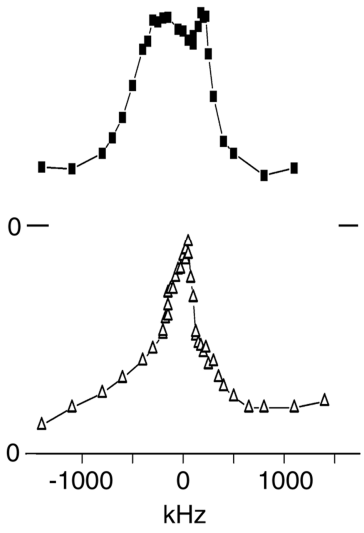

Figure 23 ^{139}La MAS NMR spectra of $[La_{10}][(GeO_4)_5(GeO_5)]O_2$ (open triangle) and $La_8Sr_2(GeO_4)_6O_2$ (filled square).

However, the multiple La sites in the apatite pseudomorphs prevent a quantitative interpretation. Proton incorporation was confirmed using ^{1}H NMR with the main signal appearing at ~7-8 ppm. (Figure 24). The slight chemical shift may be related to the change in environment as Sr replaces La.

4.2.2.3 FTIR

FTIR transmission spectra of the $La_{10-x}Sr_xGe_6O_{27-x/2}$ (nominal $0 \leq x \leq 6$) apatites did not contain O-H stretching typical of hydroxyl groups at 3570 cm^{-1}, and it can be concluded that the materials are best described as oxy-apatites.[132] Band convolution with features centered at 641, 676, 683, 693; 764, 766, 767, 787; and 845, 881, 886, 892 cm^{-1} for x = 0.00, 1.00, 2.00, 3.02 respectively can be assigned to the Ge-O vibrations in GeO_4 tetrahedra (Figures 25 and 26).[13,134]

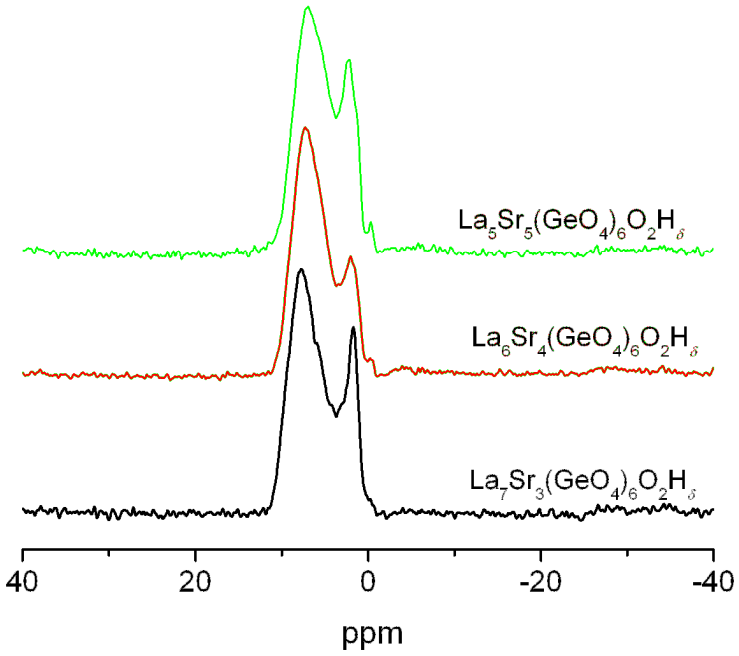

Figure 24 Solid state ^{1}H NMR data of nominal La_7Sr_3, La_6Sr_4, and $La_5Sr_5Ge_6O_{26}H_\delta$.

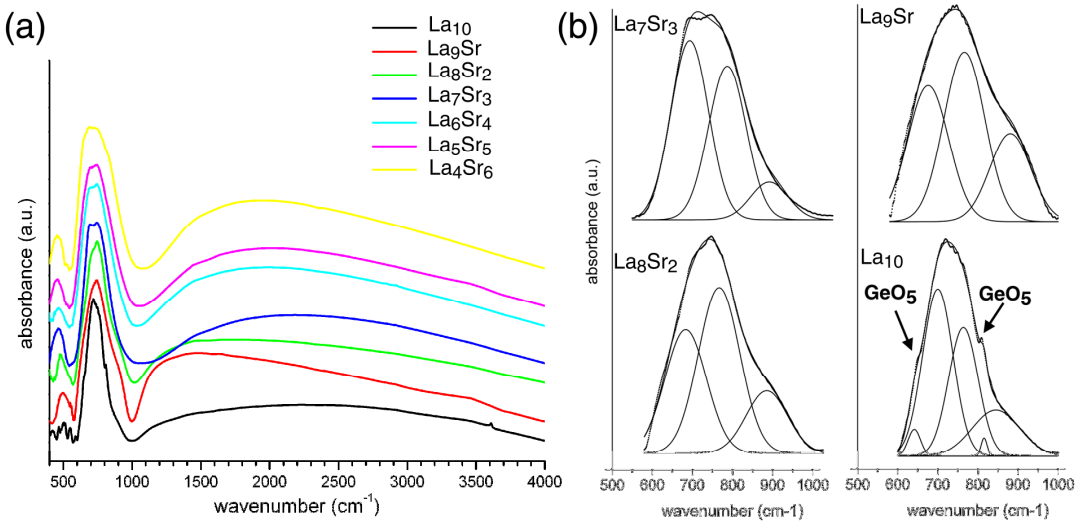

Figure 25 (a) FTIR spectra of nominal $La_{10-x}Sr_xGe_6O_{27-x/2}$ and (b) spectra deconvolution.

.

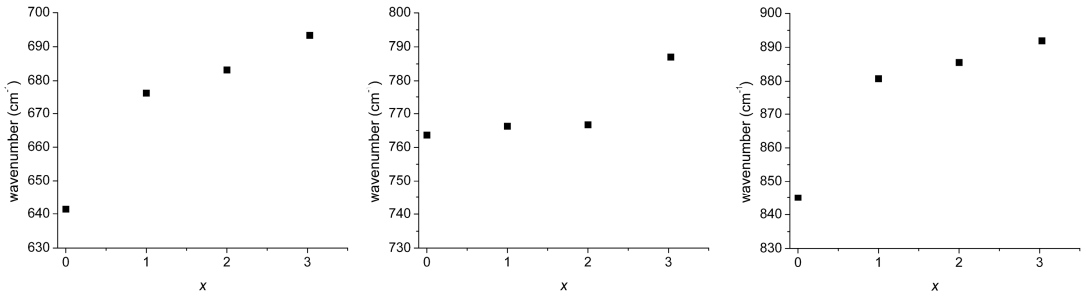

Figure 26 FTIR wavenumber shift trends with Sr composition. The lower Sr content shifts the vibration to lower wavenumbers related to the increase in Ge-O coordination number. In $La_{10}(GeO_4)_5(GeO_5)O_2$, the sharp Ge-O vibration due to the GeO_5 trigonal bipyramid appears.

For $3.54 \leq x \leq 5.32$, overlapping Ge-O oscillations arising from apatite and the second phase Sr_2GeO_4 prevented straightforward analysis. The Ge-O bonds, through coupling with *A* cations, vibrate at progressively higher frequencies as less Sr replaces La. This is consistent with observations in germanate glasses, where in $(1\text{-}x)Li_2O.xK_2O.GeO_2$ for example, the higher atomic weight dopant (K) shifts the vibration to lower wavenumbers related to the change in the co-ordination number of Ge from 4 to 6.[161] Finally, the triclinic apatite ($x = 0$) shows extra bands at 641 and 815 cm^{-1} ascribed to the incorporation of interstitial oxygen and unique Ge-O force constants associated with the GeO_5 trigonal bipyramids.

4.2.3 Pseudomorphic Crystal Structures

4.2.3.1 Triclinic Apatite – 2*A* ($0 \leq x \leq 1$)

Synchrotron X-ray diffraction confirmed an earlier, but poorer resolution neutron powder analysis where $x = 0$ was found to contain two co-existing $P\bar{1}$ phases (R_{wp} = 12.1%) : 64(1) wt.% of $[La_{9.64}][(GeO_4)_{5.54}(GeO_5)_{0.46}]O_2$ and 36(1) wt.% of $[La_{9.92}][(GeO_4)_{5.12}(GeO_5)_{0.88}]O_2$. Similarly, for $x = 1$ (R_{wp} = 11.5%) the powder contains 67(1) wt.% of $[La_{8.92}Sr_{1.08}][(GeO_4)_{5.54}(GeO_5)_{0.46}]O_2$ and 33(1) wt.% of $[La_{8.93}Sr_{1.07}][(GeO_4)_{5.535}(GeO_5)_{0.465}]O_2$ (Table 11).

4.2.3.2 Monoclinic Apatite – 2*M* ($1 \leq x \leq 2.96$)

Laboratory X-ray and neutron powder diffraction could not unambiguously identify the monoclinic pseudomorph, anticipated on the basis of subgroup-group relations, through analysis of peak splitting and residual factors. In contrast, monochromatic synchrotron diffraction data for $La_8Sr_2(GeO_4)_6O_2$ when refined in $P6_3/m$ led to high residual factors, with subsequent inspection of the plot profiles showing shoulders for several reflections indicative of lower symmetry and/or phase separation (Figure 27, Table 12).

Table 11 Unit cell parameters for nominal $La_{10}(GeO_5)(GeO_4)_5O_2$ and $La_9Sr(GeO_5)_{0.5}(GeO_4)_{5.5}O_2$ obtained from synchrotron powder X-ray diffraction.

	$La_{10}(GeO_5)(GeO_4)_5O_2$		$La_9Sr(GeO_5)_{0.5}(GeO_4)_{5.5}O_2$	
	phase #1	phase #2	phase #1	phase #2
wt.%	64(1)	36(1)	67(1)	33(1)
a (Å)	9.9481(2)	9.9322(6)	9.9078(2)	9.8637(3)
b (Å)	9.9210(2)	9.9171(5)	9.8996(3)	9.9066(3)
c (Å)	7.3041(1)	7.3030(3)	7.3167(1)	7.3162(2)
α (°)	90.94(1)	90.81(1)	90.27(1)	89.54(1)
β (°)	88.03(1)	88.63(1)	89.65(1)	89.45(1)
γ (°)	120.93(1)	120.54(1)	120.00(1)	119.76(1)
occ La1/Sr1	0.91(1)	0.98(1)	0.73/0.27(2)	0.73/0.27(2)
occ La2/Sr2	0.91(1)	0.98(1)	0.73/0.27(2)	0.73/0.27(2)
occ La3	1	1	1	1
occ La4	1	1	1	1
occ La5	1	1	1	1

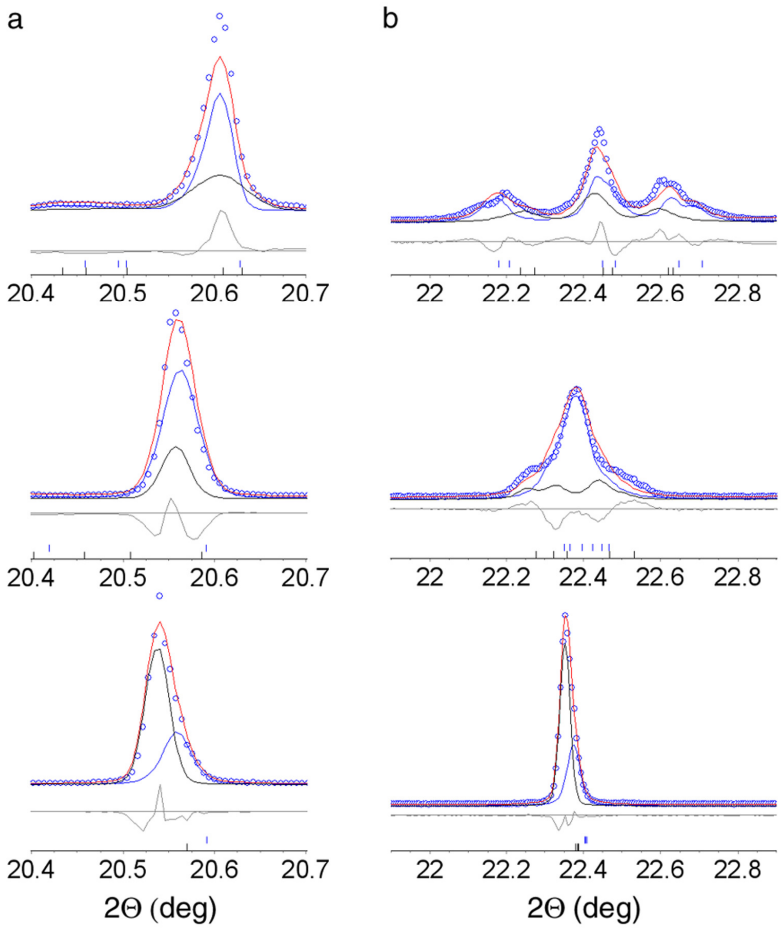

Figure 27 Rietveld plot of the synchrotron XRD patterns of $[La_{10-x}Sr_x][(GeO_4)_{5+x/2}(GeO_5)_{1-x/2}]O_2$ (x = 0 (top), 1 (middle), 2 (bottom)) showing (a) {002} and (b) {102},{1$\bar{1}$2}. The observed intensity data are shown by dots, individual phase calculated intensity by blue and black solid, total calculated intensity by red solid line. Differences between observed and calculated intensities are plotted beneath. Vertical markers indicate the Bragg reflections.

Table 12 Results of Pawley and Rietveld fits of synchrotron X-ray data for nominal $La_8Sr_2(GeO_4)_6O_2$.

# Phases	Space-group phase #1	Space-group phase #2	Pawley fits	Rietveld fits
			$R_{wp}/R_{Bp1}/R_{Bp2}$ †	$R_{wp}/R_{Bp1}/R_{Bp2}$ †
1	$P6_3/m$	-	20.0 / 5.7	22.1 / 8.0
1	$P2_1/m$	-	13.0 / 1.5	18.2 / 7.9
1	$P\bar{1}$	-	11.4 / 1.1	16.6 / 7.4
2	$P6_3/m$	$P6_3/m$	14.7 / 2.7 / 1.4	18.4 / 8.1 / 7.6
2	$P6_3/m$	$P2_1/m$	10.8 / 2.6 / 0.7	15.1 / 6.7 / 7.6
2	$P6_3/m$	$P\bar{1}$	10.2 / 1.9 / 0.7	14.5 / 8.3 / 7.6
2	$P2_1/m$	$P2_1/m$	9.9 / 0.9 / 0.6	12.9 / 6.5 / 7.0
2	$P2_1/m$	$P\bar{1}$	9.8 / 0.8 / 0.9	14.0 / 6.8 / 7.2
2	$P\bar{1}$	$P\bar{1}$	9.6 / 0.7 / 0.5	13.9 / 7.4 / 6.7

† Agreement measures are $R_{wp} = [(\Sigma_i w_i|y_{io} - y_{ci}|^2)/ \Sigma_i w_i y_{io}^2]^{1/2}$ and $R_b = \Sigma_i |I_{ko} - I_{kc}| / \Sigma_i I_{ko}$.

Pawley fitting in $P6_3/m$ did not converge satisfactorily (R_{wp} = 20%) even when the possibility of an anisotropic crystal broadening was included. Single phase Rietveld refinements using the monoclinic space group $P2_1/m$ yielded R_{wp} = 13%, while triclinic $P\bar{1}$, reduced R_{wp} by a further 1.5%. For all refinements, the (00ℓ) reflections were poorly fitted, particularly for (002) and (004), consistent with *c*-axis modulation or the co-existence of two apatites with distinct lattice metrics or symmetry. Because single crystal selected area electron diffraction (SAED) provided no evidence for an incommensurate superstructure, it was concluded that the x = 2 material was mixed phase. A Pawley fit suggested that at least one phase possessed a non-hexagonal metric, best matched with $P2_1/m$. Ultimately a comparison of R_{wp} found that a superior fit was obtained by introducing two $P2_1/m$ phases. Tables 13 and 14 show the final refined parameters and selected bond lengths for $La_{8.28}Sr_{1.72}Ge_6O_{26.14}$ and $La_{8.44}Sr_{1.56}Ge_6O_{26.22}$. Bi-phasic triclinic models produced marginal improvements in R_{wp} due to the larger number of independent parameters involved.

Table 13 Unit cell parameters, fractional atomic coordinates, occupancies and isotropic thermal displacements of the average $[La_8Sr_2][(GeO_4)_6]O_2$ structure.

	phase #1	phase #2		phase #1	phase #2
R_{wp} †	12.9		O2, 2*e*, (*x y* 1/4)		
S_{wp}	2.0		*x*	0.173(1)	
R_b	6.5	7.0	*y*	0.683(2)	
			B (Å^2)	0.10(6)	
wt.%	46(1)	54(1)			
			O3, 2*e*, (*x y* 1/4)		
a (Å)	9.9039(1)	9.9102(2)	*x*	0.504(2)	
b (Å)	9.9159(2)	9.9265(1)	*y*	0.829(1)	
c (Å)	7.3155(1)	7.3230(1)	*B* (Å^2)	0.10(6)	
γ (°)	120.00(1)	120.00(1)			
V (Å^3)	622.19(2)	623.86(2)	O4, 2*e*, (*x y* 1/4)		
			x	0.603(1)	
La/Sr1, 4*f*, (*x y z*)			*y*	0.474(2)	
x	0.3330(3)		*B* (Å^2)	0.10(6)	
y	0.6674(3)				
z	0.0004(2)		O5, 2*e*, (*x y* 1/4)		
B (Å^2)	0.44(1)		*x*	0.877(2)	
Occ La/Sr(1)	0.57/0.43(1)	0.61/0.39(1)	*y*	0.397(1)	
			B (Å^2)	0.10(6)	
La2, 2*e*, (*x y* 1/4)					
x	0.2290(3)		O6, 2*e*, (*x y* 1/4)		
y	0.9883(3)		*x*	0.518(1)	
B (Å^2)	0.51(1)		*y*	0.120(1)	
			B (Å^2)	0.10(6)	
La3, 2*e*, (*x y* 1/4)					
x	0.7592(4)		O7, 4*f*, (*x y z*)		
y	0.7676(4)		*x*	0.3470(15)	
B (Å^2)	0.51(1)		*y*	0.2507(9)	
			z	0.0600(9)	
La4, 2*e*, (*x y* 1/4)			*B* (Å^2)	0.10(6)	

x	0.0117(3)		
y	0.2436(3)	O8, 4*f*, (*x y z*)	
B (Å^2)	0.51(1)	*x*	0.0934(7)
		y	0.3474(8)
Ge1, 2*e*, (*x y* 1/4)		*z*	0.5585(9)
x	0.3994(4)	*B* (Å^2)	0.10(6)
y	0.3722(4)		
B (Å^2)	0.20(2)	O9, 4*f*, (*x y z*)	
		x	0.7569(9)
Ge2, 2*e*, (*x y* 1/4)		*y*	0.0757(15)
x	0.9733(4)	*z*	0.0677(9)
y	0.5999(4)	*B* (Å^2)	0.10(6)
B (Å^2)	0.20(2)		
		O10, 2*e*, (*x y* 1/4)	
Ge3, 2*e*, (*x y* 1/4)		*x*	0.998(6)
x	0.6284(4)	*y*	0.994(6)
y	0.0273(4)	*B* (Å^2)	0.10(6)
B (Å^2)	0.20(2)		
O1, 2*e*, (*x y* 1/4)			
x	0.304(1)		
y	0.477(1)		
B (Å^2)	0.10(6)		

† Agreement measures are $R_{wp} = [(\Sigma_i w_i|y_{io} - y_{ci}|^2)/ \Sigma_i w_i y_{io}^2]^{1/2}$, $S_{wp} = (R_{wp} / R_{exp})$ and $R_b = \Sigma_i |I_{ko} - I_{kc}| / \Sigma_i I_{ko}$.

Table 14 Selected bond lengths of the average $[La_8Sr_2][(GeO_4)_6]O_2$.

	phase #1	phase #2		phase #1	phase #2
La/Sr1–O1	2.534(7)	2.536(7)	La4–O1	2.651(7)	2.653(7)
La/Sr1–O2	2.472(10)	2.474(10)	La4–O5	2.478(21)	2.480(21)
La/Sr1–O3	2.460(8)	2.462(8)	La4–O8 [x 2]	2.445(7)	2.447(7)
La/Sr1–O4	2.570(16)	2.573(16)	La4–O9 [x 2]	2.592(7)	2.594(7)
La/Sr1–O5	2.599(16)	2.601(16)	La4–O10	2.412(8)	2.414(8)
La/Sr1–O6	2.623(6)	2.626(6)	Average	2.516	2.518
La/Sr1–O7	2.885(14)	2.886(14)			
La/Sr1–O8	2.891(6)	2.893(6)	Ge1-O1	1.726(12)	1.727(12)
La/Sr1–O9	3.131(16)	3.134(16)	Ge1-O4	1.744(9)	1.746(9)
Average	2.685	2.687	Ge1-O7 [x 2]	1.740(8)	1.742(8)
			Average	1.738	1.739
La2–O2	2.788(19)	2.791(19)			
La2–O6	2.480(9)	2.481(9)	Ge2-O2	1.724(9)	1.725(9)
La2–O7 [x 2]	2.651(8)	2.654(8)	Ge2-O5	1.740(10)	1.742(10)
La2–O9 [x 2]	2.431(8)	2.434(8)	Ge2-O8 [x 2]	1.737(8)	1.738(8)
La2–O10	2.319(8)	2.320(8)	Average	1.735	1.736
Average	2.536	2.538			
			Ge3-O3	1.723(9)	1.724(9)
La3–O3	2.880(19)	2.882(19)	Ge3-O6	1.743(13)	1.744(13)
La3–O4	2.526(19)	2.529(19)	Ge3-O9 [x 2]	1.738(8)	1.739(8)
La3–O7 [x 2]	2.469(9)	2.471(9)	Average	1.736	1.737
La3–O8 [x 2]	2.657(9)	2.660(9)			
La3–O10	2.304(8)	2.306(8)			
Average	2.566	2.568			

4.2.3.3 Hexagonal Apatite – 2*H* ($2.96 \leq x \leq 5.32$)

$La_{10-x}Sr_xGe_6O_{27-x/2}$ ($2.96 \leq x \leq 5.32$) crystallized in $P6_3/m$. Neutron scattering difference Fourier maps and site refinements of the tunnel anion sites at (0 0 z) with z~0 for all compositions invariably showed 'negative' density consistent with charge neutrality being partially achieved by inclusion of ^1H according to the altervalent substitution:

$$La^{3+} + O^{2-} \rightarrow Sr^{2+} + OH^-$$

The refined proton occupancies were 0.16(3), 0.11(3), 0.26(5) and 0.19(6) for x = 2.96, 3.54, 4.48, 5.32, respectively. As the concentrations of protons are relatively small, a significant incoherent scattering contribution to the neutron diffraction background was not expected. The final refined parameters and selected bond lengths for $La_{10-x}Sr_xGe_6O_{27-x/2}$ ($2.96 < x < 5.32$) are collated in Tables 15 and 16.

Table 15 Unit cell parameters, fractional atomic coordinates, occupancies and isotropic thermal displacements of $[La_{10-x}Sr_x][(GeO_4)_6]O_2H_\delta$ ($2.96 \leq x \leq 5.32$).

	x = 2.96	x = 3.54	x = 4.48	x = 5.32
R_{wp} †	0.184	0.178	0.172	0.185
S_{wp}	1.1	1.1	1.1	1.1
R_b	0.044	0.036	0.042	0.037
a (Å)	9.9353(3)	9.9500(4)	9.9588(4)	9.9766(5)
c (Å)	7.3247(3)	7.3362(4)	7.3491(5)	7.3740(5)
V (Å^3)	626.16(5)	628.99(6)	631.22(7)	635.63(8)
c/a	0.7372	0.7373	0.7380	0.7391
ϕ (°)	23.58	24.06	25.12	25.03
La/Sr1, 4*f*, (1/3 2/3 z)				
z	0.001(1)	0.999(1)	0.004(2)	0.003(2)
B (Å^2)	0.9(1)	1.1(2)	1.2(2)	1.8(2)
Occ La/Sr1	0.62/0.38(10)	0.67/0.33(10)	0.63/0.37(10)	0.96/0.04(10)
La/Sr2, 6*h*, (x y 1/4)				
x	0.2344(7)	0.2360(8)	0.2383(9)	0.2427(11)
y	0.9883(7)	0.9884(8)	0.9878(9)	0.9886(12)
B (Å^2)	0.5(1)	1.0(1)	1.0(1)	1.0(2)
Occ La/Sr2	0.76/0.24(7)	0.63/0.37(8)	0.50/0.50(8)	0.14/0.86(8)
Ge1, 6*h*, (x y 1/4)				
x	0.4000(7)	0.3987(7)	0.3973(8)	0.3954(10)
y	0.3707(6)	0.3696(6)	0.3707(7)	0.3676(9)
B (Å^2)	0.7(1)	0.6(1)	1.0(1)	1.3(2)
O1, 6*h*, (x y 1/4)				
x	0.312(1)	0.312(1)	0.310(1)	0.312(1)
y	0.485(1)	0.485(1)	0.485(1)	0.485(1)

B (Å^2)	1.4(1)	1.7(1)	2.2(1)	2.4(1)
O2, 6*h*, (*x y* 1/4)				
x	0.604(1)	0.603(1)	0.601(1)	0.599(1)
y	0.475(1)	0.475(1)	0.473(1)	0.468(1)
B (Å^2)	1.4(1)	1.7(1)	2.2(1)	2.4(1)
O3, 12*i*, (*x y z*)				
x	0.3393(8)	0.3392(8)	0.3373(9)	0.3386(11)
y	0.2467(8)	0.2457(9)	0.2443(10)	0.2456(12)
z	0.0624(7)	0.0640(8)	0.0644(9)	0.0636(11)
B (Å^2)	1.4(1)	1.7(1)	2.2(1)	2.4(1)
O4, 4*e*, (0 0 *z*)				
z	0.211(3)	0.204(3)	0.203(4)	0.204(5)
B (Å^2)	2.6(5)	2.3(4)	3.6(6)	3.6(7)
Occ	0.50(1)	0.50(1)	0.50(1)	0.50(1)
H1, 4*e*, (0 0 *z*)				
z	0.05(2)	0.03(3)	0	0
B (Å^2)	2.6(5)	2.3(4)	3.6(6)	3.6(7)
Occ	0.16(3)	0.11(3)	0.26(5)[§]	0.19(6)[§]

[†] Agreement measures are $R_{wp} = [(\Sigma_i w_i|y_{io} - y_{ci}|^2)/ \Sigma_i w_i y_{io}^2]^{1/2}$, $S_{wp} = (R_{wp} / R_{exp})$ and $R_b = \Sigma_i |I_{ko} - I_{kc}| / \Sigma_i I_{ko}$.

[§] H1, 2*b*, (0 0 0)

Table 16 Selected bond lengths of $[La_{10-x}Sr_x][(GeO_4)_6]O_2H_\delta$ ($2.96 \leq x \leq 5.32$).

	x = 2.96	*x* = 3.54	*x* = 4.48	*x* = 5.32
La/Sr1–O1 [x 3]	2.497(8)	2.517(11)	2.506(9)	2.503(11)
La/Sr1–O2 [x 3]	2.574(9)	2.568(12)	2.580(11)	2.576(16)
La/Sr1–O3 [x 3]	2.956(8)	2.957(9)	2.977(9)	2.976(11)
Average	2.676	2.681	2.688	2.685
La/Sr2–O1	2.732(8)	2.727(8)	2.704(10)	2.719(11)
La/Sr2–O2	2.504(9)	2.494(12)	2.493(13)	2.501(17)
La/Sr2–O3 [x 2]	2.448(6)	2.461(7)	2.457(7)	2.456(10)
La/Sr2–O3 [x 2]	2.625(7)	2.615(10)	2.615(9)	2.632(14)
La/Sr2–O4	2.406(4)	2.431(9)	2.461(8)	2.503(13)
Average	2.541	2.543	2.543	2.557
Ge1-O1	1.749(13)	1.746(14)	1.742(17)	1.741(20)
Ge1-O2	1.753(10)	1.762(11)	1.754(13)	1.761(16)
Ge1-O3 [x 2]	1.740(6)	1.733(7)	1.747(7)	1.733(9)
Average	1.746	1.744	1.748	1.742
O4-O4	0.56(5)	0.67(4)	0.69(5)	0.68(7)
O4-H1	1.20(7)	1.30(18)	1.49	1.51

4.2.4 Changes in Local Structure

X-ray absorption near edge structure (XANES) and extended X-ray absorption fine structure (EXAFS) spectra measured at the Ge *K*-edge were consistent with the presence of GeO_5 in the $x = 0$ triclinic pseudomorph. The $x = 1$ and 2 samples show identical XANES features while $x = 0$ more intensely absorbs at position A in Figure 28a and the nearby shoulder at B is modified; these features are indicative, respectively, of higher numbers of oxygen neighbors, and a difference in next-neighbor structure around Ge. The fitting results show that in passing from $[La_8Sr_2][(GeO_4)_6]O_2$ to $[La_{10}][(GeO_4)_5(GeO_5)]O_2$, the coordination number and bond-length of the first Ge-O shell increased slightly consistent with the presence of GeO_5 or GeO_6 in addition to GeO_4 (Table 17, Figure 28).[12,162] These trends, while at the limit of the precision of the technique, are believed to be significant in a relative sense, as all three samples were analyzed in the same way. From GeO_4 to GeO_6, the higher coordination corresponds to a larger average Ge-O distance, and consequently, the most evident changes are between $x = 0$ and $x = 1$. The increase of Debye-Waller factors is also consistent with a wider range of Ge-O coordinations in low x samples. Fitting the first Ge-O shells with Ge-O coordinations (IV) and (VI) was attempted, but the result was unsatisfactory as the amount of GeO_5 or GeO_6 was small. The EXAFS results agree with predictions by atomistic modelling.[29,144]

HRTEM images of $La_5Sr_5(GeO_4)_6O_{0.5}$ collected along [0001] were used to investigate local cation order/disorder. Figure 29 shows that in the [0001] projection the *p*6 plane-group is observed, consistent with the space-group $P6_3/m$. In the central part of the image, electron beam damage is evident, but disorder was not observed, even in thicker crystals. HRTEM conducted at 300/400 keV would be useful to confirm these results.[163]

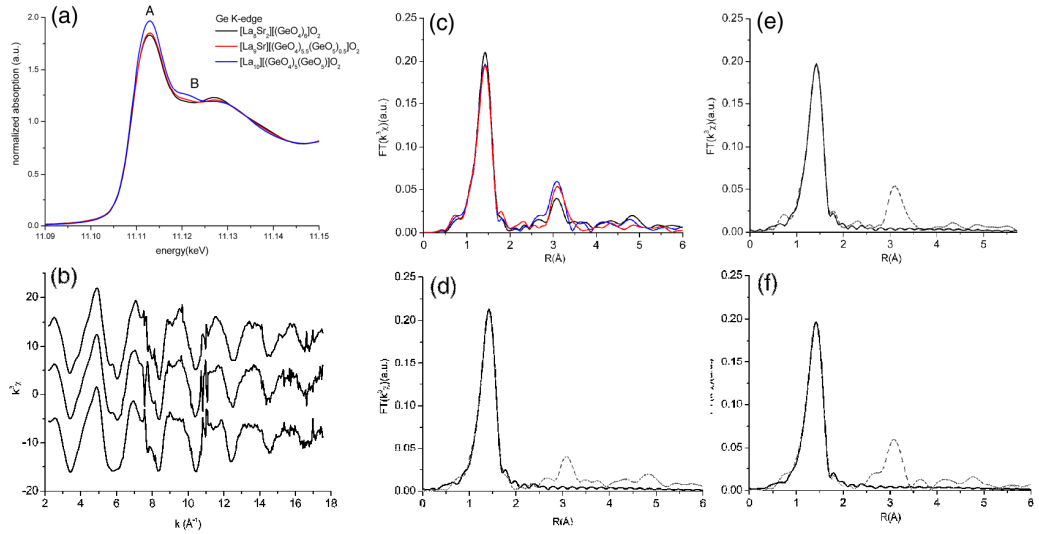

Figure 28 (a) Ge *K*-edge XANES spectra of $[La_{10-x}Sr_x][(GeO_4)_{5+x/2}(GeO_5)_{1-x/2}]O_2$ (x = 0, 1 and 2 for blue, red and black lines). The white line and the shoulder are indicated by A and B, (b) Ge *K*-edge XAFS (k3 weighed) of x = 0 (bottom), x = 1 (middle), x = 2 (top), (c) Fourier transform of the Ge *K*-edge XAFS data of x = 0 (blue line), x = 1 (red line), x = 2 (black line); (d-f) experimental and fitted data of the first coordination of x = 0, 1, 2 respectively (dash line = experimental data; solid line = calculated data).

Table 17 Coordination number, bond distances and Debye-Waller factors of the first Ge-O coordination for $[La_{10-x}Sr_x][(GeO_4)_{5+x/2}(GeO_5)_{1-x/2}]O_2$ (x = 0, 1 and 2).

	$x = 2$	$x = 1$	$x = 0$
coordination number (CN) (±10% $_{relative}$)	4.0	3.9	4.3
idealized CN	4.00	4.08	4.17
bond distances (Å)	1.75_1	1.75_5	1.76_2
D-W factor (x 10^3 Å^2) (±10%$_{relative}$)	2.5	2.7	3.2

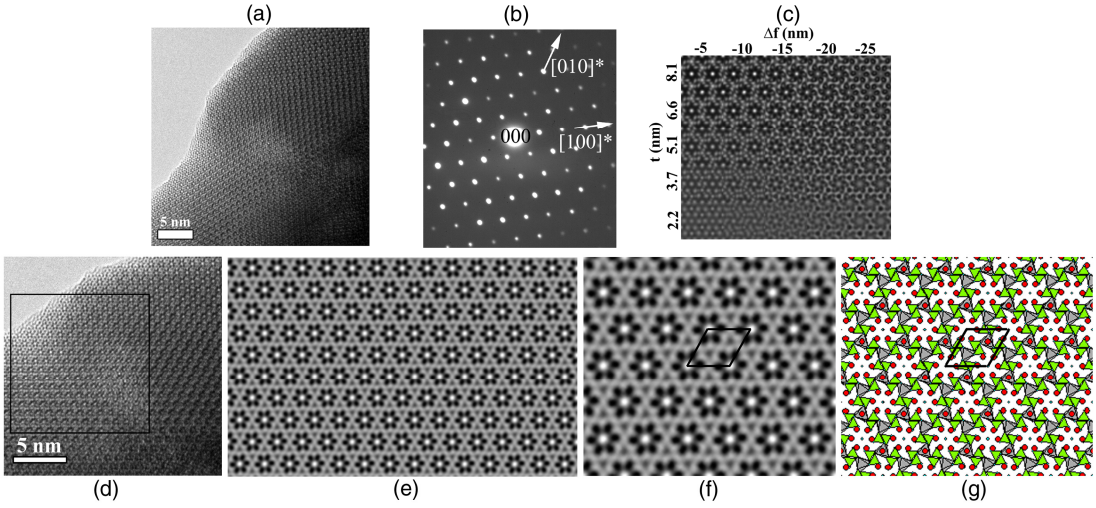

Figure 29 (a) [0001] high-resolution electron micrograph collected from $La_5Sr_5(GeO_4)_6O_{0.5}$ thin crystal wedges with (b) selected area electron diffraction; (c) calculated [0001] using multislice simulation with different thickness (t) and defocus (Δf), (e) Fourier-processed impositioning *p*6 symmetry. The Fourier region was developed within the square in (d), (f) enlarged region of the processed image and (g) the correlated apatite structure. All input crystal and atomic parameters were derived from refined X-ray diffraction data.

4.2.5 Framework Adaptation and Twist Angle

Adherence to strict three-dimensional periodicity prevents the introduction of more than 2 oxygens in the centre of the large apatite tunnel, and for example in $P6_3/m$, either the 2*a* or 2*b* site is fully occupied, or the 4*e* position is statistically half occupied. Contrariwise, *X*-anion vacancies are well known in lacunar apatites such as $Na_2Pb_8(PO_4)_6\square_2$,[82] although the tunnel is not vacant but filled with Pb^{2+} stereographically active lone pair electrons; indeed all examples of lacunar apatites and polysomes contain either Pb^{2+} or Bi^{3+}. Consequently, the appearance of $La_4Sr_6(GeO_4)_6\square$ with empty tunnels is unlikely, but partial occupancy is feasible. ^1H NMR provides direct evidence of protons, that may be surface-H_2O, absorbed OH^-, or "interstitial H" (Figure 24), but as OH vibrations were not detected by IR spectroscopy it can be surmised free protons are present. As Sr^{2+} replaces La^{3+} additional positive charges are required for charge balance, and it is believed this was achieved by the protons, as there was no evidence for more exotic charge balancing mechanisms (e.g. tunnel peroxide). Additional La^{3+} was not regarded as a viable alternate charge balance mechanism since there should not be significant error in the refined La/Sr occupancies. Moreover, TGA shows a small but constant trend for greater mass loss at higher Sr concentration. This mass loss occurred at elevated temperature, and was not complete at 1000 °C, consistent with the removal of lattice protons, rather than surface absorbed OH^- or H_2O (Figure 30).

Structural modeling through neutron powder refinement and difference Fourier mapping requires H^+ for charge balance as the oxygen sites are fully occupied, with the tunnel site partially occupied by "OH^-" that displaces O^{2-} leading to reasonable *R*-factors. However, the amount of H per formula unit at (0 0 *z*) determined by neutron diffraction is lower than expected to achieve neutrality; 0.64, 0.44, 0.52, 0.38 for x = 2.96, 3.54, 4.48, 5.32, respectively. It was therefore concluded that the additional cations are primarily delocalized protons, as Fourier mapping did not show deficient scattering nodes, except for the hydrogen located at (0 0 *z*) (Figure 31, Table 18).

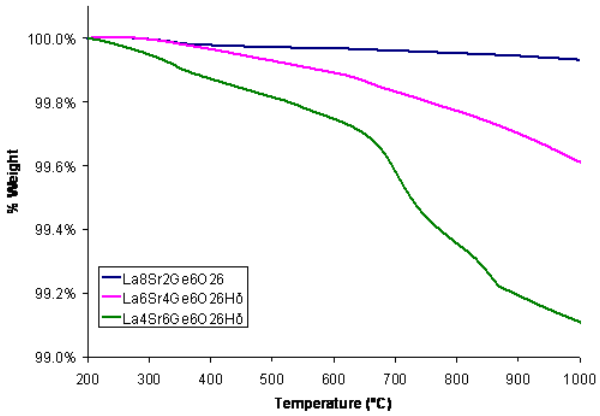

Figure 30 TGA plots for nominal $La_8Sr_2Ge_6O_{26}$, $La_6Sr_4Ge_6O_{26}H_\delta$, and $La_4Sr_6Ge_6O_{26}H_\delta$.

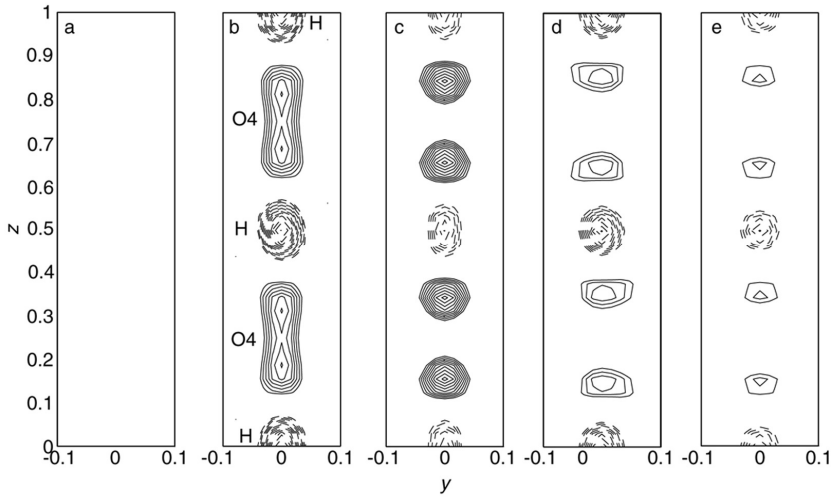

Figure 31 Nuclear density maps of the regions at x = 0 (solid = scattering excess, dash = scattering deficit) where the tunnel oxygens split to 4*e* (0,0,*z*) and H were detected at (0,0,*z*; *z*~0) of $[La_{10-x}Sr_x][(GeO_4)_6]O_2H_\delta$ (a) x = 2, (b) x = 2.96, (c) x = 3.54, (d) x= 4.48, (e) x = 5.32.

Table 18 Total hydrogen distributed in the $[La_{10-x}Sr_x][(GeO_4)_6][O_2][H_\delta]$ apatite lattice.

Refined x	Total H^+ for charge	hydroxyl H^+	Free H^+
2.96	0.96	0.64	0.32
3.54	1.54	0.44	1.10
4.48	2.48	0.52	1.96
5.32	3.32	0.38	2.94

This conclusion was also supported by analysis of the metaprism twist angle (ϕ) which is a qualitative, and in some cases semi-quantitative, predictor of apatite distortion and deviation from expected stoichiometry.[25,75] In reviewing apatites, it has been found that as the average crystal radii ratio increases, the average twist angle becomes less acute to accommodate larger framework and/or smaller tunnel ions.[25] When protons are not included in the analysis, this general trend was not followed,

but by introducing the free proton content for charge balance, and placing these in the tunnel, the expected relationship appeared (Figure 32).

Apatite pseudomorphism arises to satisfy the bonding requirements of the A^{I} and B cations as their size changes relative to the A^{II} and X species.[75] In the pure lanthanum germanate system ($x = 0$), apatite-2A crystallizes in $P\bar{1}$ to accommodate framework interstitial oxygen that promotes unusually large $A^{I}O_6$ metaprism twisting ($\phi_3 \sim 29°$) and creates GeO_5 trigonal bipyramids containing statistically split O sites in $P\bar{1}$. To compensate for the obtuse ϕ_3, the remaining twist angles become more acute (~20-22°) (Figure 33).

The principle substitution mechanisms for the strontium-doped lanthanum germanate apatite pseudomorphs and their compositional stability fields are:

apatite – 2A, 2M	$La^{3+} + 1/2\ O^{2-}{}_{int_{framework}} \rightarrow Sr^{2+} + 1/2\ \square_{O^{2-}}$	$0 \leq x \leq 2$
apatite – 2M	$La^{3+} + O^{2-} \rightarrow Sr^{2+} + OH^{-}$	$2 \leq x \leq 2.5$
apatite – 2M, 2H	$La^{3+} + \square_{int_{tunnel}} \rightarrow Sr^{2+} + H^{+}{}_{int_{tunnel}}$	$2.5 \leq x \leq 6$

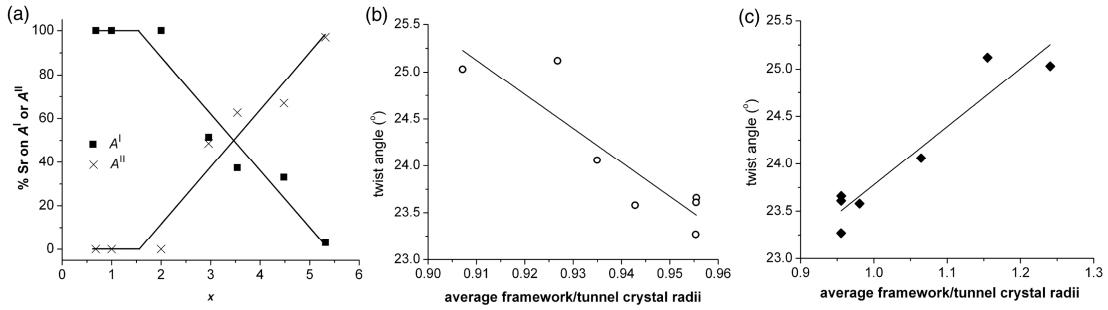

Figure 32 Crystallochemical properties including (a) partitioning coefficient of Sr over A^{I} and A^{II} crystallographic sites, and twist angle as a function of the average framework to tunnel crystal radii (b) without considering the existence of proton and (c) after placing the proton in the tunnel. The inclusion of tunnel protons leads to a trend consistent with all other apatites.

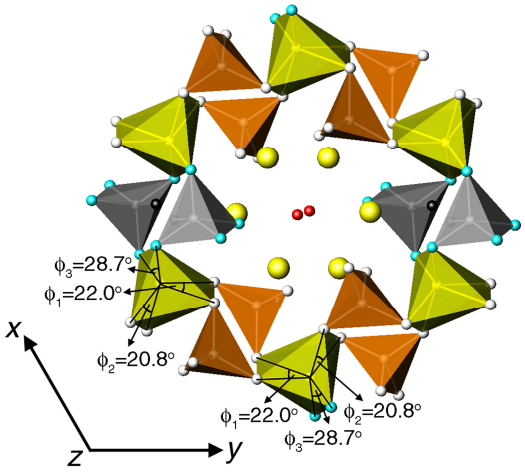

Figure 33 An [001] polyhedral representation of triclinic $La_{10}(GeO_4)_5(GeO_5)O_2$ apatite emphasizing the average structure in which face-sharing LaO_6 metaprisms (yellow) are corner connected to GeO_4 tetrahedra (brown) and GeO_5 trigonal bipyramids (grey) to create an adaptable framework. Metaprism twisting (ϕ) adjusts the channel diameter as a function of stoichiometry such that large ϕ collapses the framework, reduces tunnel dimensions, and decreases oxygen mobility.

This series of apatite phase transformations is somewhat analogous to perovskite systems, where for example in $LaAlO_3$[164] and $Ba_3BSb_2O_9$ (*B* = Ca, Sr, Ba),[165] the monoclinic $P2_1/m$ pseudomorph intervenes between triclinic and hexagonal end-members. Similarly, when $CaTiO_3$ is heated from 23 to 1447°C, a transformation from orthorhombic *Pbnm* ϕ_x^- = 8-12° → tetragonal *I*4/*mcm* ϕ_z^- = 5-8° → cubic *Pm*3*m* ϕ_z^- < 5° proceeds where ϕ is the octahedral tilt angle.[166] For both apatites and perovskites subgroup-group relationships can guide the detection of changes of symmetry, while the magnitude of metaprism twisting and octahedral tilting can be used to assess the reliability of pseudomorph structure refinements.

4.2.6 Conclusion: Importance of Pseudomorph Transitions and Ionic Conductivity

During ion migration the flux and pathway of the mobile species are a direct consequence of crystallographic structure, with the motion conforming to symmetry constraints and bond strength. For example, in perovskites ionic conductivity of $LaGa_{0.8}Mg_{0.2}O_{2.9}$ (7.23×10^{-2} Scm^{-1}) and $La_{0.9}Sr_{0.1}Ga_{0.9}Mg_{0.1}O_{2.9}$ (5.00×10^{-2} Scm^{-1}) is greater in these high symmetry phases compared to lower symmetry $LaGaO_3$

(insulator) and $La_{0.8}Sr_{0.2}GaO_{2.9}$ (3.97×10^{-3} Scm^{-1}). In these cases, mobility is enhanced by oxygen vacancies created by introducing lower valence cations in place of La^{3+} and Ga^{3+}.[167,168] Analogously, in high conductivity apatites, interstitial oxygen and/or A^I cation vacancies are essential.[3,90,169] However, excessive or heterogeneous dopant concentrations can create defect clusters that reduce conductivity.[111] In apatite the conductivity is somewhat anisotropic and favored along [001] with ionic motion promoted by large diameter tunnels.[30] On the other hand, intra-tunnel conduction (perpendicular to *c*)[30] is significant, and promoted by interstitial oxygen that partially converts the $A^I_4(BO_4)_6$ framework to $A^I_4(BO_5)(BO_4)_5$ in $La_{10}(GeO_4)_5(GeO_5)O_2$[130] and results in larger tunnel diameters. Modeling studies have suggested that this intra-tunnel conduction is significantly enhanced in the germanate apatites.[144]

Tunnel enlargement can also be achieved at elevated temperatures through a reduction of ϕ, that in turn leads to higher symmetry ($2A \rightarrow 2M \rightarrow 2H$) and enhanced conductivity. Conversely, increasing pressure is expected to compress the tunnel and lower conductivity although this has yet to be validated experimentally.[25] Kendrick and Slater[94] used this approach in designing a lower temperature, high conduction hexagonal $La_8Y_2Ge_6O_{27}$ apatite, notionally in $P6_3/m$, and containing split oxygen sites with twist angles of 15.8° and 21.2°, averaging as 18.5°.[170] This small ϕ effectively expands the tunnel diameter. Therefore, crystallochemical mechanisms that enlarge the tunnel at ambient conditions are sought, when the framework size is small relative to the tunnel. These features are elegantly illustrated by the conductivity profile for the $La_{10}(GeO_4)_5(GeO_5)O_2$,[100] where the low temperature triclinic cell (high ϕ) has relatively low conductivity while the high temperature hexagonal cell (small ϕ) has high conductivity. As noted in Section 4.1, the slope of the conductivity plot suggests an intermediate monoclinic cell (intermediate ϕ). As this section discusses the strontium-doped lanthanum germanate, other alkaline earth dopants with similar valence (Ca and Ba) were studied to better understand the pseudomorphic transformations and ionic conduction (Section 4.3).

4.3 Crystal Chemistry and Optimization of Conductivity in 2*A*, 2*M* and 2*H* Alkaline Earth Lanthanum Germanate Oxyapatite Electrolyte Polymorphs*

4.3.1 Alkaline Earths in Oxyapatite Electrolytes

Initially, the development of apatite electrolytes focused on variants with *A*-cation vacancies ($RE_{9.33}\square_{0.67}Si_6O_{26}$), sometimes coupled with extrastoichiometric oxygen $RE_{9.33+x}\square_{0.67-x}Si_6O_{26+3x/2}$ (*RE* = La, Pr, Nd, Sm, Gd, Dy).[9-11,93,108,171,172] Here, alkaline earths (*AE*) are introduced to study the mobility of "excess" oxygen when combined with stoichiometric *A*-cation occupancy. In this case, the $RE_8AE_2Si_6O_{26}$ parent structure with low ionic conductivity[3] shows improved performance when oxygen is injected as:

$$AE^{2+} \rightarrow RE^{3+} + \tfrac{1}{2}\, O^{2-} \quad \textbf{(26)}$$

The position of oxygen and its migration mechanism in extrastoichiometric apatites are the subject of debate because the total interstitial oxygen per formula unit is ≤ 1 complicating the direct observation of dynamic cooperative movements of Si/GeO_4 tetrahedra.[16,89,90,130,144] In Sr-doped lanthanum germanate apatites (Sections 4.1 and 4.2), pseudomorphic transformations correlate with ionic conductivity. In this supplementary study the relationship between stoichiometry, structural pseudomorphism and oxygen mobility in lanthanum germanate oxyapatites was clarified by combining powder X-ray diffraction, conductivity measurements and atomistic simulation of the mechanisms of calcium and barium incorporation in $La_{10-x}(Ca,Ba)_xGe_6O_{27-x/2}$ apatites. Given the important role of disorder and oxygen content in solid electrolyte applications this investigation tests the viability of *ab initio* mobility models through comparison with crystallographic data.

*This section published substantially as Pramana *et al.* (2010) Solid State Ionics, **181**, 1189-1196.

4.3.2 Lattice Metric

4.3.2.1 Calcium Doped Lanthanum Germanate Apatites

The refinement of $La_{10-x}Ca_xGe_6O_{27-x/2}$ ($x > 1.5$) using $P6_3/m$ resulted in the best fit with respect to R_b and R_{wp} compared to the alternative settings of $P6_3$ as reported in $La_{9.33}Si_6O_{26}$ and $La_9AESi_6O_{26+\delta}$,[112] and $P\bar{3}$ for $La_{9.33}Si_6O_{26}$ and $La_8Sr_2Si_6O_{26}$.[139] When calcium [Ca^{2+}(VII) = 1.06 Å] replaces lanthanum [La^{3+}(VII) = 1.10 Å][43] the unit cell contracts (Figure 34). For nominal $x = 1$, the refinement was modeled using a two-phase apatite assemblage containing 38(1) wt.% $La_{9.20}Ge_6O_{26}H_\delta$ (a = 9.888(1) Å and c = 7.2729(9) Å) and 62(1) wt.% $La_{8.5}Ca_{1.5}Ge_6O_{26.25}$ (a = 9.8786(5) Å and c = 7.2317(5) Å) (Figure 35, Tables 19 and 20). In the absence of a pseudomorphic transformation the cell metrics versus composition must accord with Vegard's law and vary directly over the solid solution range. However, when compared to $La_{10}Ge_6O_{27}$ which is known to be triclinic $P\bar{1}$, it becomes evident that the lattice parameter trends can be divided into two regions where $La_{10-x}Ca_xGe_6O_{27-x/2}$ crystallized in $P\bar{1}$ for $0 < x < 1.5$ and $P6_3/m$ for $x > 1.5$ (Figure 34), although the precise phase boundary ($x \sim 1.5$) remains to be determined. The solid solubility limit of Ca in La-Ge-apatite was reached at $x \sim 2.5(1)$, beyond which the unit cell volume no longer changed, refined Ca occupancy stabilized within e.s.ds, and $Ca_5Ge_3O_{11}$ was increasingly abundant through to a nominal $x = 6$ (Figure 36).

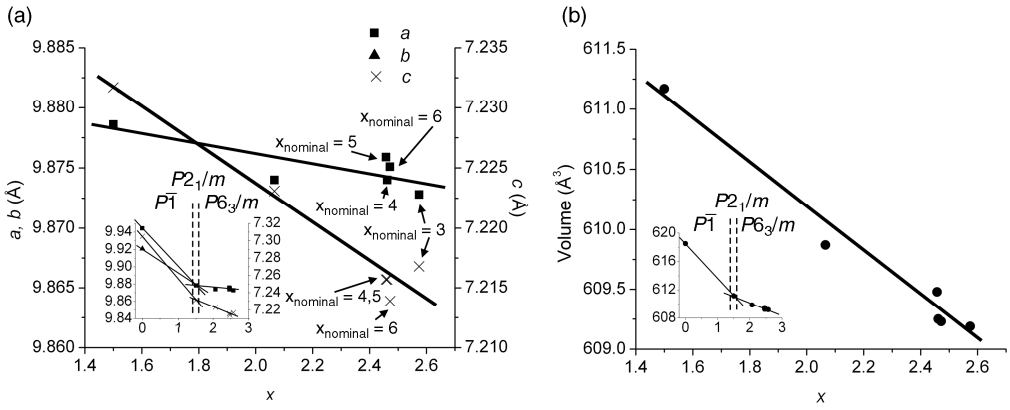

Figure 34 Trends of (a) lattice parameters and (b) volume of calcium doped lanthanum germanate apatites. The inflection indicates the pseudomorphic transformation from $P\bar{1}$ to $P6_3/m$ at a Ca loading of $x \sim 1.5$. The existence of an intervening $P2_1/m$ apatite stable over a narrow compositional range cannot be excluded, and would be expected on the basis of space group systematics.

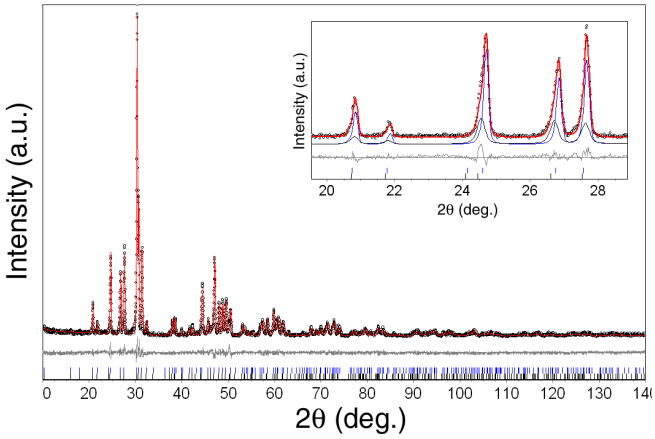

Figure 35 Rietveld XRD refinement plot of nominal $La_9CaGe_6O_{26.5}$ collected at room temperature. The observed intensities are shown by circles with a red solid line representing the calculated intensity. Differences between observed and calculated intensities are plotted beneath. Vertical markers indicate the Bragg reflections. (inset) Rietveld plot at low 2θ emphasizing the bi-phasic apatite mixture (38(1) wt.% $La_{9.20}Ge_6O_{26}H_\delta$ and 62(1) wt.% $La_{8.5}Ca_{1.5}Ge_6O_{26.25}$ averaging to $La_{8.77}Ca_{0.93}Ge_6O_{26.14}H_\delta$) recognized from asymmetric peak profiles such as $(002)_{triclinic}$ at 2θ = 24.6°.

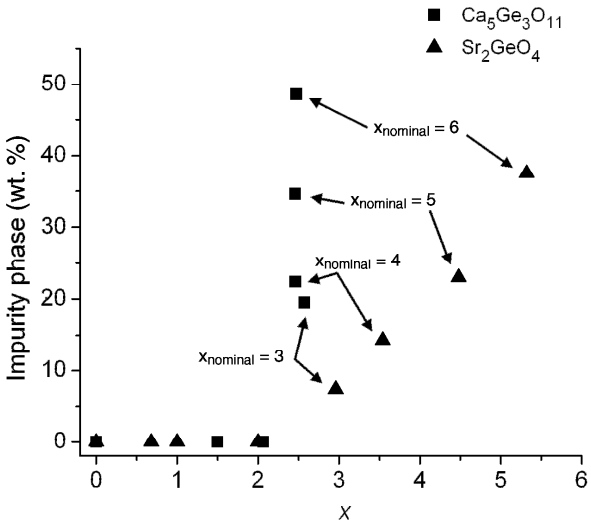

Figure 36 Impurity phases in $La_{10-x}(Ca,Sr)_xGe_6O_{27-x/2}$.

Table 19 Selected bond distances of $La_{10-x}Ca_xGe_6O_{27-x/2}$.

x	0	1.5	2	3	4	5	6
La/Ca1-O1 (x3)	2.41(1)		2.456(7)	2.443(8)	2.450(8)	2.449(8)	2.44(1)
La/Ca1-O2 (x3)	2.49(2)		2.58(1)	2.61(2)	2.59(1)	2.57(2)	2.57(2)
La/Ca1-O3 (x3)	3.01(1)		2.99(1)	3.05(1)	3.01(1)	2.93(1)	2.98(1)
La/Ca1-O5 (x3)		2.64					
La/Ca1-O5 (x3)		3.11					
La/Ca2-O1	2.908(9)		2.787(7)	2.816(8)	2.788(7)	2.801(8)	2.80(1)
La/Ca2-O2	2.60(1)		2.47(1)	2.43(2)	2.46(2)	2.48(2)	2.50(2)
La/Ca2-O3 (x2)	2.446(8)		2.455(7)	2.476(9)	2.427(8)	2.419(8)	2.434(9)
La/Ca2-O3 (x2)	2.574(8)		2.550(6)	2.494(9)	2.569(8)	2.619(7)	2.577(8)
La/Ca2-O4	2.357(5)		2.343(4)	2.371(5)	2.356(4)	2.351(6)	2.347(3)
Ge1-O1	1.73(2)		1.73(1)	1.73(1)	1.73(1)	1.73(1)	1.73(2)
Ge1-O2	1.73(1)		1.725(8)	1.717(9)	1.728(8)	1.730(9)	1.72(1)
Ge1-O3 (x2)	1.728(7)		1.728(6)	1.726(8)	1.731(7)	1.730(7)	1.725(8)
Ge1-O5 (x2)		1.87					

Table 20 Unit cell and atomic parameters of $La_{10-x}Ca_xGe_6O_{27-x/2}$.

Nominal *x*	0*	1.5	2	3	4	5	6
a (Å)	9.888(1)	9.8786(5)	9.8740(2)	9.8728(2)	9.8740(2)	9.8759(2)	9.8751(2)
c (Å)	7.2729(9)	7.2317(4)	7.2231(2)	7.2168(2)	7.2157(2)	7.2157(2)	7.2139(2)
Volume (Å^3)	615.8(2)	611.17(8)	609.87(2)	609.19(3)	609.25(3)	609.48(2)	609.23(3)
R_{wp}/R_b (%)	13.1/2.7	13.1/2.5	12.8/2.9	13.7/2.6	13.6/2.1	13.7/2.2	13.5/2.2
wt%	38(1)	62(1)	100	81(1)	78(1)	65(1)	51(1)
La/Ca1							
4*f* (⅓ ⅔ *z*)							
z	0.0014(8)		0.9984(7)	0.9983(9)	0.0000(8)	0.9989(8)	0.0000(9)
Occ	0.80	0.64/0.36(1)	0.512/0.488(6)	0.502/0.498(7)	0.509/0.491(6)	0.510/0.490(7)	0.511/0.489(8)
Beq	1.9(1)		0.67(6)	0.71(7)	0.88(7)	0.81(6)	0.68(7)
La/Ca2							
6*h* (*x y* ¼)							
x	0.2297(2)		0.2305(2)	0.2311(2)	0.2308(2)	0.2308(2)	0.2307(3)
y	0.9860(3)		0.9869(2)	0.9870(3)	0.9874(3)	0.9872(3)	0.9868(3)
Occ	1.00	0.99/0.01(1)	0.981/0.019(6)	0.903/0.097(8)	0.917/0.083(8)	0.917/0.083(8)	0.914/0.086(9)
Beq	0.60(6)		0.85(3)	0.44(4)	0.58(4)	0.60(4)	0.54(4)
Ge1							
6*h* (*x y* ¼)							
x	0.4037(4)		0.4026(3)	0.4016(3)	0.4017(3)	0.4021(3)	0.4014(4)
y	0.3755(4)		0.3743(3)	0.3745(3)	0.3737(3)	0.3739(3)	0.3738(4)
Occ	1		1	1	1	1	1
Beq	1.17(9)		0.43(6)	0.21(7)	0.41(7)	0.34(7)	0.43(8)
O1							
6*h* (*x y* ¼)							
x	0.333(1)		0.320(1)	0.323(1)	0.319(1)	0.321(1)	0.321(1)
y	0.505(1)		0.4929(9)	0.496(1)	0.4923(9)	0.494(1)	0.494(1)
Occ	1		1	1	1	1	1
Beq	4.6(3)		2.7(2)	4.2(3)	3.2(3)	2.5(3)	2.8(3)
O2							
6*h* (*x y* ¼)							
x	0.605(1)		0.6043(9)	0.602(1)	0.604(1)	0.604(1)	0.602(1)
y	0.467(2)		0.481(2)	0.485(2)	0.482(2)	0.480(2)	0.478(2)
Occ	1		1	1	1	1	1
Beq	4.6(3)		2.7(2)	4.2(3)	3.2(3)	2.5(3)	2.8(3)
O3							
12*i* (*x y z*)							
x	0.331(2)		0.333(1)	0.325(1)	0.331(1)	0.340(1)	0.334(1)
y	0.2434(9)		0.2417(6)	0.236(1)	0.2431(8)	0.2481(8)	0.2440(9)
z	0.0694(9)		0.0696(8)	0.076(1)	0.067(1)	0.062(1)	0.067(1)
Occ	1		1	1	1	1	1
Beq	4.6(3)		2.7(2)	4.2(3)	3.2(3)	2.5(3)	2.8(3)
O4							
4*e* (0 0 *z*)							
z	0.212(5)		0.24(2)	0.206(5)	0.216(5)	0.23(1)	0.24(4)
Occ	0.5		0.5	0.5	0.5	0.5	0.5
Beq	2(1)		1.5(6)	1(1)	0.5(9)	2.9(8)	3(1)
O5							
12*i* (*x y z*)							
x		0.028					
y		0.477					
z		0.511					
Occ		0.02					
Beq		0.1					

4.3.2.2 Barium Doped Lanthanum Germanate Apatites

An attempt to introduce Ba into $La_{10-x}Ba_xGe_6O_{27-x/2}$ apatite with $x > 3$ was unsuccessful as the powders melted during sintering and lower temperatures (1100 °C) yielded poorly crystalline, mixed phase products. The unit cell parameters of Ba-doped apatites should increase as Ba is larger than La [Ba^{2+}(VII) = 1.38 Å and La^{3+}(VII) = 1.10 Å][43] (Figure 37, Tables 21 and 22), and a pseudomorphic transformation for $x \sim 1 - 2$ is expected, as observed for the Ca and Sr analogues. While this could not be confirmed directly, an inflection in cell parameters at $x \sim 2$ is consistent with the crystallization of $P2_1/m$ apatite – 2*M*. Furthermore, the partitioning of Ba and La between the framework and tunnel could not be established using X-ray diffraction as Ba^{2+} and La^{3+} are isoelectronic, with neutron diffraction studies required to allow differentiation. At the highest Ba loadings ($x = 3$) 3 wt.% Ba_2GeO_4 was present and this composition is assumed near the solubility limit.

Table 21 Unit cell and atomic parameters of $La_{10-x}Ba_xGe_6O_{27-x/2}$.

x	1	2	3
a (Å)	9.9558(2)	9.9916(2)	10.0267(2)
c (Å)	7.3643(2)	7.4069(2)	7.4149(2)
Volume (Å^3)	632.14(3)	640.38(3)	645.58(3)
R_{wp}/R_b (%)	15.4/3.4	15.7/3.4	17.2/3.0
wt%	100	100	97(1)
La/Ba1 4*f* (⅓ ⅔ *z*)			
z	0.0000(6)	0.9999(7)	0.9999(6)
Occ	0.75/0.25	0.5/0.5	0.25/0.75
Beq	1.57(5)	0.71(4)	0.39(4)
La/Ba2 6*h* (*x y* ¼)			
x	0.2301(2)	0.2304(2)	0.2323(2)
y	0.9883(3)	0.9886(3)	0.9881(3)
Occ	1/0	1/0	1/0
Beq	0.91(4)	0.51(4)	0.44(4)
Ge1 6*h* (*x y* ¼)			
x	0.3992(3)	0.3984(4)	0.4010(4)
y	0.3724(3)	0.3715(4)	0.3726(3)
Occ	1	1	1
Beq	0.69(8)	0.42(8)	0.23(8)
O1 6*h* (*x y* ¼)			
x	0.312(1)	0.321(1)	0.315(1)
y	0.485(1)	0.492(1)	0.486(1)
Occ	1	1	1
Beq	2.8(3)	2.3(3)	1.6(3)
O2 6*h* (*x y* ¼)			
x	0.599(1)	0.596(1)	0.600(1)

y	0.483(2)	0.482(2)	0.474(2)
Occ	1	1	1
Beq	2.8(3)	2.3(3)	1.6(3)
O3 12*i* (*x y z*)			
x	0.340(1)	0.341(1)	0.338(1)
y	0.2471(8)	0.2487(8)	0.2493(8)
z	0.068(1)	0.066(1)	0.067(1)
Occ	1	1	1
Beq	2.8(3)	2.3(3)	1.6(3)
O4 4*e* (0 0 *z*)			
z	0.203(7)	0.208(7)	0.194(8)
Occ	0.5	0.5	0.5
Beq	4(1)	2(1)	7(2)
O5 12*i* (*x y z*)			
x	0.028		
y	0.477		
z	0.511		
Occ	0.04		
Beq	0.1		

Table 22 Selected bond distances of $La_{10-x}Ba_xGe_6O_{27-x/2}$.

x	1	2	3
La/Ba1-O1 (x3)	2.516(8)	2.508(9)	2.532(9)
La/Ba1-O2 (x3)	2.66(1)	2.68(2)	2.61(2)
La/Ba1-O3 (x3)	2.97(1)	2.97(1)	3.01(1)
La/Ba1-O5 (x3)	2.66		
La/Ba1-O5 (x3)	3.14		
La/Ba2-O1	2.746(9)	2.839(9)	2.787(8)
La/Ba2-O2	2.48(2)	2.50(2)	2.56(2)
La/Ba2-O3 (x2)	2.507(8)	2.515(9)	2.506(9)
La/Ba2-O3 (x2)	2.612(7)	2.637(8)	2.655(8)
La/Ba2-O4	2.376(7)	2.382(6)	2.426(9)
Ge1-O1	1.73(1)	1.73(1)	1.74(1)
Ge1-O2	1.724(9)	1.71(1)	1.73(1)
Ge1-O3 (x2)	1.724(7)	1.727(8)	1.728(7)
Ge1-O5 (x2)	1.92		

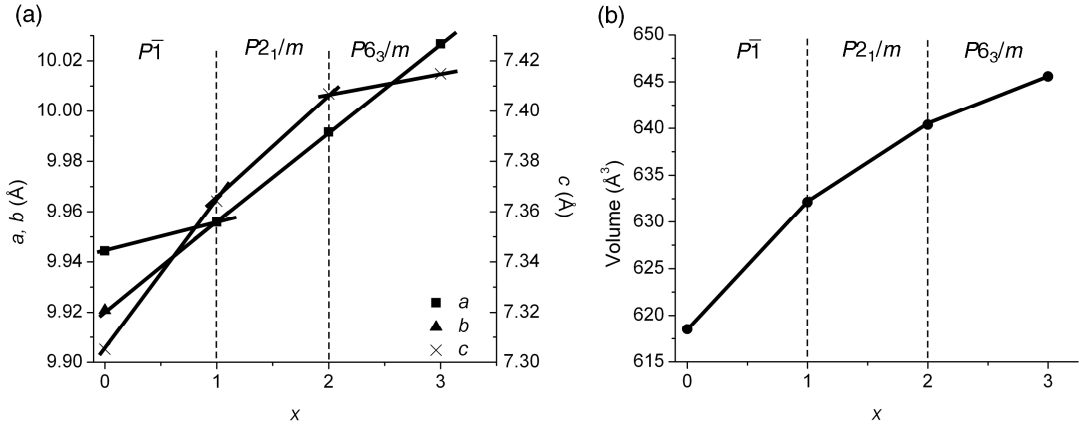

Figure 37 Trends of (a) lattice parameters and (b) volume of barium doped lanthanum germanate apatites. The inflection indicates the pseudomorphic transformation from $P\bar{1}$ to $P6_3/m$ as Ba dopant increases. $P2_1/m$ may be anticipated at $1 < x < 2$, as the trend is not linear.

4.3.3 Mechanisms of *AE* Incorporation in Lanthanum Germanate Apatites

The ionic radii of Ca, Sr and Ba differ from La by -3.6%, +10.0% and +25.5%, respectively, and the incorporation of Ca is anticipated to be favorable over a wide solubility range. However, at least for the $La_{10-x}Ca_xGe_6O_{27-x/2}$ studied here, Ca solid solubility was much lower (x_{max} ~ 2.5) than for Sr and Ba. Specifically, Ca differed from Sr in $La_{10-x}Sr_xGe_6O_{27-x/2}$ where x_{max} ~ 5.3 although Sr_2GeO_4 co-crystallized[64] (Figure 38) and Sr preferentially entered the A^I position at lower content and A^{II} at higher loading, as discussed in Section 4.2. In $La_{10-x}Ca_xGe_6O_{27-x/2}$, the larger La^{3+} occupied the less voluminous, but higher co-ordination (CN = 7) A^{II} site completely to better deploy charge, while the smaller Ca^{2+} ions occupied the larger A^I site with an effective co-ordination number of 6.[173] The different substitution mechanism is also evident in the *c/a* ratio, which for the Ca compound decreases linearly, while in the Sr analogue increases ($0 < x < 1$), becomes constant ($1 < x < 2$) and finally decreases ($2 < x < 5.3$). As expected, Ba shows a similar *c/a* trend to Sr where it both increases ($0 < x < 2$) and decreases ($2 < x < 3$). As X-rays are insensitive for determining the low *Z* ion (O) position, particularly when co-existing with high *Z* ions (La, Ba), the twist angle does not show any correlation with the average framework to tunnel radii (Figure 39). Neutron diffraction will be required to investigate metaprism distortion.

The appearance of Ba_2GeO_4 in $La_{10-x}Ba_xGe_6O_{27-x/2}$ (x ~ 3) is analogous to the Sr_2GeO_4 impurity in $La_{10-x}Sr_xGe_6O_{27-x/2}$ ($x > 2$)[64] and Ba_2SiO_4 in $La_{10-x}Ba_xSi_6O_{27-x/2}$ ($x > 2$).[174] However, $Ca_5Ge_3O_{11}$ was found in $La_{10-x}Ca_xGe_6O_{27-x/2}$ ($x > 2$) as a second phase. In contrast, Berastegui *et al.*[12] reported that in Ca and Sr-doped apatites, $CaGe_2O_5$ and $SrGeO_3$ appeared above the solubility limit.

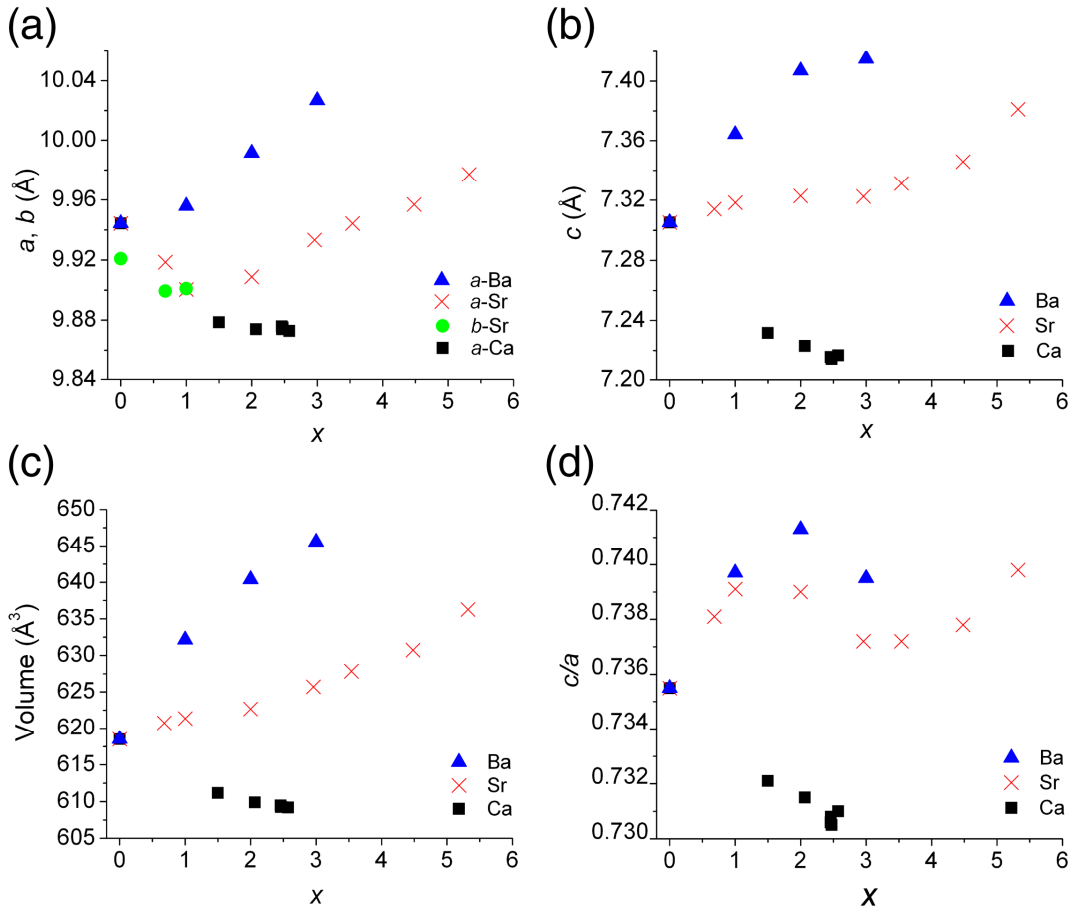

Figure 38 Unit cell trends for different alkaline earth doped lanthanum germanate pseudomorphs obtained from X-ray diffraction at room temperature. Sr and Ba show similar behavior, but Ca is distinct as it is the only AE^{2+} smaller than La^{3+}.

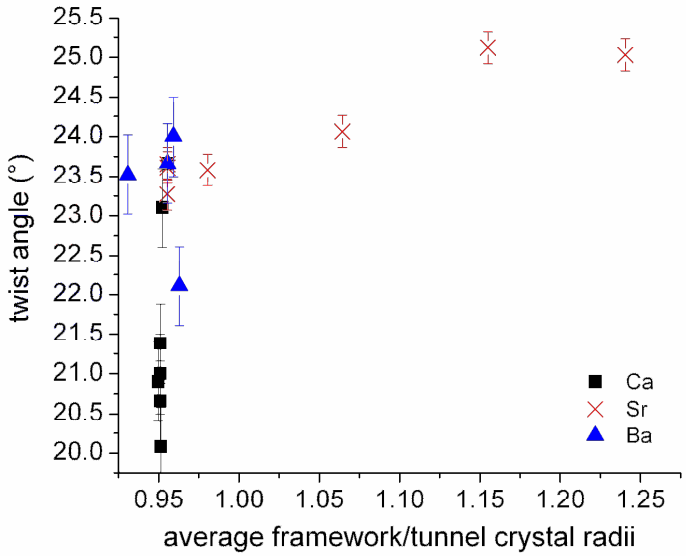

Figure 39 Twist angle trends for different *AE* dopants derived from the average ratio between framework and tunnel crystal radii.

4.3.4 Ionic Conductivity

Oxygen excess $La_{10}(GeO_4)_5(GeO_5)O_2$ apatite has a higher ionic conductivity compared to fully stoichiometric (on both cation and anion sites) $La_8AE_2(GeO_4)_6O_2$ (Table 23). At lower temperatures (T < 720°C) $La_{8.5}Ca_{1.5}(GeO_4)_{5.75}(GeO_5)_{0.25}O_2$ and co-existing $La_{9.20}Ge_6O_{26}H_\delta$ shows greatest oxygen mobility, but this situation is reversed at higher temperature (Figure 40). Discontinuities at 460 and 620 ºC for $La_{8.5}Ca_{1.5}(GeO_4)_{5.75}(GeO_5)_{0.25}O_2$ and $La_9Ba(GeO_4)_{5.5}(GeO_5)_{0.5}O_2$ are believed to coincide with the triclinic 2*A* – hexagonal 2*H* polymorphic transformation; however this should be verified by *in-situ* high temperature and high resolution powder diffraction. Nor should possibility of an intervening monoclinic phase be discounted. $La_9Ba(GeO_4)_{5.5}(GeO_5)_{0.5}O_2$ and $La_9Sr(GeO_4)_{5.5}(GeO_5)_{0.5}O_2$ show similar trends and intermediate conductivity. For stoichiometric $La_8AE_2(GeO_4)_6O_2$, where there is no interstitial oxygen, the lower oxygen mobility is observed as expected, and within these poorly performing compounds conductivity decreased in the order Sr < Ba < Ca. $La_6Sr_4(GeO_4)_6O_2H_\delta$ is hexagonal and is the poorest ion conductor (1.7×10^{-6} Scm^{-1} at 800 ºC) with very high activation energy, consistent with the lack of interstitial oxide ion defects, which are required to promote conductivity in these apatite systems.

Although the conductivity of $La_8AE_2(GeO_4)_6O_2$ is inadequate for SOFC applications, the activation energy (E_a) for ionic migration is low compared to oxygen excess samples in accord with previous studies.[175,176] The low activation energy correlates with the hexagonal symmetry of these systems, with overall conductivity limited by the paucity of interstitial oxide ions. This observation of a low activation energy is contrary to Si-analogues,[15] but consistent with modeling studies indicating lower Frenkel defect energies for the germanate systems, that is coupled with a more expansive framework and a range of possible conduction pathways.[144] Contrarily, $La_{10}Ge_6O_{27}$ with high ionic conductivity at high temperature invariably shows high activation energy, as a consequence of additional defect trapping in the lower symmetry triclinic cell. As both activation energy and extrastoichiometric oxygen control the conductivity, the performance of $La_9AEGe_6O_{26.5}$ compounds decreases from *AE* = Ca to Sr to Ba at 500°C, in a behavior opposite to Si-analogues where Ba

doping produced superior conductivity,[177] due to the dilation of the framework relative to the tunnel.

Table 23 Conductivities of Ca, Sr and Ba doped lanthanum germanate apatites do not increase linearly with temperature due to phase transitions from lower (low T) to higher symmetry (high T). $La_8Ca_2Ge_6O_{26}$ is exceptional in showing no polymorphic modifications.

Nominal composition	σ (S cm^{-1}) (800°C)	*E*a (eV) (low/medium/high T (°C))
$La_{10}Ge_6O_{27}$	0.030	1.30/2.20/1.10 (T<620 / 620<T<780 / T>780)
$La_9CaGe_6O_{26.5}$	0.010	1.09/0.70 (T<460 / T>460)
$La_9SrGe_6O_{26.5}$	0.007	1.13/0.43/0.71 (T<580 / 580<T<660 / T>660)
$La_9BaGe_6O_{26.5}$	0.013	1.13/1.01 (T<470 / T>470)
$La_8Ca_2Ge_6O_{26}$	$7.7x10^{-4}$	0.89
$La_8Sr_2Ge_6O_{26}$	$3.0x10^{-5}$	0.69/0.88 (T<490 / T>490)
$La_8Ba_2Ge_6O_{26}$	$1.1x10^{-4}$	1.01/0.80 (T<420 / T>420)
$La_7Sr_3Ge_6O_{26}H_\delta$	$7.8x10^{-6}$	0.88 / 1.35 (T<590 / T > 590)
$La_6Sr_4Ge_6O_{26}H_\delta$	$1.7x10^{-6}$	1.72

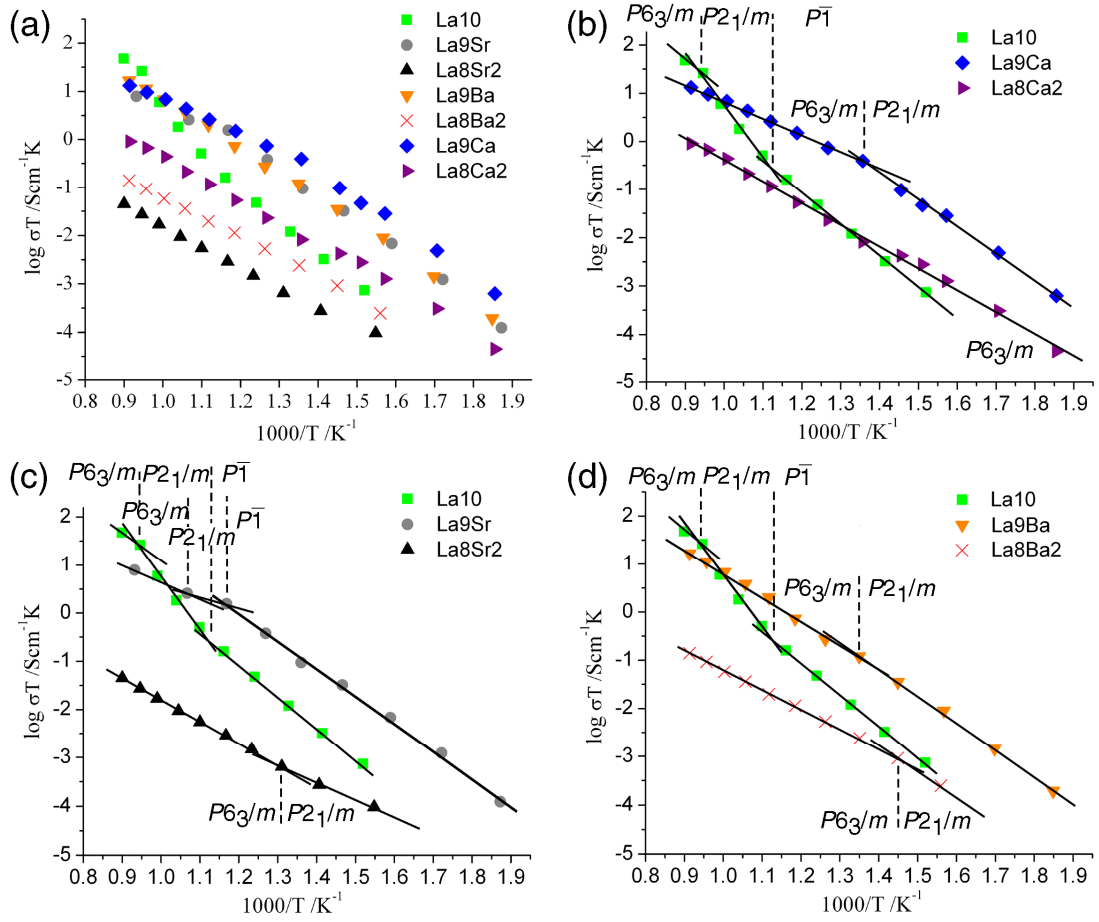

Figure 40 (a) Oxide ion conductivity for stoichiometric $La_8AE_2(GeO_4)_6O_2$ and oxygen excess $La_{10-x}AE_x(GeO_4)_{5+x/2}(GeO_5)_{1-x/2}O_2$ (x = 0 and 1) (AE = (b) Ca, (c) Sr, (d) Ba). The greatest oxygen mobility over the widest temperature range was for the x = 1 sample ($La_{8.5}Ca_{1.5}(GeO_4)_{5.75}(GeO_5)_{0.25}O_2$ with $La_{9.20}Ge_6O_{26}H_\delta$) because a lowered activation energy is optimally coupled with the interstitial oxide ion content. Inflection points correspond to the polymorphic transformations apatite – 2*A* → apatite – 2*M* → apatite – 2*H*. The higher symmetry favors conduction.

4.3.5 Atomistic Modeling

Minimum energy configurations of the stoichiometric and oxidized alkaline earth doped lanthanum germanate apatites were calculated using the short range interatomic potentials given in Table 24. Starting with the lattice energy of $La_{9.33}Ge_6O_{26}$ obtained by Berastegui *et al.*,[12] calculated and optimized atomic parameters were transformed to $P1$ so that partially occupied oxygen interstitial sites in $P6_3/m$ could be introduced as fully occupied sites in $P1$ (Table 25). The experimental and calculated unit cell and atomic parameters of $La_8AE_2(GeO_4)_6O_2$ (AE = Ca, Sr, Ba) are in good agreement (Tables 26 and 27).

The calculated anion (O^{2-}) vacancy defect energies show that within the tunnel, it is energetically preferable to have an O4 vacancy rather than disrupt the GeO_4 tetrahedra which are known to be stable structural units. Within the framework the vacancy energy of O3 is less than O1 and O2, and this may facilitate inter-tunnel oxygen transport as proposed in $La_{10}(GeO_4)_5(GeO_5)O_2$[130] and silicate systems[29]. The formation of Schottky defects is energetically unfavorable (Table 28).

The defect energy here refers to the energy of the whole system, not only at the isolated defect; and is defined as the difference between energy of the imperfect (perfect plus defect) and the perfect system. For interstitial defects, the number of ions in the system increases and ions are closer together. This, in turn will further increase the lattice energy (lattice energy becomes more negative) and vice versa for vacancy defects. It can be explained using Born Mayer equation:

$$E = \frac{LMz^+z^-e^2}{4\pi\varepsilon_0 r}\left(\frac{1-\rho}{r}\right) \quad \textbf{(27)}$$

where E is the lattice energy, L is the Avogadro constant, M is the Madelung constant, z^+ is the number of charges of each positive ion, z^- is the number of charges on each negative ion, e is the charge of the electron, r is the distance between the centers of the ions, ρ is a repulsion constant between the electron shells of adjacent ions and ε_0 is a permittivity of free space constant.[178] In order to identify whether a defect will form, we have to consider the overall process expressed in Kröger-Vink notation, which is

often called the solution energy. So for example, to create an interstitial defect in a stoichiometric system, vacancy defect needs to be created as well, known as Frenkel defect, hence the overall energy will be the sum of the two.

Table 24 Short range interatomic potentials and shell model for $La_8AE_2Ge_6O_{26}$ with the potential cut off = 12 Å.

Interaction	A (eV)	ρ (Å)	C (eV Å^6)	Y (e)	K(eV Å^{-2})
La^{3+} core – O^{2-} shell	4579.23	0.3044	0	3.00	
Ca^{2+} core – O^{2-} shell	1228.90	0.3372	0	2.00	
Sr^{2+} core – O^{2-}shell	1400.00	0.3500	0	2.00	
Ba^{2+} core – O^{2-} shell	931.70	0.3946	0	2.00	
Ge^{4+} core – O^{2-} shell	1497.40	0.3256	16.00	4.00	
O^{2-} shell – O^{2-} shell	22764.00	0.1490	27.88	-2.90	74.92

Table 25 Experimental and calculated unit cell and atomic parameters of $La_{9.33}(GeO_4)_6O_2$.

		Experimental[12]	Calculated
Volume		619.66(2)	617.778
a (Å)		9.9117(1)	9.99623
b (Å)		9.9117(1)	9.99623
c (Å)		7.2833(2)	7.13887
α (°)		90	90
β (°)		90	90
γ (°)		120	120
	x	0.333333	0.33333
La1	y	0.666667	0.66667
	z	0.0010(4)	0.00335
	x	0.2305(2)	0.23520
La2	y	0.9893(2)	0.99716
	z	0.25	0.25
	x	0.4011(2)	0.39964
Ge	y	0.3731(2)	0.37685
	z	0.25	0.25
	x	0.3160(4)	0.30829
O1	y	0.4893(4)	0.48405
	z	0.25	0.25
	x	0.6022(3)	0.60092
O2	y	0.4764(3)	0.47688
	z	0.25	0.25
	x	0.3438(3)	0.34258
O3	y	0.2502(3)	0.25169
	z	0.0610(2)	0.05960
	x	0	0
O4	y	0	0
	z	0.25	0.25
Lattice energy (eV)		-1310.12	-1327.41

The location of extrastoichiometric oxygen in these apatites has attracted some controversy, particularly for the silicate systems.[3] For the germanates, the consensus from simulation and experiment is that interstitial oxide ions neighbor Ge. In $La_{10}(GeO_4)_5(GeO_5)O_2$, the interstitial oxygen was determined by powder neutron diffraction at (0.028(4), 0.477(4), 0.511(5)), and its inclusion was accompanied by displacement, but not distortion of the two surrounding GeO_4 tetrahedra with the largest site splitting (0.87 Å) observed for O3 [(0.068(4), 0.300(4), 0.577(5)) and (0.017(3), 0.204(4), 0.615(4))],[130] as discussed in Section 4.1. These split sites are close (~0.5 Å) to the interstitial oxygen located by neutron diffraction in $La_{9.60}Ge_6O_{26.4}$ at [0.016(2), 0.228(2), 0.606(1)].[89]

It is also encouraging that in $La_8AE_2(GeO_4)_6O_2$, atomistic simulation led to almost identical relaxed defect structures when the interstitial oxygen was inserted at two starting positions (0, 1/2, 1/2) and (0.016, 0.228, 0.606), i.e. between two GeO_4 tetrahedra and at the surface of tunnel wall, respectively. Beginning at (0, 1/2, 1/2) relaxation resulted in a ~3.7 eV lower defect energy than for (0, 0, 1/2) and the O3 position (0.089, 0.340, 0.559) split into statistically disordered sites (0.050, 0.278, 0.587) and (0.084, 0.335, 0.565) separated by ~0.5 Å (Figures 41a and c). These positions are only ~0.4 Å away from the interstitial oxygen located by neutron diffraction in $La_{9.60}Ge_6O_{26.4}$ at [0.016(2), 0.228(2), 0.606(1)].[89] The location is also similar to $La_8Sr_2Si_6O_{26}$ (0.0128, 0.2315, 0.6159) determined by earlier calculations.[29,179] When extrastoichiometric oxygen was introduced at the channel periphery (0.016, 0.228, 0.606) modeling resulted in a large relaxation of O3 to (0.037, 0.487, 0.469) with position and energy comparable to those obtained by starting at (0, 1/2, 1/2) (Table 29, Figures 41b and d). It is believed that the short bond distance previously explained by local relaxation and unusually large atomic displacement parameters[90] are better described by the disordered arrangement of O3. The structural distortion caused by the formation of Ge_2O_9 dimers and O3 split sites possibly assists inter-tunnel interstitial oxygen migration and may promote the $2A \rightarrow 2M \rightarrow 2H$ pseudomorphic transformation. The agreement of these results suggests that modeling methods can be used to predict the probable locations of oxygen interstitials.

The relative solution energies for incorporating *AE* (Ca, Sr, Ba) into neutral apatite as $La^{I}_{2}AE^{I}_{2}La^{II}_{6}(GeO_4)_6O_2$ implies that the introduction of La into the La/AE^{I} framework positions is simultaneous with the capture of interstitial oxygen by the framework expressed in Kröger-Vink notation as:

$$AE^{x}_{La/AE} + \frac{1}{2}La_2O_3 \rightarrow La^{\bullet}_{La/AE} + AEO + \frac{1}{2}O_i^{''} \quad \textbf{(28)}$$

and is energetically preferable to *AE* doping in the same site and creation of an oxygen vacancy (Table 30):

$$La^{x}_{La/AE} + AEO \rightarrow AE^{'}_{La/AE} + \frac{1}{2}La_2O_3 + \frac{1}{2}V_O^{\bullet\bullet} \quad \textbf{(29)}$$

The negative solution energy for La^{3+} and O^{2-} interstitial insertion observed for Ca-doped apatite (Table 30) is due to a more stable interstitial oxygen position at (0.000, 0.498, 0.500) with the defect energy difference of 0.38 and 0.87 eV for Sa and Ba-doped, respectively. It was supported by the lowest strain in the lattice for La-Ca system because the ionic radius of La differs by 3.6% from Ca compared with Sr (10.0%) and Ba (25.5%). Furthermore the electronegativity of Ca (1.00) is more similar to La (1.10) than Sr (0.95) and Ba (0.89).[180-182] It is therefore predicted that in parent $La_8Ca_2Ge_6O_{26}$, the interstitial oxygen coupled with La^{3+} dopant is the most highly favored as compared to oxygen vacancy with Ca^{2+} dopant. This result supports the experimental observation where the Ca solid solution limit in La-germanate apatite is the narrowest among *AE* dopants.

Table 26 Experimental ($P6_3/m$) and calculated (pseudo-hexagonal $P1$) unit cell parameters of $La_8AE_2(GeO_4)_6O_2$ show good agreement.

AE		Experimental	Calculated	Δ (%)
Ca	Volume	609.87(2)	614.05	0.68
	a (Å)	9.8740(2)	9.9988	1.26
	b (Å)	9.8740(2)	9.9988	1.26
	c (Å)	7.2231(2)	7.0921	-1.81
	α (°)	90	90.0	0
	β (°)	90	90.0	0
	γ (°)	120	120.0	0
	Lattice energy (eV)	-1311.46	-1328.36	
Sr	Volume	622.65(2)	624.89	0.36
	a (Å)	9.9087(1)	10.0275	1.20
	b (Å)	9.9087(1)	10.0275	1.20
	c (Å)	7.3229(1)	7.1761	-2.00
	α (°)	90	90.0	0
	β (°)	90	90.0	0
	γ (°)	120	120.0	0
	Lattice energy (eV)	-1305.88	-1323.96	
Ba	Volume	640.38(3)	639.86	-0.08
	a (Å)	9.9916(2)	10.0906	0.99
	b (Å)	9.9916(2)	10.0906	0.99
	c (Å)	7.4069(2)	7.2564	-2.03
	α (°)	90	90.0	0
	β (°)	90	90.0	0
	γ (°)	120	120.0	0
	Lattice energy (eV)	-1297.54	-1317.31	

Table 27 Calculated atomic parameters of $La_{9.33}(GeO_4)_6O_2$ and $La_8AE_2(GeO_4)_6O_2$.

		$La_{9.33}(GeO_4)_6O_2$	Ca	Sr	Ba
La/*AE*1	*x*	0.33333	0.33277	0.33402	0.33525
	y	0.66667	0.66479	0.66687	0.66745
	z	0.00335	0.00443	0.00347	0.00337
La/*AE*2	*x*	0.66667	0.66610	0.66735	0.66859
	y	0.33333	0.33145	0.33353	0.33412
	z	0.50335	0.50443	0.50347	0.50337
La/*AE*3	*x*	0.66667	0.66610	0.66735	0.66859
	y	0.33333	0.33145	0.33353	0.33412
	z	0.99665	0.99557	0.99653	0.99664
La/*AE*4	*x*	0.33333	0.33277	0.33402	0.33525
	y	0.66667	0.66479	0.66687	0.66745
	z	0.49665	0.49557	0.49653	0.49664
La5	*x*	0.2352	0.2352	0.2352	0.2352
	y	0.99716	0.99716	0.99716	0.99716
	z	0.25	0.25	0.25	0.25
La6	*x*	0.7648	0.76366	0.76617	0.76864
	y	0.00284	0.99908	0.00324	0.00442
	z	0.75	0.75	0.75	0.75

	x	0.00284	0.00039	0.00373	0.00555
La7	y	0.23804	0.23485	0.23776	0.23770
	z	0.25	0.25	0.25	0.25
	x	0.76196	0.76270	0.76313	0.76501
La8	y	0.7648	0.76235	0.76569	0.76751
	z	0.25	0.25	0.25	0.25
	x	0.23804	0.23616	0.23824	0.23883
La9	y	0.2352	0.23389	0.23471	0.23407
	z	0.75	0.75	0.75	0.75
	x	0.99716	0.99847	0.99765	0.99829
La10	y	0.76196	0.76139	0.76265	0.76388
	z	0.75	0.75	0.75	0.75
	x	0.39964	0.40077	0.39801	0.39503
Ge1	y	0.37685	0.37662	0.37593	0.37405
	z	0.25	0.25	0.25	0.25
	x	0.60036	0.59810	0.60337	0.60881
Ge2	y	0.62315	0.61962	0.62448	0.62753
	z	0.75	0.75	0.75	0.75
	x	0.62315	0.62093	0.62496	0.62866
Ge3	y	0.02279	0.02096	0.02180	0.02064
	z	0.25	0.25	0.25	0.25
	x	0.97721	0.97660	0.97909	0.98207
Ge4	y	0.60036	0.59678	0.60288	0.60768
	z	0.25	0.25	0.25	0.25
	x	0.02279	0.02227	0.02229	0.02177
Ge5	y	0.39964	0.39946	0.39752	0.39390
	z	0.75	0.75	0.75	0.75
	x	0.37685	0.37793	0.37641	0.37518
Ge6	y	0.97721	0.97528	0.97860	0.98094
	z	0.75	0.75	0.75	0.75
O1	x	0.30829	0.31333	0.30471	0.29802
	y	0.48405	0.48734	0.48090	0.47446
	z	0.25	0.25	0.25	0.25
O2	x	0.69171	0.68553	0.69667	0.70582
	y	0.51595	0.50890	0.51950	0.52712
	z	0.75	0.75	0.75	0.75
O3	x	0.51595	0.51021	0.51999	0.52825
	y	0.82424	0.82280	0.82352	0.82322
	z	0.25	0.25	0.25	0.25
O4	x	0.17576	0.1748	0.17737	0.17949
	y	0.69171	0.68422	0.69618	0.70469
	z	0.25	0.25	0.25	0.25
O5	x	0.82424	0.82411	0.82401	0.82435
	y	0.30829	0.31202	0.30422	0.296889
	z	0.75	0.75	0.75	0.75
O6	x	0.48405	0.48865	0.48139	0.47559
	y	0.17576	0.17344	0.17688	0.17836
	z	0.75	0.75	0.75	0.75
O7	x	0.60092	0.60212	0.59883	0.59463
	y	0.47688	0.47343	0.47804	0.48065
	z	0.25	0.25	0.25	0.25
O8	x	0.39908	0.39674	0.40255	0.40921
	y	0.52312	0.52281	0.52237	0.52093
	z	0.75	0.75	0.75	0.75
O9	x	0.52312	0.52412	0.52285	0.52206
	y	0.12404	0.12550	0.12051	0.11364

	z	0.25	0.25	0.25	0.25
O10	*x*	0.87596	0.87205	0.88038	0.88907
	y	0.39908	0.39543	0.40206	0.40808
	z	0.25	0.25	0.25	0.25
O11	*x*	0.12404	0.12681	0.12099	0.11477
	y	0.60092	0.60081	0.59834	0.59350
	z	0.75	0.75	0.75	0.75
O12	*x*	0.47688	0.47474	0.47852	0.48178
	y	0.87596	0.87074	0.87990	0.88794
	z	0.75	0.75	0.75	0.75
O13	*x*	0.34258	0.34125	0.34152	0.34021
	y	0.25169	0.25071	0.25101	0.24984
	z	0.0596	0.05891	0.06060	0.06267
O14	*x*	0.65742	0.65762	0.65986	0.66363
	y	0.74831	0.74553	0.74939	0.75173
	z	0.5596	0.55891	0.56060	0.56267
O15	*x*	0.74831	0.74684	0.74988	0.75286
	y	0.09089	0.08734	0.09022	0.09002
	z	0.0596	0.05891	0.06060	0.06267
O16	*x*	0.90911	0.91021	0.91066	0.91268
	y	0.65742	0.65630	0.65937	0.66250
	z	0.0596	0.05891	0.06060	0.06267
O17	*x*	0.09089	0.08865	0.09071	0.09116
	y	0.34258	0.33994	0.34103	0.33908
	z	0.5596	0.55891	0.56060	0.56267
O18	*x*	0.25169	0.25203	0.25150	0.25097
	y	0.90911	0.90890	0.91018	0.91155
	z	0.5596	0.55891	0.56060	0.56267
O19	*x*	0.65742	0.65762	0.65986	0.66363
	y	0.74831	0.74553	0.74939	0.75173
	z	0.9404	0.94109	0.93940	0.93733
O20	*x*	0.34258	0.34125	0.34152	0.34021
	y	0.25169	0.25071	0.25101	0.24984
	z	0.4404	0.44109	0.43940	0.43733
O21	*x*	0.25169	0.25203	0.25150	0.25097
	y	0.90911	0.90890	0.91018	0.91155
	z	0.9404	0.94109	0.93940	0.93733
O22	*x*	0.09089	0.08865	0.09071	0.09116
	y	0.34258	0.33994	0.34103	0.33908
	z	0.9404	0.94109	0.93940	0.93733
O23	*x*	0.90911	0.91021	0.91066	0.91268
	y	0.65742	0.65630	0.65937	0.66250
	z	0.4404	0.44109	0.43940	0.43733
O24	*x*	0.74831	0.74684	0.74988	0.75286
	y	0.09089	0.08734	0.09022	0.09002
	z	0.4404	0.44109	0.43940	0.43733
O25	*x*	0	0.99943	0.00069	0.00192
	y	0	0.99812	0.00020	0.00079
	z	0.25	0.25	0.25	0.25
O26	*x*	0	0.99943	0.00069	0.00192
	y	0	0.99812	0.00020	0.00079
	z	0.75	0.75	0.75	0.75

Table 28 Vacancy, Schottky defect and substitution energies of $La_8AE_2(GeO_4)_6O_2$. The formation of an O4 vacancy is energetically most preferable.

Vacancy defect energy (eV/defect)	Ca	Sr	Ba
La1/*AE*1	32.68	31.72	30.11
La1	44.16	44.26	44.25
*AE*1	22.84	21.08	18.43
La2	45.58	47.15	46.96
Ge	99.09	98.55	100.37
O1	21.77	22.13	22.35
O2	23.18	20.47	22.91
O3	20.19	20.09	19.84
O4	18.85	18.85	18.65

Schottky defect energy (eV/defect)			
La_2O_3	3.04	3.09	2.96
GeO_2	5.06	4.88	5.35
*AE*O	2.82	3.08	2.86
$La_8AE_2Ge_6O_{26}$	3.70	3.66	3.82

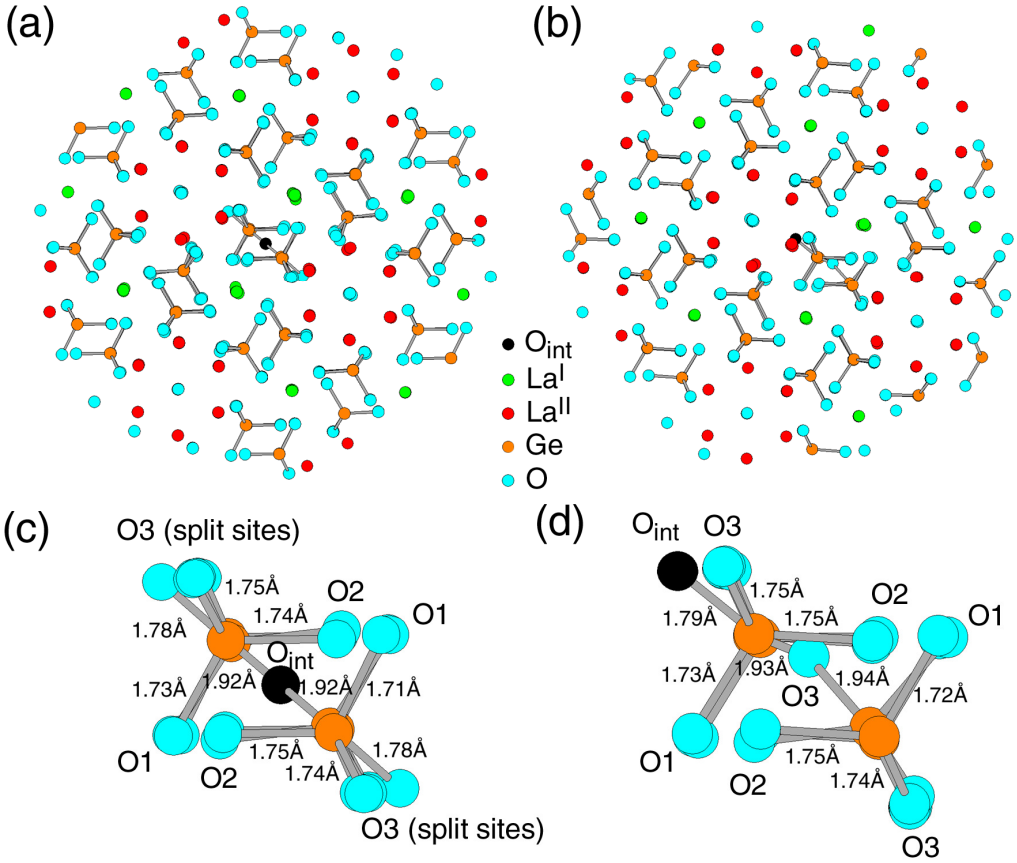

Figure 41 Relaxed apatite defect cores projected along [001]. The interstitial oxygen (black) is placed at (a) (0.002, 0.501, 0.500) and (b) (0.046, 0.262, 0.593) with the Ge_2O_9 unit emphasized in (c) and (d), respectively. Energetically, the relaxed structures of these two 'distinct' extrastoichiometric oxygen positions are similar.

Table 29 Computed defect energies and interstitial positions for extrastoichiometric oxygen in $La_8AE_2(GeO_4)_6O_2$. Relaxed position 2 leads to the splitting of O3 to (0.050, 0.278, 0.587) and (0.084, 0.335, 0.565) which is close to the interstitial position 3. In the same manner, relaxed position 3 leads to the displacement of O3 to (0.037, 0.487, 0.469) near to the interstitial position 2. Hence, they possess the same energetically relaxed structure (see Figure 41).

AE	modeling position	initial fractional coordinate	final fractional coordinate	defect energy (eV)
Ca	1	(0, 0, 1/2)	(0.000, -0.002, 0.551)	-11.49
	2	(0, 1/2, 1/2)	(0.000, 0.498, 0.500)	-15.06
	3	(0.016, 0.228, 0.606)[89]	(-0.057, 0.228, 0.647)	-13.67
Sr	1	(0, 0, 1/2)	(0.001, 0.000, 0.500)	-10.86
	2	(0, 1/2, 1/2)	(0.001, 0.500, 0.500)	-14.57
	3	(0.016, 0.228, 0.606)[89]	(0.039, 0.257, 0.598)	-14.68
Ba	1	(0, 0, 1/2)	(0.002, 0.001, 0.500)	-10.32
	2	(0, 1/2, 1/2)	(0.002, 0.501, 0.500)	-14.13
	3	(0.016, 0.228, 0.606)[89]	(0.046, 0.262, 0.593)	-14.19

Table 30 Calculated solution energies (eV/dopant) for La and *AE* in A^I framework site in $La_8AE_2Ge_6O_{26}$. In each case, the insertion mechanism of La^{3+} coupled with an O^{2-} interstitial is more favorable than introduction of AE^{2+} and a vacancy.

Parent composition	La^{3+} and O^{2-} interstitial insertion	AE^{2+} and vacancy insertion
$La_8Ca_2Ge_6O_{26}$	-0.06	1.96
$La_8Sr_2Ge_6O_{26}$	0.52	1.57
$La_8Ba_2Ge_6O_{26}$	0.56	1.66

4.3.6 Conclusion: Correlating Co-operative Displacements with Conductivity

Alkaline earth doped lanthanum germanate apatites show distinct pseudomorphic transformation compositions in passing from $P\bar{1}$ ($x < 1.5$ and $x < 1$) to $P6_3/m$ ($x > 1.5$ and $x > 2$) for $La_{10-x}Ca_xGe_6O_{27-x/2}$ and $La_{10-x}Ba_xGe_6O_{27-x/2}$, respectively. An intervening apatite – 2*M* pseudomorph may also be present. Ca is least soluble in $La_{10-x}AE_xGe_6O_{27-x/2}$ compared to Sr and Ba. Oxygen excess apatites deliver the highest conductivity at low temperature. In addition, the symmetry change at high temperature to hexagonal apatite – 2*H* lowers the activation energy for ion migration. Atomistic modeling suggests the energetically favored interstitial position is located near (0, 1/2, 1/2) with its introduction accompanied by splitting of the O3 position (0.089, 0.340, 0.559) into statistically disordered sites (0.050, 0.278, 0.587) and (0.084, 0.335, 0.565) in agreement with experiment. These insights into the structural transformations that accompany extrastoichiometric oxygen loading in the framework can facilitate the design of intermediate temperature solid oxide fuel cell apatite electrolytes.

4.4 Sodium Substituted Lanthanum Silicate Apatite – 2*H* Electrolytes and the Non-Existence of $La_{10}Si_6O_{27}$

4.4.1 Na^+ Doping of "$La_{10}Si_6O_{27}$"Apatite

It was shown in Section 4.1 that the compound $La_{10}Ge_6O_{27}$ is crystallochemically described as $La_{10}[(GeO_4)_5(GeO_5)]O_2$, however the analogue $La_{10}Si_6O_{27}$ may not exist, despite numerous publications with respect to its synthesis and properties.[2,9,10,183] The difficulty arises because Si^{4+}, unlike Ge^{4+}, can readily accommodate only four O^{2-} in first near-neighbor tetrahedral bonding – indeed the SiO_4 polyhedra is one of the most rigid known.[184] Where higher coordination does appear, it is combined with unusual edge-sharing tetrahedra as in leucophoenicite[185] or is stabilized by high pressure, as in stishovite.[186,187] Thus, in apatite electrolytes fabricated at ambient pressure,[188] it is unlikely that extrastoichiometric oxygen is substantially contained in the framework to create SiO_5 trigonal bipyramids. For cation-deficient rare-earth silicate apatites, the parent structure is often represented as "$La_{9.33}\square_{0.67}(SiO_4)_6O_2$,"[139] but this description does not account for ^{29}Si NMR data that reveals several resonances[105] and a more complete polysomatic representation may be as apatite – 6*H* $La_{10}\square_2La_{18}(SiO_4)_6(Si_2O_7)_3(Si_2O_9)_3O_2$ where the La-vacancy is surrounded by Si_2O_7 dimers to create a cage structure (Figure 42). When $La_{9.33}\square_{0.67}Si_6O_{26}$ is modified through the introduction of *A*-type counter ions over the crystallographically unique La^I and La^{II} sites, electrolyte properties will be controlled by the apportionment of the dopant and its concentration. The introduction of alkaline earths to lanthanum silicate electrolytes has been widely considered, but doping with alkali metals has been scarcely reported, possibly because of substantial volatilization during synthesis.[159,189-191] Oxide ion conductivity has been reported for $RE_{8.67}Na_{1.33}(SiO_4)_6(F_{0.33}O_{0.67})_2$ (*RE* = La, Ce, Gd) where poor mobility may be a consequence of fluorine behaving as a migration barrier.[16]

As larger ions can occupy the A^I (6-coordinated) and/or A^{II} (7-coordinated) cation acceptor sites, ionic size and electrostatic charge will determine the partitioning. Na^+

in six-coordination is slightly smaller than La^{3+} (ionic radii of Na^{+} = 1.02 Å and La^{3+} = 1.032 Å), while the situation is reversed in seven-coordination (Na^{+} = 1.12 Å and La^{3+} = 1.10 Å),[43] suggesting that the replacement of La by Na may show a dependence on dopant concentration. Following usual precepts, it is anticipated that at low concentrations, sodium simultaneously replaces lanthanum and fills *A*-site vacancies (□) in $La_{9.33}\square_{0.67}Si_6O_{26}$ such that

$$La^{3+} + 2\square_{La} \rightarrow 3Na^{+} \quad \textbf{(30)}$$

to generate the series $La_{9.33-x/3}Na_xSi_6O_{26}$ ($0 \leq x \leq 1$) where the sodium-rich end-member has the composition $La_9Na(SiO_4)_6O_2$.

For higher Na loadings, different mechanisms come into play that either remove tunnel oxygen:

$$La^{3+} + O^{2-} \rightarrow Na^{+} + \square_{O} \quad \textbf{(31)}$$

or, more likely, introduce hydrogen as hydroxyl (OH^{-}) groups:

$$La^{3+} + 2O^{2-} \rightarrow Na^{+} + 2OH^{-} \quad \textbf{(32)}$$

that may be expressed as $La_{9-y}Na_{1+y}(SiO_4)_6O_{2-2y}(OH)_{2y}$ with $0 \leq y \leq 1$. This series is analogous to $La_{10-x}Sr_xGe_6O_{27-x/2}H_\delta$ as described in Section 4.2. While substitution (30) is not believed to be operative when syntheses are carried out in air,[64] the hydroxylation mechanism (31) is probable.

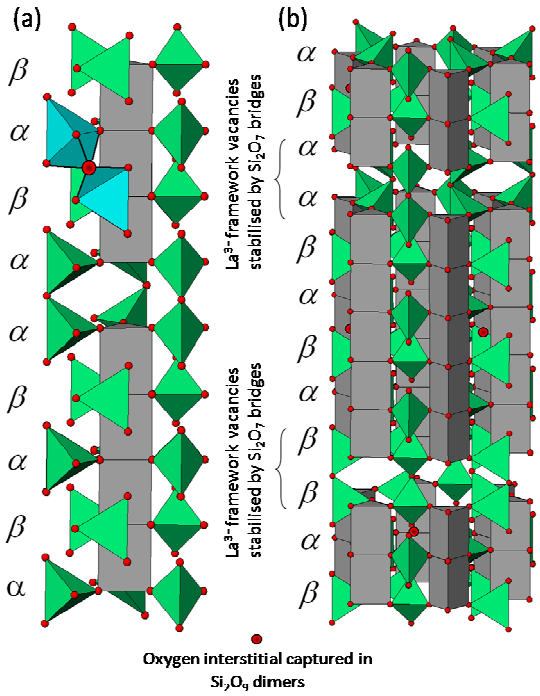

Figure 42 Apatite – 6*H* $La_{10}\square_2La_{18}(SiO_4)_6(Si_2O_7)_3(Si_2O_9)_3O_2$ with the La^I framework vacancies stabilized by Si_2O_7 bridges. Only La^IO_6 metaprisms (grey) and SiO_4 tetrahedra (green) and Si_2O_9 trigonal bipyramids (blue) are shown for clarity. [Taken from Baikie *et al.*[102]]

In general, sodium is a weak scatterer of X-rays, at least compared to lanthanum, and conventional laboratory experiments are not ideal for investigating Na incorporation in the electrolyte. Therefore, the present study exploited anomalous scattering to accentuate differences in X-ray form factors near the La L_{III} absorption edge to more reliably establish cation concentration and location.

As the primary objective of the study was to monitor the occupancy of the A^I and A^{II} sites, resonant powder diffraction was undertaken at X-ray energies of 5.473 keV or 5.000 keV, these being 10 eV and 473 eV away from the 5.483 keV La L_{III}-edge which is the preferred absorption edge to observe strong anomalous scattering effects.[192-195] This approach leads to large changes in diffracted intensity as illustrated in Figure 43. While the relative diffracted intensities of $La_{9.33}Si_6O_{26}$, $La_9Na(SiO_4)_6O_2$, $La_{8.5}Na_{1.5}(SiO_4)_6O(OH)$ and $La_8Na_2(SiO_4)_6(OH)_2$ were not obviously different when collected using copper radiation (8.03 keV), these compounds were clearly discriminated in those data sets collected near the absorption edge. For each composition, three powder diffraction patterns – one laboratory (designated the X experiment at 8.03 keV) and two synchrotron (designated E1 (5.473 keV) and E2

(5.000 keV)) – were simultaneously refined, with all crystallographic parameters constrained to have identical values.

4.4.2 Crystallochemical Analysis

For all compositions, the refinements were carried out in $P6_3/m$ and $P\bar{3}$ as in earlier analyses,[139] but in every case the former space group was chosen as the trigonal setting gave no significant improvement in residuals. An attempt to synthesize $La_{10}Si_6O_{27}$ was unsuccessful and the refined occupancy of La resulted in $La_{9.34}Si_6O_{26}$ (Table 31) with lattice parameters similar to Sansom *et al.*.[139] A small amount (6 wt.%) of $P2_1/c$ $La_2Si_2O_7$ was observed for the composition $La_{9.16}Na_{0.6}Si_6O_{26.5}$ and $La(OH)_3$ (5 wt.%) co-existed with apatite in $La_9Na(SiO_4)_6O_2$. The presence of minor phases is consistent with other investigations of lanthanum silicate apatites.[196,197] Impurity phases were not detected in the remaining samples. The refined crystal and atomic parameters of $La_{9.33-x/3}Na_xSi_6O_{26}$ are collated in Table 32. Although attempts were made to prepare apatites with $y > 1.0$ in $La_{9-y}Na_{1+y}(SiO_4)_6O_{2-2y}(OH)_{2y}$, Rietveld analysis showed that the cell constants and refined sodium occupancies saturated at $y = 1$, and as detectable impurities were absent, it is assumed sodium was lost by volatilization to leave a glassy silicate residue.

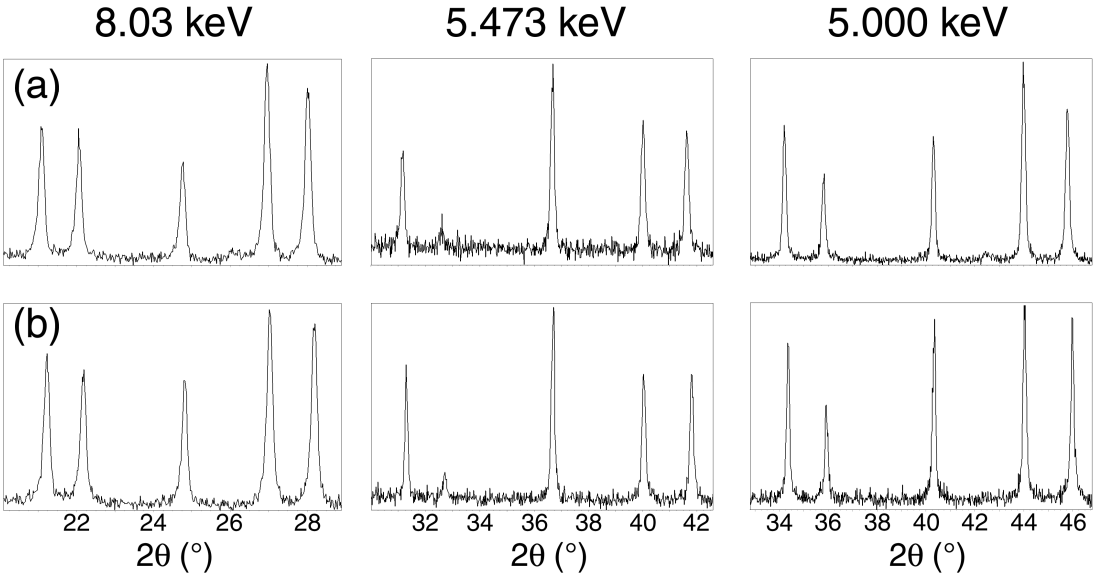

Figure 43 Changes in the relative diffracted intensities for selected reflections for (a) $La_{9.33}(SiO_4)_6O_2$ (b) $La_8Na_2(SiO_4)_6(OH)_2$ as a function of X-ray energy. Miller indices of the reflections shown - from left to right, {020}, {111}, {002}, {012} and {120}.

In every case, the O4 position was fully occupied within experimental error. This is consistent with the conversion of $O^{2-} \rightarrow OH^-$ to maintain charge balance, in an analogous manner to the $La_{8-x}Sr_{2+x}(GeO_4)_6O_{2-x}(OH)_x$ series described in Section 4.2. However, as X-rays are insensitive to hydrogen ions this could not be confirmed and neutron diffraction will be required to remove ambiguity on this point. For $La_{9-y}Na_{1+y}(SiO_4)_6O_{2-2y}(OH)_{2y}$ ($0 \leq y \leq 1$), the O4 tunnel ions were split over the 4*e* Wyckoff site (0 0 *z*), rather than fully tenanting at the 2*a* (0 0 ¼), consistent with poor intra-channel correlation (Table 33).

4.4.3 Trends in Lattice Parameters

The trends in lattice parameters for the $La_{9.33-x/3}Na_x(SiO_4)_6O_2$ and $La_{9-y}Na_{1+y}(SiO_4)_6O_{2-2y}(OH)_{2y}$ series are collated in Figure 44 with a clear discontinuity indicative of the different substitution mechanisms. In the former, there is a substantial reduction in *a* in passing from $La_{9.33}Si_6O_{26}$ to $La_9NaSi_6O_{26}$ consistent with the replacement of lanthanum by sodium in the six coordination metaprism.[198] For $La_{9.33}Si_6O_{26}$ and $La_{9.16}Na_{0.6}Si_6O_{26}$ the *c* parameters are quite similar, but the *a*-edges are distinct. As X-rays are quite insensitive during diffraction for establishing the position of low *Z* oxygen in a heavy element (La) matrix, the metaprism twist angle (ϕ) cannot be determined with the accuracy required to correlate La content with the average framework to tunnel crystal radii (Figure 45).

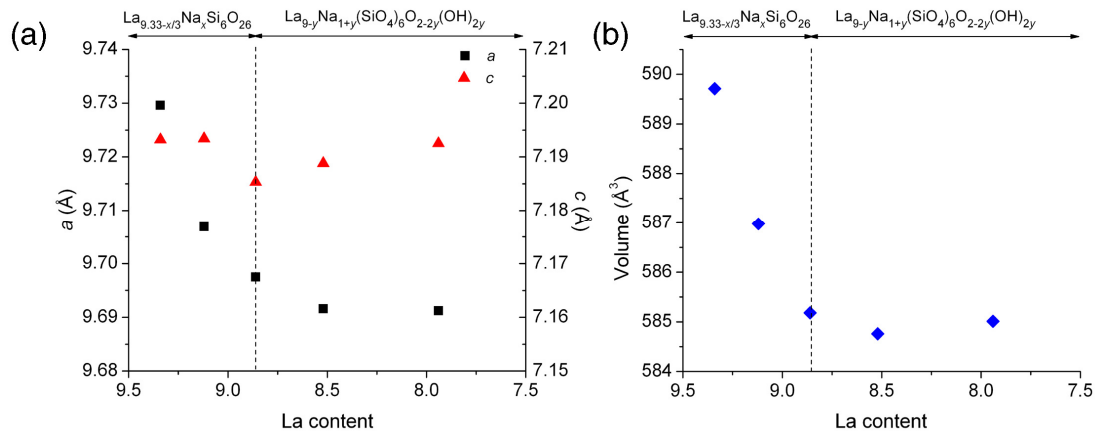

Figure 44 Variation in cell constants as a function of refined La content.

Table 31 Comparison of ideal and refined chemical formula for $La_{9.33-x/3}Na_x(SiO_4)_6O_2$ (x = 0 and 0.5) $La_{9-y}Na_{1+y}(SiO_4)_6O_{2-y}(OH)_y$ (y = 0, 0.5 and 1).

	Composition	Phase(s) present	Space group	Chemical formula (ideal)	Chemical formula (refined)
x	0	Hexagonal	$P6_3/m$	La_{10}	$La_{9.34}$
	0.5	Hexagonal &	$P6_3/m$	$La_{9.16}Na_{0.5}$	$La_{9.12}Na_{0.6}$
		$La_2Si_2O_7$	$P2_1/c$		
y	0	Hexagonal	$P6_3/m$	La_9Na_1	$La_{8.86}Na_{1.14}$
		$La(OH)_3$	$P6_3/m$		
	0.5	Hexagonal	$P6_3/m$	$La_{8.5}Na_{1.5}$	$La_{8.52}Na_{1.48}$
	1	Hexagonal	$P6_3/m$	La_8Na_2	$La_{7.94}Na_{2.06}$

Table 32 Refined crystal and atomic parameters from powder XRD of $La_{9.33-x/3}Na_x(SiO_4)_6O_2$ (x = 0 and 0.5).

Nominal x	0	0.5
Space Group	$P6_3/m$	$P6_3/m$
a (Å)	9.7296(2)	9.7069(1)
c (Å)	7.1932(1)	7.1934(1)
V (Å^3)	589.71(2)	586.98(2)
ϕ (°)	23.1(5)	24.4(5)
GOF^X/ GOF^{E1}/ $GOF^{E2\dagger}$	1.23/ 1.14/ 1.20	1.19/ 1.11/ 1.15
$R_{exp}{}^X$/ $R_{exp}{}^{E1}$/ $R_{exp}{}^{E2}$ (%)	4.40/ 9.81/ 14.89	4.42/ 12.56/ 16.10
$R_{wp}{}^X$/ $R_{wp}{}^{E1}$/ $R_{wp}{}^{E2}$ (%)	5.41/ 11.22/ 17.91	5.26/ 13.93/ 18.53
$R_p{}^X$/ $R_p{}^{E1}$/ $R_p{}^{E2}$ (%)	4.32/ 8.85/ 13.24	4.19/ 11.00/ 13.67
$R_b{}^X$/ $R_b{}^{E1}$/ $R_b{}^{E2}$ (%)	1.35/ 2.72/ 3.14	1.10/ 2.88/ 3.44
La1, 4*f*, (1/3, 2/3, z)		
z	0.9998(7)	0.9987(7)
Occ La/Na1	0.836(4)	0.78(1)/0.15(3)
B (Å^2)	1.40(9)	1.22(8)
La2, 6*h*, (x, y, 1/4)		
x	0.2307(2)	0.2315(2)
y	0.9874(3)	0.9863(3)
Occ	1	1
B (Å^2)	0.95(5)	0.56(4)
Si, 6*h*, (x, y, 1/4)		
x	0.4036(8)	0.4009(8)
y	0.3691(9)	0.3693(8)
B (Å^2)	0.7(2)	0.2(2)
O1, 6*h*, (x, y, 1/4)		
x	0.323(1)	0.323(1)
y	0.479(1)	0.481(1)
B (Å^2)	0.7(2)	0.3(2)
O2, 6*h*, (x, y, 1/4)		
x	0.592(2)	0.589(1)
y	0.471(1)	0.465(1)
B (Å^2)	0.7(2)	0.3(2)
O3, 12*i*, (x, y, z)		
x	0.342(1)	0.342(1)
y	0.257(1)	0.259(1)

z	0.077(1)	0.073(1)
B (Å^2)	0.7(2)	0.3(2)
O4, 2*a*, (0, 0, *z*)		
z	1/4	1/4
Occ	1.000(2)	1.000(2)
B (Å^2)	0.7(2)	0.3(2)

†X = Laboratory X-ray (8.03 keV), E1 = Synchrotron X-ray (5.473 keV) and E3 = Synchrotron X-ray (5.000 keV).

Table 33 Refined crystal and atomic parameters for $La_{9-y}Na_{1+y}(SiO_4)_6O_{2-2y}(OH)_{2y}$ (y = 0, 0.5 and 1).

Nominal x	0	0.5	1
Space Group	*P*6$_3$*m*	*P*6$_3$*m*	*P*6$_3$*m*
a (Å)	9.6975(1)	9.6916(1)	9.6912(2)
c (Å)	7.1853(1)	7.1888(1)	7.1925(2)
V (Å^3)	585.18(2)	584.76(2)	585.01(3)
ϕ (°)	20.3(5)	20.4(5)	23.7(5)
GOF^{X}/ GOF^{E1}/ GOF^{E2†}	1.20/ 1.19/ 1.22	1.27/ 1.31/ 1.29	1.16/ 1.16/ 1.18
R_{exp}^{X}/ R_{exp}^{E1}/ R_{exp}^{E2} (%)	4.13/ 10.11/ 12.45	4.12/ 9.53/ 13.08	4.43/ 12.38/ 22.54
R_{wp}^{X}/ R_{wp}^{E1}/ R_{wp}^{E2} (%)	4.98/ 12.05/ 15.18	5.23/ 12.49/ 16.83	5.12/ 14.41/ 26.55
R_{p}^{X}/ R_{p}^{E1}/ R_{p}^{E2} (%)	3.97/9.50/ 11.69	4.12/ 9.63/ 12.94	4.09/ 11.40/ 20.15
R_{b}^{X}/ R_{b}^{E1}/ R_{b}^{E2} (%)	1.01/ 3.56/ 4.30	2.56/ 5.63/ 6.82	1.46/ 4.90/ 6.08
La1, 4*f*, (1/3, 2/3, *z*)			
z	-0.0021(5)	0.0015(7)	-0.0023(7)
Occ La/Na1	0.76(1)/0.24(1)	0.72(1)/0.28(1)	0.65(1)/0.35(1)
B (Å^2)	0.68(7)	0.80(7)	0.69
La2, 6*h*, (*x*, *y*, 1/4)			
x	0.0138(2)	0.0145(3)	0.0150(3)
y	0.2418(2)	0.2448(2)	0.2457(2)
Occ La/Na2	0.97(1)/0.03(1)	0.94(1)/0.06(1)	0.89(1)/0.11(1)
B (Å^2)	0.39(4)	0.70(4)	0.58(5)
Si, 6*h*, (*x*, *y*, 1/4)			
x	0.4041(6)	0.4015(7)	0.4043(9)
y	0.3700(6)	0.3705(8)	0.3687(9)
B (Å^2)	0.5(2)	2.2(2)	1.8(2)
O1, 6*h*, (*x*, *y*, 1/4)			
x	0.3313(11)	0.3241(13)	0.3206(14)
y	0.4823(11)	0.4895(13)	0.4770 (15)
B (Å^2)	0.4(2)	2.5(2)	2.2(3)
O2, 6*h*, (*x*, *y*, 1/4)			
x	0.5966(11)	0.5996(13)	0.5936(17)
y	0.4674(11)	0.4810(13)	0.4684(17)
B (Å^2)	0.4(2)	2.5(2)	2.2(3)
O3, 12*i*, (*x*, *y*, *z*)			
x	0.3401(7)	0.3375(7)	0.3399(9)
y	0.2541(7)	0.2585(8)	0.2566(10)
z	0.0696(8)	0.0828(9)	0.0739(11)
B (Å^2)	0.4(2)	2.5(2)	2.2(3)
O4, 2*a*, (0, 0, *z*)			
z	0.2017(22)	0.2468(9)	0.2521(11)
Occ	0.50(3)	0.50(3)	0.50(3)
B (Å^2)	0.4(2)	2.5(2)	2.2(3)

†X = Laboratory X-ray (8.03 keV), E1 = Synchrotron X-ray (5.473 keV) and

E3 = Synchrotron X-ray (5.000 keV).

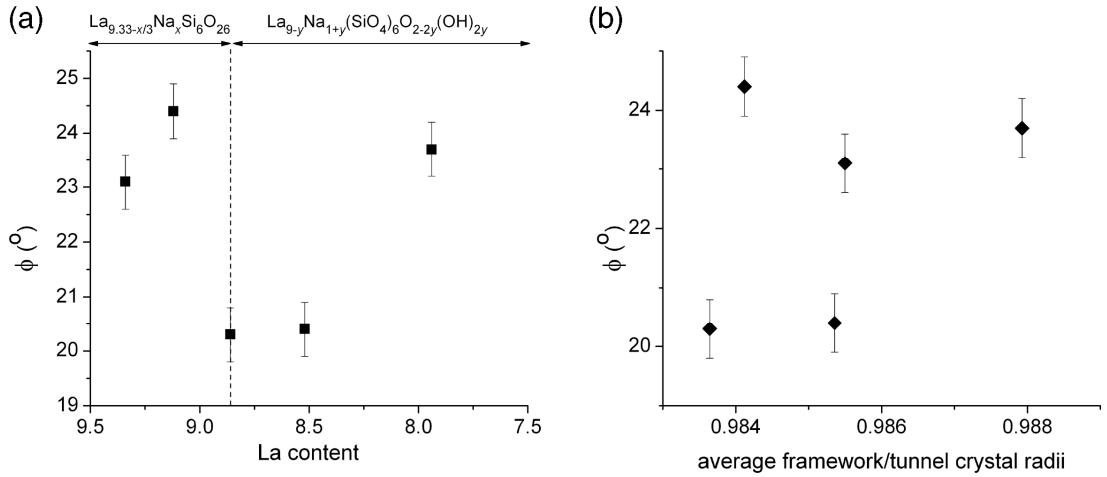

Figure 45 A clear discontinuity in twist angle is apparent when the mechanism for Na incorporation changes. There is no simple correlation between ϕ, and (a) La content or (b) average framework to tunnel crystal radii.

For the $La_{9-y}Na_{1+y}(SiO_4)_6O_{2-2y}(OH)_{2y}$ compounds changes in *a* are modest, because sodium not only enters the A^{I} site, but also the A^{II} channel positions where the cation coordination to oxygen is seven. In this case, the relative ionic radii of lanthanum and sodium are self-compensating, and together with the presumed insertion of protons which converts the oxygen ions to slightly smaller OH^-, results in minor cell constant dilation across the $La_{9-y}Na_{1+y}(SiO_4)_6O_{2-2y}(OH)_{2y}$ as sodium content increases.

The refined bond distances for $La_{9.33-x/3}Na_x(SiO_4)_6O_2$ (x = 0 and 0.5) $La_{9-y}Na_{1+y}(SiO_4)_6O_{2-2y}(OH)_{2y}$ (y = 0, 0.5 and 1) are collated inTable 34, where the analysis employed a semi-rigid SiO_4 tetrahedra to ensure all the Si-O bond distances fall within acceptable ranges. Figures 46 and 47 present the Rietveld plots of $La_{9.12}Na_{0.60}(SiO_4)_6O_2$ and $La_8Na_2(SiO_4)_6(OH)_2$ respectively.

Table 34 Selected bond distances (Å) for $La_{9.33-x/3}Na_x(SiO_4)_6O_2$ (x = 0 and 0.5) and $La_{9-y}Na_{1+y}(SiO_4)_6O_{2-2y}(OH)_{2y}$ (y = 0, 0.5 and 1) refined in $P6_3/m$.

	$x = 0$	$x = 0.5$	$y = 0$	$y = 0.5$	$y = 1$
La1-O1 [x 3]	2.563(11)	2.521(10)	2.538(9)	2.449(10)	2.541(12)
La1-O2 [x 3]	2.556(13)	2.527(12)	2.491(10)	2.583(12)	2.514(14)
La1-O3 [x 3]	2.913(8)	2.902(8)	2.902(6)	2.960(7)	2.914(9)
Average	2.677	2.650	2.646	2.664	2.656
La2-O1	2.748(11)	2.716(10)	2.782(8)	2.739(9)	2.675(11)
La2-O2	2.518(12)	2.551(11)	2.560(10)	2.424(11)	2.528(14)
La2-O3 [x 2]	2.501(7)	2.474(7)	2.450(6)	2.522(7)	2.469(8)
La2-O3 [x 2]	2.599(9)	2.632(8)	2.605(6)	2.602(8)	2.620(9)
La2-O4	2.309(2)	2.316(2)	2.307(3)	2.306(7)	2.312(16)
Average	2.539	2.542	2.537	2.531	2.528
Si-O1	1.554(19)	1.600(18)	1.567(15)	1.659(17)	1.616(20)
Si-O2	1.587(14)	1.579(13)	1.617(11)	1.667(12)	1.589(16)
Si-O3 [x 2]	1.569(8)	1.574(8)	1.622(6)	1.528(8)	1.579(9)
Average	1.570	1.582	1.607	1.596	1.591

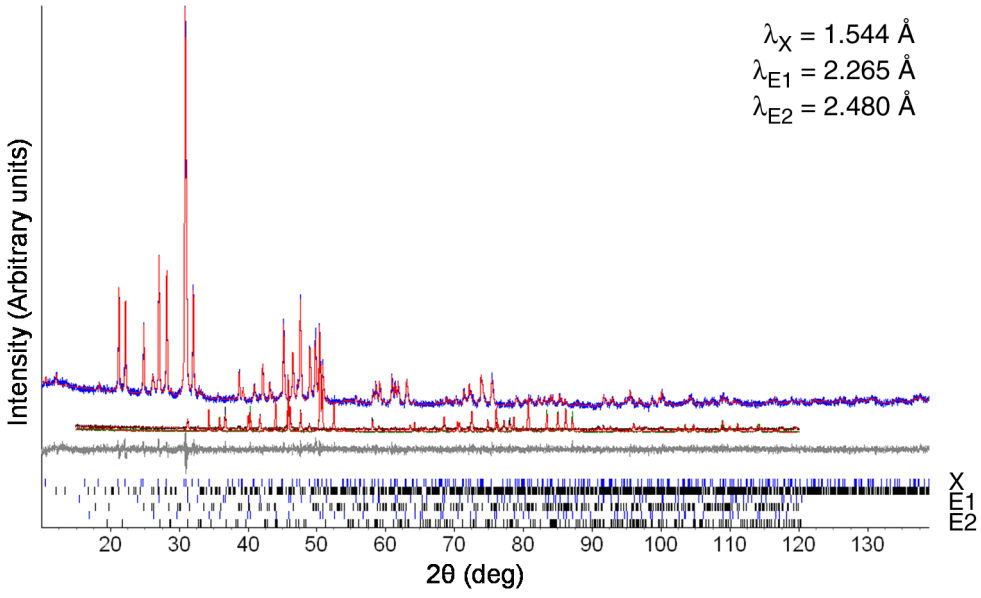

Figure 46 Observed (dotted), calculated (line) and difference (bottommost) Rietveld plots for $La_{9.12}Na_{0.60}(SiO_4)_6O_2$ (94(1) wt.%) co-existing with $P2_1/c$ $La_2Si_2O_7$ (6(1) wt.%). Three patterns (X, E1, E2) were refined simultaneously and for each phase pair the apatite Bragg markers are uppermost.

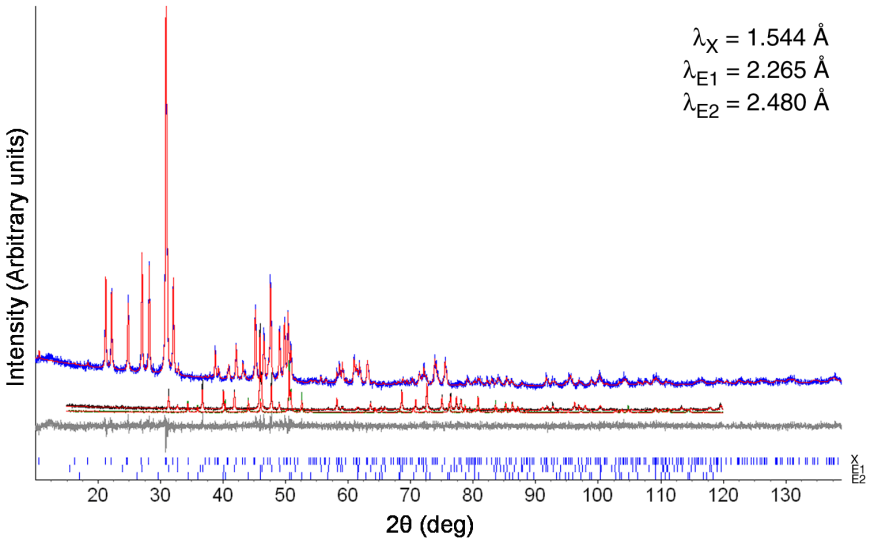

Figure 47 Observed (dotted), calculated (full line) and difference (bottom) XRD profiles for $La_8Na_2(SiO_4)_6(OH)_2$. Bragg markers are for $P6_3/m$ phase.

4.4.4 Conclusion: Crystallochemical Constraints and Structural Complexity

The insertion of extrastoichiometric oxygen and creation of vacancies are essential to optimize apatites as solid oxide fuel cell electrolytes. In silicate apatites the rigid SiO_4 tetrahedra and compact framework, compared to germanate, make it relatively difficult to introduce interstitial oxygen between the tetrahedra. Consequently, although $La_{10}Ge_6O_{27}$ is an established $P\bar{1}$ apatite – 2*A* phase, $La_{10}Si_6O_{27}$ may be impossible to form at ambient pressure. It follows that lanthanum vacancies, together with oxygen interstitials play a more significant role in silicates during conduction, compared to analogous germanates. While the average structure is frequently reported as $La^{I}_{3.33}\square^{I}_{0.67}La^{II}_{6}(SiO_4)_6O_2$, this apatite may be better described as a disordered N = 6 $La_{10}\square_2La_{18}(SiO_4)_6(Si_2O_7)_3(Si_2O_9)_3O_2$ polysome in accord with ^{29}Si NMR revealing three chemical shifts assigned to SiO_4, distorted SiO_4 and Si_2O_7.[11,28] The Si_nO_{3n+1} chains for polysomates with $N > 2$, may not show long range order due to Si-Si repulsion, and further study is required to detect and characterize polysomatic intergrowths. These future experiments will include other spectroscopy techniques, such as FTIR, Raman and EXAFS, and neutron diffraction. Although the oxygen conductivity in these sodium-bearing apatites was not high, this analysis and interpretation does provide guidance for the tailoring of solid state electrolytes. Moreover, semi-empirical atomistic modeling (Section 4.3), would be valuable to further validate the nature of ion migration in these compounds.

4.5 Rhenium Apatite Electrolytes – The Prospects for Highly Oxidized Polytypes

4.5.1 Rhenium as an Enabler for Oxygen Mobility

The preceding sections have demonstrated that high oxide ion conductivity is achieved primarily by introducing extrastoichiometric oxygen into the $A_{10}(BO_4)_6O_2$ apatite prototype. Hybrids such as $La_{10}(GeO_4)_5(GeO_5)O_2$ position the interstitial oxygen in the framework rather than the conventionally assumed tunnel position.[130] In this well established example, the additional oxygen migrates *via* GeO_4 tetrahedral pairs to create transient Ge_2O_9 units that facilitate inter-tunnel O^{2-} penetration through a saddle point at (0, 0, ½).[29,144] This movement is made possible by the cooperative displacement of the surrounding tetrahedra.

It can be hypothesized that a fully oxidized apatite such as $Ba_{10}(ReO_5)_6O_2$ will have superior ionic conduction because six additional oxygens are located in the framework per unit cell. Earlier studies determined that $Ba_{10}(ReO_5)_6O_2$ crystallizes in $P6_3cm$ where the framework composition is $Ba^{I}_4(ReO_5)_6$ and the tunnel is filled with $Ba^{II}_6X_2$ (X = superoxide ion O_2^-) as confirmed by single crystal X-ray diffraction and Raman spectroscopy.[113] In this case, the "extra" oxygen is more strongly bound to the rhenium centered square pyramid than for GeO_4/GeO_5 in $La_{10}(GeO_4)_5(GeO_5)O_2$. The related apatites $Sr_{10}(ReO_5)_6X_2$ (X = Cl, Br and I) adopt a different structure (*Pnma*) to the Ba analogue. In $Sr_{10}(ReO_5)_6X_2$, the ReO_5 apical oxygen directionality is antiparallel between the SrO_6 metaprism columns while it is unidirectional in $Ba_{10}(ReO_5)_6X_2$ (Figure 48).[75] It is probable that the orientation of the ReO_5 square pyramids modulate the underlying structure to create longer period ordering.

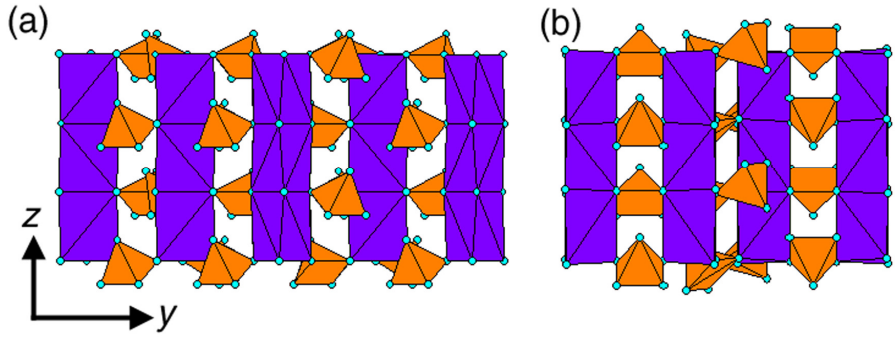

Figure 48 Crystal structure of (a) $Ba_{10}(ReO_5)_6X_2$ and (b) $Sr_{10}(ReO_5)_6X_2$ transformed into the same orientation as the Ba analogue; $(Ba,Sr)O_6$ metaprisms are shown in purple while the ReO_5 square pyramids are in brown. These two structures have different ReO_5 directionality.

Therefore, it is of fundamental interest to examine the structural transformation between the Ba- and Sr-rhenates and correlate possible incommensuration with oxygen mobility. In this section, a reconnaissance investigation of $(Ba,Sr)_{10}(ReO_5)_6O_2$ apatites demonstrates these materials show excellent conductivity in their own right, with these insights providing guidance for the design of new hybrid apatite electrolytes.

4.5.2 Structure of $Ba_{10}(ReO_5)_6O_2$

Selected area electron diffraction (SAED) patterns from [001] and [010] zones revealed a commensurate supercell (Figure 49). Using $P6_3cm$ as the parent structure ($a = b = 10.98$ Å, c = 7.79 Å), double and triple repeats in b and c were observed, while a retained the subcell dimension. Single crystal electron diffraction patterns could be indexed as a supercell with $a_s = a_p$, $b_s = 2b_p$, $c_s = 3c_p$.

$$\begin{pmatrix} a_s \\ b_s \\ c_s \end{pmatrix} = \begin{pmatrix} 1 & 0 & 0 \\ 0 & 2 & 0 \\ 0 & 0 & 3 \end{pmatrix} \begin{pmatrix} a_p \\ b_p \\ c_p \end{pmatrix} \quad \textbf{(33)}$$

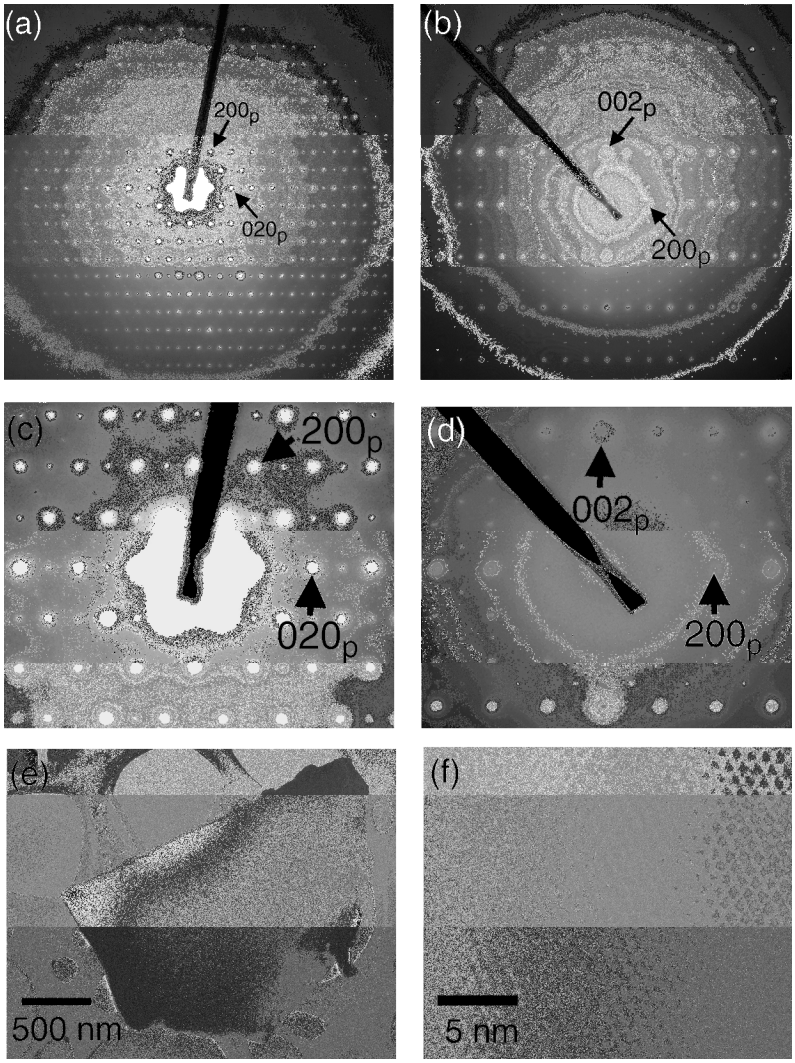

Figure 49 SAED of $Ba_{10}(ReO_5)_6O_2$ along (a, c) [001] and (b, d) [010] with (e) low magnification and (f) HRTEM images along [001]. The subcell reflections are indexed, with strong commensurate supercell ordering.

Laboratory and synchrotron powder X-ray diffraction data were Pawley-fitted with the reported structure in $P6_3cm$ and modeled virtually all reflections. Lowering the symmetry to the $P2_1$ sub-group provided a better intensity match to the main reflections, but could not account for the weak reflections. Therefore, atomic positions in the supercell recognized by electron diffraction were determined by matrix inversion and transposition as follows.

$$M = \begin{pmatrix} 1 & 0 & 0 \\ 0 & 2 & 0 \\ 0 & 0 & 3 \end{pmatrix};\ M^{-1} = \begin{pmatrix} 1 & 0 & 0 \\ 0 & \frac{1}{2} & 0 \\ 0 & 0 & \frac{1}{3} \end{pmatrix};\ \left(M^{-1}\right)^T = \begin{pmatrix} 1 & 0 & 0 \\ 0 & \frac{1}{2} & 0 \\ 0 & 0 & \frac{1}{3} \end{pmatrix} \quad \textbf{(34)}$$

For example, the atomic coordinates of Ba1 in the 4*b* Wyckoff position in $P6_3cm$ space group are:

$$\left(\frac{2}{3},\frac{1}{3},0\right);\ \left(\frac{1}{3},\frac{2}{3},0\right);\ \left(\frac{2}{3},\frac{1}{3},\frac{1}{2}\right);\ \left(\frac{1}{3},\frac{2}{3},\frac{1}{2}\right)$$

The supercell, which is six times larger of parent cell, contains 24 Ba atoms (Figure 50, Table 35). After applying symmetry restrictions (2_1 along *c*; i.e. $\bar{x}$, $\bar{y}$, $z+\frac{1}{2}$), these 24 atoms are reduced to the 12 atoms of the asymmetric unit (Table 36). Rietveld analysis using this cell and $P2_1$ reduced R_{wp} substantially (Table 37, Figures 51a and b) and allowed the refinement of all 144 atoms in the unit cell (Table 38).

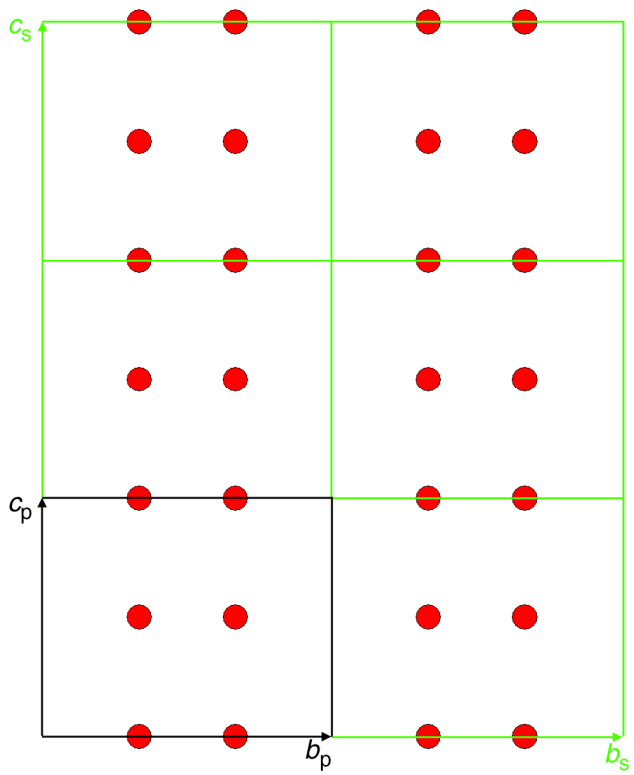

Figure 50 Ba1 position in parent cell (black) and supercell (green) projected along [100].

Table 35 Atomic coordinates of Ba1 in the parent cell and corresponding supercell.

x	*y*	*z*
0.666667	0.333333	0
0.333333	0.666667	0
0.666667	0.333333	0.5
0.333333	0.666667	0.5
0.666667	0.333333	1
0.333333	0.666667	1
0.666667	0.333333	1.5
0.333333	0.666667	1.5
0.666667	0.333333	2
0.333333	0.666667	2
0.666667	0.333333	2.5
0.333333	0.666667	2.5
0.666667	1.333333	0
0.333333	1.666667	0
0.666667	1.333333	0.5
0.333333	1.666667	0.5
0.666667	1.333333	1
0.333333	1.666667	1
0.666667	1.333333	1.5
0.333333	1.666667	1.5
0.666667	1.333333	2
0.333333	1.666667	2
0.666667	1.333333	2.5
0.333333	1.666667	2.5

supercell →

x	*y*	*z*
0.666667	0.166667	0
0.333333	0.333333	0
0.666667	0.166667	0.166667
0.333333	0.333333	0.166667
0.666667	0.166667	0.333333
0.333333	0.333333	0.333333
0.666667	0.166667	0.5
0.333333	0.333333	0.5
0.666667	0.166667	0.666667
0.333333	0.333333	0.666667
0.666667	0.166667	0.833333
0.333333	0.333333	0.833333
0.666667	0.666667	0
0.333333	0.833333	0
0.666667	0.666667	0.166667
0.333333	0.833333	0.166667
0.666667	0.666667	0.333333
0.333333	0.833333	0.333333
0.666667	0.666667	0.5
0.333333	0.833333	0.5
0.666667	0.666667	0.666667
0.333333	0.833333	0.666667
0.666667	0.666667	0.833333
0.333333	0.833333	0.833333

Table 36 Ba1 positions in $P2_1$ space group.

x	*y*	*z*
0.666667	0.166667	0
0.666667	0.166667	0.166667
0.666667	0.166667	0.333333
0.666667	0.166667	0.5
0.666667	0.166667	0.666667
0.666667	0.166667	0.833333
0.666667	0.666667	0
0.666667	0.666667	0.166667
0.666667	0.666667	0.333333
0.666667	0.666667	0.5
0.666667	0.666667	0.666667
0.666667	0.666667	0.833333

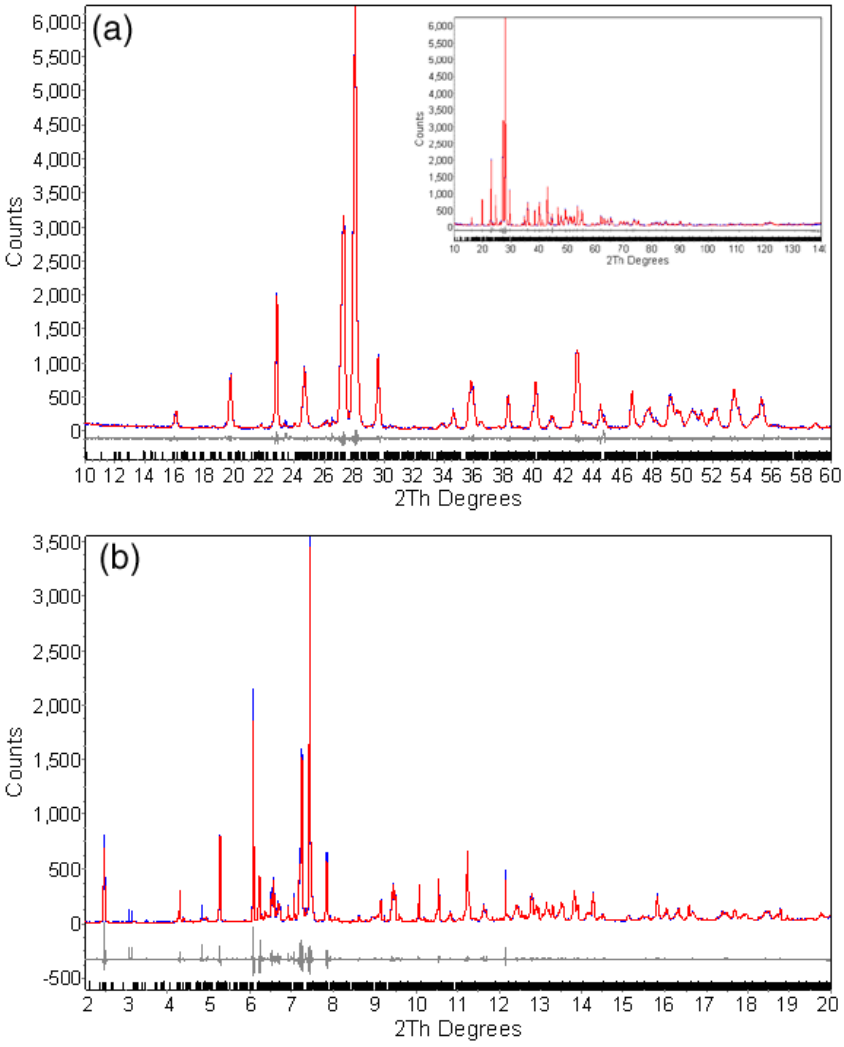

Figure 51 (a) Laboratory and (b) synchrotron powder XRD of $Ba_{10}(ReO_5)_6O_2$ with the supercell $P2_1$ space group.

Table 37 Unit cell parameters of $Ba_{10}(ReO_5)_6O_2$ refined using Pawley fitting.

	Synchrotron XRD		
	$P6_3cm$	$P2_1$	$P2_1$ (supercell)
R_{wp}	30.1	25.6	10.8
a (Å)	11.117(1)	11.0109(6)	11.1237(6)
b (Å)	11.117(1)	10.8059(6)	22.108(1)
c (Å)	7.7894(1)	7.7900(1)	23.3708(2)
γ (°)	120	119.85(1)	120.65(1)
Volume (Å^3)	827.5(2)	803.93(7)	4944.4(4)

Table 38 Unit cell and atomic parameters of $Ba_{10}(ReO_5)_6O_2$ refined using Rietveld fitting.

R_{wp}/R_b	18.6/9.0
a (Å)	10.9800(1)
b (Å)	22.1128(6)
c (Å)	23.3705(2)
γ (°)	120.24(1)
Volume (Å^3)	4902.0 (2)

	Wyckoff position	x	y	z	occupancy	Beq
Ba1	2*a*	0.654(3)	0.166(1)	0.004(1)	1	0.91(9)
Ba2	2*a*	0.661(2)	0.659(1)	0.009(1)	1	0.91(9)
Ba3	2*a*	0.672(2)	0.156(1)	0.330(1)	1	0.91(9)
Ba4	2*a*	0.690(2)	0.666(1)	0.335(1)	1	0.91(9)
Ba5	2*a*	0.726(2)	0.192(1)	0.632(1)	1	0.91(9)
Ba6	2*a*	0.679(3)	0.676(1)	0.675(1)	1	0.91(9)
Ba7	2*a*	0.667(3)	0.179(1)	0.176(1)	1	0.91(9)
Ba8	2*a*	0.673(3)	0.666(2)	0.167(1)	1	0.91(9)
Ba9	2*a*	0.672(3)	0.163(1)	0.503(1)	1	0.91(9)
Ba10	2*a*	0.694(2)	0.687(1)	0.497(1)	1	0.91(9)
Ba11	2*a*	0.656(2)	0.179(1)	0.834(1)	1	0.91(9)
Ba12	2*a*	0.649(3)	0.665(1)	0.840(1)	1	0.91(9)
Ba13	2*a*	0.237(2)	0.458(1)	0.085(1)	1	0.91(9)
Ba14	2*a*	0.217(2)	0.986(1)	0.110(1)	1	0.91(9)
Ba15	2*a*	0.270(2)	0.499(1)	0.423(1)	1	0.91(9)
Ba16	2*a*	0.258(2)	0.001(1)	0.430(1)	1	0.91(9)
Ba17	2*a*	0.257(3)	0.494(1)	0.756(1)	1	0.91(9)
Ba18	2*a*	0.237(2)	0.015(1)	0.744(1)	1	0.91(9)
Ba19	2*a*	0.991(2)	0.146(1)	0.095(1)	1	0.91(9)
Ba20	2*a*	0.986(2)	0.616(1)	0.083(1)	1	0.91(9)
Ba21	2*a*	0.004(2)	0.123(1)	0.423(1)	1	0.91(9)
Ba22	2*a*	0.998(2)	0.618(1)	0.428(1)	1	0.91(9)
Ba23	2*a*	0.031(2)	0.139(1)	0.765(1)	1	0.91(9)
Ba24	2*a*	0.985(2)	0.628(1)	0.765(1)	1	0.91(9)
Ba25	2*a*	0.734(2)	0.373(1)	0.090(1)	1	0.91(9)
Ba26	2*a*	0.736(2)	0.864(1)	0.088(1)	1	0.91(9)
Ba27	2*a*	0.726(2)	0.343(1)	0.422(1)	1	0.91(9)
Ba28	2*a*	0.807(2)	0.906(1)	0.405(1)	1	0.91(9)
Ba29	2*a*	0.754(2)	0.372(1)	0.753(1)	1	0.91(9)
Ba30	2*a*	0.750(2)	0.887(1)	0.762(1)	1	0.91(9)
Re1	2*a*	0.3879(9)	0.9873(6)	0.2364(6)	1	1.35(7)

Re2	2*a*	0.371(1)	0.5048(6)	0.2438(5)	1	1.35(7)
Re3	2*a*	0.3895(9)	0.9881(5)	0.5798(7)	1	1.35(7)
Re4	2*a*	0.415(1)	0.5062(6)	0.5785(6)	1	1.35(7)
Re5	2*a*	0.402(1)	0.0025(5)	0.9007(7)	1	1.35(7)
Re6	2*a*	0.391(1)	0.5056(6)	0.9087(6)	1	1.35(7)
Re7	2*a*	0.005(1)	0.1948(6)	0.2380(6)	1	1.35(7)
Re8	2*a*	0.008(1)	0.7065(6)	0.2398(6)	1	1.35(7)
Re9	2*a*	0.006(1)	0.1988(6)	0.5732(6)	1	1.35(7)
Re10	2*a*	0.006(1)	0.6946(5)	0.5682(5)	1	1.35(7)
Re11	2*a*	0.969(1)	0.1750(5)	0.9107(6)	1	1.35(7)
Re12	2*a*	0.994(1)	0.7071(6)	0.9047(6)	1	1.35(7)
Re13	2*a*	0.609(1)	0.3092(6)	0.2438(6)	1	1.35(7)
Re14	2*a*	0.6011(9)	0.8046(6)	0.2345(8)	1	1.35(7)
Re15	2*a*	0.605(1)	0.2956(5)	0.5698(6)	1	1.35(7)
Re16	2*a*	0.618(1)	0.8063(5)	0.5739(5)	1	1.35(7)
Re17	2*a*	0.598(1)	0.2929(6)	0.9085(5)	1	1.35(7)
Re18	2*a*	0.616(1)	0.8118(6)	0.9029(5)	1	1.35(7)
O1	2*a*	0.292(4)	0.005(2)	0.287(3)	1	0.1(4)
O2	2*a*	0.360(6)	0.512(5)	0.334(3)	1	0.1(4)
O3	2*a*	0.247(5)	0.932(3)	0.626(3)	1	0.1(4)
O4	2*a*	0.388(7)	0.490(4)	0.661(3)	1	0.1(4)
O5	2*a*	0.32(1)	0.934(3)	0.955(3)	1	0.1(4)
O6	2*a*	0.412(8)	0.547(5)	0.986(3)	1	0.1(4)
O7	2*a*	0.98(1)	0.143(3)	0.307(3)	1	0.1(4)
O8	2*a*	0.028(7)	0.661(3)	0.301(3)	1	0.1(4)
O9	2*a*	0.064(9)	0.280(2)	0.616(3)	1	0.1(4)
O10	2*a*	0.027(7)	0.655(3)	0.633(3)	1	0.1(4)
O11	2*a*	0.999(8)	0.184(4)	0.991(3)	1	0.1(4)
O12	2*a*	0.094(5)	0.697(2)	0.959(3)	1	0.1(4)
O13	2*a*	0.754(5)	0.342(5)	0.298(3)	1	0.1(4)
O14	2*a*	0.801(5)	0.848(4)	0.224(4)	1	0.1(4)
O15	2*a*	0.57(1)	0.235(3)	0.624(3)	1	0.1(4)
O16	2*a*	0.640(7)	0.813(3)	0.658(3)	1	0.1(4)
O17	2*a*	0.65(1)	0.307(5)	0.985(3)	1	0.1(4)
O18	2*a*	0.67(1)	0.845(4)	0.977(3)	1	0.1(4)
O19	2*a*	0.573(5)	0.047(6)	0.266(6)	1	0.1(4)
O20	2*a*	0.574(5)	0.550(4)	0.247(4)	1	0.1(4)
O21	2*a*	0.486(4)	0.937(2)	0.577(4)	1	0.1(4)
O22	2*a*	0.598(4)	0.581(3)	0.582(5)	1	0.1(4)
O23	2*a*	0.586(5)	0.057(7)	0.919(5)	1	0.1(4)
O24	2*a*	0.561(5)	0.530(3)	0.931(3)	1	0.1(4)
O25	2*a*	0.872(4)	0.216(2)	0.229(7)	1	0.1(4)
O26	2*a*	0.977(4)	0.768(3)	0.268(3)	1	0.1(4)
O27	2*a*	0.829(4)	0.179(3)	0.580(5)	1	0.1(4)
O28	2*a*	0.987(3)	0.768(3)	0.584(3)	1	0.1(4)
O29	2*a*	0.928(4)	0.244(2)	0.915(6)	1	0.1(4)
O30	2*a*	0.923(5)	0.760(3)	0.876(3)	1	0.1(4)
O31	2*a*	0.53(2)	0.215(2)	0.234(7)	1	0.1(4)
O32	2*a*	0.408(5)	0.745(7)	0.240(5)	1	0.1(4)
O33	2*a*	0.50(1)	0.216(2)	0.606(3)	1	0.1(4)
O34	2*a*	0.51(1)	0.718(2)	0.541(3)	1	0.1(4)
O35	2*a*	0.586(7)	0.218(2)	0.946(3)	1	0.1(4)
O36	2*a*	0.63(1)	0.795(3)	0.831(3)	1	0.1(4)

O37	2*a*	0.90(1)	0.215(2)	0.089(3)	1	0.1(4)
O38	2*a*	0.90(1)	0.707(2)	0.067(6)	1	0.1(4)
O39	2*a*	0.086(5)	0.245(3)	0.434(3)	1	0.1(4)
O40	2*a*	0.036(4)	0.746(3)	0.416(4)	1	0.1(4)
O41	2*a*	0.88(1)	0.208(2)	0.763(3)	1	0.1(4)
O42	2*a*	0.890(9)	0.720(2)	0.768(3)	1	0.1(4)
O43	2*a*	0.629(8)	0.102(2)	0.099(4)	1	0.1(4)
O44	2*a*	0.746(5)	0.584(2)	0.076(5)	1	0.1(4)
O45	2*a*	0.63(1)	0.090(2)	0.408(4)	1	0.1(4)
O46	2*a*	0.647(7)	0.584(2)	0.393(7)	1	0.1(4)
O47	2*a*	0.505(4)	0.055(2)	0.748(7)	1	0.1(4)
O48	2*a*	0.526(5)	0.541(2)	0.751(5)	1	0.1(4)
O49	2*a*	0.419(4)	0.132(2)	0.038(3)	1	0.1(4)
O50	2*a*	0.525(4)	0.673(2)	0.071(5)	1	0.1(4)
O51	2*a*	0.587(5)	0.248(4)	0.404(3)	1	0.1(4)
O52	2*a*	0.593(4)	0.734(6)	0.411(4)	1	0.1(4)
O53	2*a*	0.518(4)	0.156(2)	0.723(5)	1	0.1(4)
O54	2*a*	0.554(4)	0.690(2)	0.758(8)	1	0.1(4)
O55	2*a*	0.288(4)	0.034(2)	0.237(5)	1	0.1(4)
O56	2*a*	0.40(1)	0.559(2)	0.178(3)	1	0.1(4)
O57	2*a*	0.270(4)	0.023(2)	0.571(7)	1	0.1(4)
O58	2*a*	0.459(8)	0.599(2)	0.583(5)	1	0.1(4)
O59	2*a*	0.349(4)	0.061(2)	0.868(3)	1	0.1(4)
O60	2*a*	0.363(7)	0.541(3)	0.842(3)	1	0.1(4)
O61	2*a*	0.858(5)	0.181(3)	0.197(3)	1	0.1(4)
O62	2*a*	0.91(1)	0.648(4)	0.182(3)	1	0.1(4)
O63	2*a*	0.92(1)	0.130(3)	0.519(3)	1	0.1(4)
O64	2*a*	0.863(8)	0.605(2)	0.566(6)	1	0.1(4)
O65	2*a*	0.823(5)	0.097(3)	0.887(3)	1	0.1(4)
O66	2*a*	0.883(5)	0.686(6)	0.842(3)	1	0.1(4)
O67	2*a*	0.643(7)	0.283(3)	0.174(3)	1	0.1(4)
O68	2*a*	0.799(5)	0.847(4)	0.220(6)	1	0.1(4)
O69	2*a*	0.623(6)	0.302(3)	0.481(3)	1	0.1(4)
O70	2*a*	0.813(4)	0.840(6)	0.558(5)	1	0.1(4)
O71	2*a*	0.61(1)	0.321(5)	0.835(3)	1	0.1(4)
O72	2*a*	0.744(5)	0.794(3)	0.873(3)	1	0.1(4)
O73	2*a*	0.988(8)	0.318(7)	0.989(3)	1	0.1(4)
O74	2*a*	0.95(1)	0.765(4)	0.000(3)	1	0.1(4)
O75	2*a*	0.837(4)	0.289(3)	0.393(6)	1	0.1(4)
O76	2*a*	0.863(4)	0.783(5)	0.369(3)	1	0.1(4)
O77	2*a*	0.855(5)	0.287(4)	0.691(3)	1	0.1(4)
O78	2*a*	0.898(5)	0.813(2)	0.682(3)	1	0.1(4)
O79	2*a*	0.774(4)	0.020(3)	0.054(4)	1	0.1(4)
O80	2*a*	0.67(1)	0.522(4)	0.004(3)	1	0.1(4)
O81	2*a*	0.753(4)	0.066(2)	0.435(3)	1	0.1(4)
O82	2*a*	0.748(5)	0.576(2)	0.437(3)	1	0.1(4)
O83	2*a*	0.759(5)	0.049(6)	0.687(3)	1	0.1(4)
O84	2*a*	0.775(5)	0.563(3)	0.703(3)	1	0.1(4)
O85	2*a*	0.391(4)	0.126(2)	0.035(3)	1	0.1(4)
O86	2*a*	0.477(4)	0.654(2)	0.084(3)	1	0.1(4)
O87	2*a*	0.36(1)	0.141(2)	0.334(3)	1	0.1(4)
O88	2*a*	0.420(5)	0.666(2)	0.347(3)	1	0.1(4)
O89	2*a*	0.397(5)	0.115(2)	0.755(5)	1	0.1(4)

O90	2*a*	0.400(5)	0.661(2)	0.673(3)	1	0.1(4)
O91	2*a*	0.02(3)	0.00(2)	0.12(2)	0.5	1
O92	2*a*	0.05(4)	0.51(2)	0.11(2)	0.5	1
O93	2*a*	0.96(3)	0.03(2)	0.51(2)	0.5	1
O94	2*a*	-0.08(4)	0.46(2)	0.40(2)	0.5	1
O95	2*a*	0.01(4)	0.88(2)	0.83(2)	0.5	1
O96	2*a*	0.10(4)	0.57(2)	0.72(2)	0.5	1

4.5.3 Oxygen Conductivity in Rhenium Apatite

Oxygen conductivity in $Ba_{10}(ReO_5)_6O_2$ was slightly improved over $La_{10}(GeO_4)_5(GeO_5)O_2$, but lower than for $La_9Sr(GeO_4)_{5.5}(GeO_5)_{0.5}O_2$. Mobility increases with temperature and reaches a maximum at 740°C before decreasing. $Sr_{10}(ReO_5)_6O_2$ has the poorest conductivity with $Ba_5Sr_5(ReO_5)_6O_2$ showing intermediate behavior (Figure 52). Although the Re framework is rich in "extrastoichiometric" oxygen, this does not translate directly to high conductivity due to the strong bonding in the ReO_5 square pyramid. This is distinct from the transient oxygen in germanate apatites. In addition, commensuration may affect apatite performance and complicate correlating structure with performance in these electrolyte apatites.

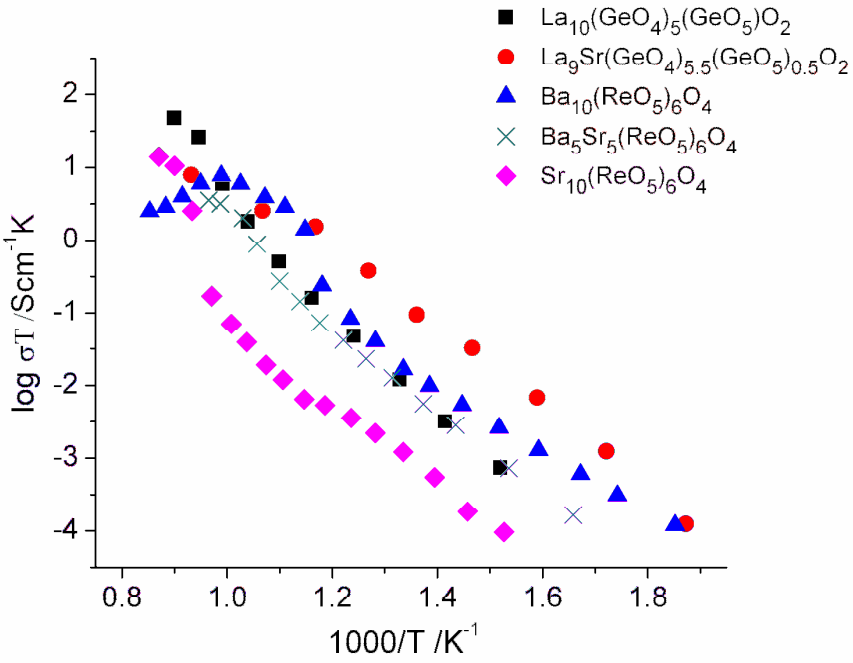

Figure 52 Variation of conductivities with temperature for germanium and rhenium apatites.

4.5.4 Conclusion: Future Tailoring of Rhenate Hybrid Electrolytes

As the interstitial oxygen in the rhenate apatite is more abundant than the germanate hybrid with comparable conductivity, a rationale to enhance migration is to introduce a degree of non-stoichiometry (oxygen / cation vacancy). For example, a vacancy could act as a saddle site for oxygen during transport, and this might be achieved by altervalent substitution of Re^{7+} with Ge^{4+} as:

$$2Re^{7+} + 3O^{2-} \rightarrow 2Ge^{4+} + \square_{O}^{2-} \quad \textbf{(35)}$$

or $(Ba/Sr)^{2+}$ with Na^{+}

$$2(Ba,Sr)^{2+} + O^{2-} \rightarrow 2Na^{+} + \square_{O}^{2-} \quad \textbf{(36)}$$

Clearly, a systematic examination of doping strategies is required to optimize this new electrolyte chemistry and is beyond the scope of the present thesis. Such an investigation is likely to be challenging due to structural modulation that may attenuate performance in unexpected ways. Furthermore, atomistic simulations will be computationally expensive, and may not be appropriate for the long period structures identified in these preliminary experiments.

Chapter 5

Conclusions and Future Work

5.1 Conclusions

Solid oxide fuel cells (SOFCs) are electrochemical devices for converting chemical energy into electricity that will be a key technology replacing non-renewable fossil fuels. In this thesis, a range of germanate, silicate and rhenate apatites were investigated as novel electrolytes for SOFC. Apatites can be described as one-dimensional tunnel structures with zeolitic character, in which the $[A^{I}_4][A^{II}_6][(BO_4)_6][X]_2$ motif flexes in response to cation and anion substitutions. White *et al.*[25,75] mapped the apatite family into $[A^{I}_4][A^{II}_6][(BO_3)_6][X]_2$, $[A^{I}_4][A^{II}_6][(BO_4)_6][X]_2$ and $[A^{I}_4][A^{II}_6][(BO_5)_6][X]_2$ genera. Here, this taxonomy was expanded by introducing hybrid $A_{10}(BO_4)_{6-x}(BO_5)_xX_2$ forms through the recognition of $La_{10}(GeO_4)_5(GeO_5)O_2$ as a prototype electrolyte which contains germanium in tetrahedral and trigonal bipyramidal coordination. The direct location of the interstitial oxygen responsible for conduction was established for the first time by Fourier analysis of neutron diffraction data. Furthermore, the framework interstitial oxygen promotes co-operative displacements of the Ge3, O3, O6, O9 and O12 atoms, permitting a re-analysis of oxygen migration in SOFC apatites that rationalizes intra-tunnel and inter-tunnel conduction. When this oxidized apatite is heated to fuel cell operating temperatures, the structure transforms from triclinic apatite – 2*A* to hexagonal apatite – 2*H* through a possible intervening monoclinic apatite – 2*M* polymorph.

By selective doping of the *A* site with alkaline earths (*AE* = Ca, Sr and Ba), the concentration of oxygen vacancies and interstitials can be controlled through

$$RE^{3+} + \tfrac{1}{2}\,O^{2-} \rightarrow AE^{2+} + \tfrac{1}{2}\,\square_{O^{2-}} \qquad \textbf{(37)}$$

where *RE* is the rare earth. Ionic conductivity is dependent on two factors – the transient oxide ion concentration and activation energy, and $La_9Ca(GeO_4)_{5.5}(GeO_5)_{0.5}O_2$ provided the optimal balance between these. When excess *AE*s are introduced, as for example in $La_6Sr_4(GeO_4)_6O_2H_\delta$, the lack of interstitial oxide ion results in poor conduction. In general, $La_{10-x}Sr_xGe_6O_{27-x/2}$ compounds undergo pseudomorphic transformations from $P\bar{1}$ ($0 \leq x \leq 1$) to $P2_1/m$ ($1 \leq x \leq 2.96$) and finally to $P6_3/m$ ($2.96 \leq x \leq 5.32$). Furthermore, polysomatic apatites can be

synthesized when more than two apatite modules are stacked in an ordered fashion, with polysomes in silicate-based electrolytes also playing a role. These studies led to the systematization of polymorphic (driven by change in temperature), pseudomorphic (initiated by compositional adjustments), polysomatic transformations (stacking of *n*-modules which may stabilize *A* cation substoichiometry) and the construction of a hybrid taxonomy map for the apatite family. Using anomalous scattering of synchrotron X-ray diffraction to examine the $La_{9.33-x/3}Na_x(SiO_4)_6O_2$ series provided the La/Na partitioning over the A^{I} and A^{II} sites and the reliable determination of symmetry. As the BO_5 component is crucial to the functionality of apatite electrolytes, the fully oxidized $Ba_{10}(ReO_5)_6O_2$ apatite, which contains a five times higher interstitial oxygen concentration was explored. The conductivity was comparable to the germanate $La_{10}(GeO_4)_5(GeO_5)O_2$ because the 'interstitial' oxygen in the rhenate is more tightly bound to the *B* cation and does not migrate readily.

5.2 Novelty and Innovation

The key outcomes of these investigations are that:

- Apatite pseudomorphism promoted by altervalent substitution, and temperature driven polymorphic transformations in electrolytes has been partially mapped for the first time. Polysomatic nomenclature is adapted to summarize these structural modifications.
- The incorporation of extrastoichiometric framework oxygen improves ionic conductivity and is accompanied by symmetry reduction from the conventional $P6_3/m$ setting to $P\bar{1}$ with the probable intervention of a $P2_1/m$ phase for all compositions. These experimental observations are consistent with atomistic modeling which predicts oxygen disorder in the vicinity of the tetrahedra. In addition, inter-tunnel migration pathways allow significant conduction across, as well as along, the tunnels.
- Displacement of lanthanum by alkaline earths in germanate apatites drives a pseudomorphic transformation of apatite hybrids with the highest conductivity observed for $La_9AE(GeO_4)_{5.5}(GeO_5)_{0.5}O_2$ (*AE* = Ca). This superior performance is ascribed to the optimum balance between interstitial oxygen

content and activation energy. At higher Sr loadings, charge balance is achieved by proton addition rather than the commonly assumed creation of tunnel oxygen vacancies. In the case of alkali metal doping (i.e. Na) the precise *A*-site partitioning was extracted from multiple wavelength anomalous diffraction. However, the quantitative assessment of $A^{I}O_6$ metaprism twisting that underpins the linkage of ionic migration to structure could not be established; neutron diffraction will be essential to accomplish this correlation.

- "Excess" oxygens introduced commensurately within the framework of "oxidized" rhenate apatites resulted in high conductivity, and these compounds might be tailored for inclusion in novel apatite electrolyte designs.

Although this research has led to a deeper understanding of apatite polymorphism and pseudomorphism and the implications of these crystallochemical modifications for oxygen migration, outstanding questions remain. Specifically:

- Inflections in lattice constant trends reflect crystal structure transformations, with distinct oxygen diffusion behavior for triclinic – 2*A*, monoclinic – 2*M* and hexagonal – 2*H* forms. This linkage is unequivocal, but requires further examination.
- The limitation of powder diffraction studies must be recognized, and despite the difficulty of growing large refractory apatite crystals, structure determination from single crystal polymorphs will be essential to comprehensively couple structure modification to conductivity and thereby design systems that optimize performance. Furthermore diffraction studies offer only a partial, and sometimes deceptively simple, representation of the crystal structure.
- Supplementary analysis by NMR and FTIR spectroscopies are essential and should be correlated with X-ray and neutron diffraction to yield a consistent description of electrolyte crystal chemistry.

5.3 Outstanding Crystallographic Questions

Because interstitial oxygen that promotes higher conductivity is located in the framework, the synthesis of BO_4/BO_5 hybrids is an obvious means to enhance conductivity. Hybrids can be designed by introducing high valence *B* cations such as Re^{7+} and W^{6+}, although their stability under reducing atmospheres needs further examination. To this end, the following altervalent substitutions might be attempted:

$GeO_4^{4-} \rightarrow WO_4^{2-} + O^{2-} \rightarrow WO_5^{4-}$ $(La_{9.33}(GeO_4)_{6-x}(WO_5)_xO_2)$

$2GeO_4^{4-} \rightarrow 2PO_4^{3-} + O^{2-} \rightarrow PO_4^{3-} + PO_5^{5-}$ $(La_{9.33}(GeO_4)_{6-x}(PO_4)_{x/2}(PO_5)_{x/2}O_2)$

Recent work by Kendrick *et al.*[94] with Y^{3+} doped germanate apatite found symmetry can attenuate ion conduction with hexagonal compounds superior to triclinic, in accord with the current investigations. Therefore it would be fruitful to identify strategies to stabilize apatite – 2*H* polymorphs at fuel cell operating temperatures. In addition, the metaprism twist angle, could serve as a universal functional parameter, analogous to octahedral tilting in perovskite systems, that controls the tunnel diameter, and hence conductivity.

5.4 Outstanding Ion Migration Questions

Although this research focused solely on the apatite-2*S* polysomes, condensation of apatite modules into tri- or tetra-modular structures to create B_2O_7 and B_3O_{10} units are worthy of exploration as the cage structure in $La_{9.33}\square_{0.67}(Si/GeO_4)_6O_2$ described in Section 2.4.2 is predicted to be essential for ion migration. In addition, the effect of BO_3 in reduced apatites $A_{10}(BO_3)_6O_2$ with regards to ion conductivity should be addressed to complete the crystallochemical map of structure versus functionality.

A dynamic TEM study that exploits the high spatial and temporal resolution possible in spherical aberration (C_s) corrected instruments could be used to observe tetrahedral / square pyramidal distortion that allows O^{2-} to migrate at high operating temperature. Convergent beam electron diffraction and high resolution TEM are crucial to specify crystallographic diffusion mechanisms with respect to atomic scale order–disorder

phenomena and incommensurate-commensurate modulation of apatites, together with the support of spectroscopy.

5.5 Outstanding Device Fabrication Questions

Commercialization of solid oxide fuel cells requires fast and economical fabrication while achieving optimum performance. In a SOFC, the dense, ion conducting electrolyte must be compatible with the porous electrode to allow H_2 and O_2 permeation while electrons pass to the external load. The crucial materials issue is for the anode to be stable in a reducing environment, while the cathode remains inert in an oxidizing atmosphere. Moreover, both must have excellent contact with the electrolyte without the formation of low-conductivity phases.[32,199] A feasibility study of electrolyte-electrode modules stacked in series in planar or tubular configurations, and including the interconnect materials and fuel cell sealing, will be required.[200,201] In addition, durability and reliability studies involving mechanical and thermal stress and creep at high operating temperatures should be completed to ensure the longevity of the fuel cell.[202]

An ultimate SOFC might incorporate single crystal electrolytes, grown using fluxes, direct melting, high pressure or Czochralski processes, and can be considered as an option for preparing dense apatite electrolyte that optimally exploit anisotropic *c*-axis conductivity. While this concept cell could prove prohibitively expensive in commercial production, valuable insights into device fabrication may result.

References

1. S. P. S. Badwal and K. Foger, *Ceram. Int.*, 1996, **22**, 257-265.
2. S. Nakayama, H. Aono and Y. Sadaoka, *Chem. Lett.*, 1995, **24**, 431-432.
3. P. R. Slater, J. E. H. Sansom and J. R. Tolchard, *Chem. Rec.*, 2004, **4**, 373-384.
4. T. Ohnuki, N. Kozai, M. Samadfam, R. Yasuda, S. Yamamoto, K. Narumi, H. Naramoto and T. Murakami, *Chem. Geol.*, 2004, **211**, 1-14.
5. A. Smahi, A. Solhy, H. El Badaoui, A. Amoukal, A. Tikad, M. Maizi and S. Sebti, *Appl. Catal. A-Gen.*, 2003, **250**, 151-159.
6. H. Oonishi, *Biomaterials*, 1991, **12**, 171-178.
7. M. Røkkum and A. Reigstad, *J. Arthroplasty*, 1999, **14**, 689-700.
8. A. S. Karpov, J. Nuss, M. Jansen, P. E. Kazin and Y. D. Tretyakov, *Solid State Sci.*, 2003, **5**, 1277-1283.
9. S. Nakayama, T. Kageyama, H. Aono and Y. Sadaoka, *J. Mater. Chem.*, 1995, **5**, 1801-1805.
10. S. Nakayama and M. Sakamoto, *J. Eur. Ceram. Soc.*, 1998, **18**, 1413-1418.
11. S. Nakayama and M. Sakamoto, *J. Mater. Sci. Lett.*, 2001, **20**, 1627-1629.
12. P. Berastegui, S. Hull, F. J. G. Garcia and J. Grins, *J. Solid State Chem.*, 2002, **168**, 294-305.
13. J. Sansom, L. Hildebrandt and P. Slater, *Ionics*, 2002, **8**, 155-160.
14. L. León-Reina, M. C. Martín-Sedeño, E. R. Losilla, A. Cabeza, M. Martínez-Lara, S. Bruque, F. M. B. Marques, D. V. Sheptyakov and M. A. G. Aranda, *Chem. Mater.*, 2003, **15**, 2099-2108.
15. P. R. Slater and J. E. H. Sansom, *Solid State Phenom.*, 2003, **90-91**, 195-200.
16. E. Kendrick, M. S. Islam and P. R. Slater, *J. Mater. Chem.*, 2007, **17**, 3104-3111.
17. E. J. Abram, C. A. Kirk, D. C. Sinclair and A. R. West, *Solid State Ionics*, 2005, **176**, 1941-1947.
18. S. Célérier, C. Laberty, F. Ansart, P. Lenormand and P. Stevens, *Ceram. Int.*, 2006, **32**, 271-276.
19. S. Tao and J. T. S. Irvine, *Mater. Res. Bull.*, 2001, **36**, 1245-1258.

20. Y. Masubuchi, M. Higuchi, T. Takeda and S. Kikkawa, *J. Alloy Compd.*, 2006, **408-412**, 641-644.
21. A. Onda, S. Ogo, K. Kajiyoshi and K. Yanagisawa, *Mater. Lett.*, 2008, **62**, 1406-1409.
22. R. Ternane, M. Ferid, N. Kbir-Ariguib and M. Trabelsi-Ayedi, *J. Alloy Compd.*, 2000, **308**, 83-86.
23. S. Ferdov, R. A. S. Ferreira and Z. Lin, *Chem. Mater.*, 2006, **18**, 5958-5964.
24. X. Guo and P. Xiao, *J. Eur. Ceram. Soc.*, 2006, **26**, 3383-3391.
25. T. White, C. Ferraris, J. Kim and S. Madhavi, in *Reviews in Mineralogy and Geochemistry*, eds. G. Ferraris and S. Merlino, Mineralogy Society of America, Washington, DC, 2005, vol. 57, pp. 307-401.
26. H. R. Low, N. Phonthammachai, A. Maignan, G. A. Stewart, T. J. Bastow, L. L. Ma and T. J. White, *Inorg. Chem.*, 2008, **47**, 11774-11782.
27. R. R. Rao, H. N. Roopa and T. S. Kannan, *J. Mater. Sci.-Mater. M.*, 1997, **8**, 511-518.
28. S. S. Pramana, W. T. Klooster and T. J. White, *J. Solid State Chem.*, 2008, **181**, 1717-1722.
29. J. R. Tolchard, M. S. Islam and P. R. Slater, *J. Mater. Chem.*, 2003, **13**, 1956-1961.
30. S. Nakayama and M. Higuchi, *J. Mater. Sci. Lett.*, 2001, **20**, 913-915.
31. Energy Information Administration, Washington DC, 2008
32. N. Q. Minh, *J. Am. Ceram. Soc.*, 1993, **76**, 563-588.
33. M. C. Williams, J. P. Strakey, W. A. Surdoval and L. C. Wilson, *Solid State Ionics*, 2006, **177**, 2039-2044.
34. J. W. Fergus, *J. Power Sources*, 2006, **162**, 30-40.
35. K. Sasaki, K. Watanabe, K. Shiosaki, K. Susuki and Y. Teraoka, *J. Electroceram.*, 2004, **13**, 669-675.
36. P. Singh and N. Q. Minh, *Int. J. Appl. Ceram. Technol.*, 2004, **1**, 5-15.
37. S. C. Singhal, *Solid State Ionics*, 2002, **152-153**, 405-410.
38. H. Tu and U. Stimming, *J. Power Sources*, 2004, **127**, 284-293.
39. R. Bove and S. Ubertini, *J. Power Sources*, 2006, **159**, 543-559.
40. V. V. Kharton, F. M. B. Marques and A. Atkinson, *Solid State Ionics*, 2004, **174**, 135-149.
41. C. Haering, A. Roosen and H. Schichl, *Solid State Ionics*, 2005, **176**, 253-259.

42. S. P. S. Badwal, F. T. Ciacchi and D. Milosevic, *Solid State Ionics*, 2000, **136-137**, 91-99.
43. R. Shannon, *Acta Crystallogr. A*, 1976, **32**, 751-767.
44. H. Y. Tu, W. Y. Sun, Y. J. Yang, Z. Y. Lu, D. Q. Wang and T. L. Wen, *J. Eur. Ceram. Soc.*, 2000, **20**, 2421-2425.
45. K. Wiik, C. R. Schmidt, S. Faaland, S. Shamsili, M.-A. Einarsrud and T. Grande, *J. Am. Ceram. Soc.*, 1999, **82**, 721-728.
46. G. Stochniol, E. Syskakis and A. Naoumidis, *J. Am. Ceram. Soc.*, 1995, **78**, 929-932.
47. D. Kuscer, J. Holc, M. Hrovat, S. Bernik, Z. Samardzija and D. Kolar, *Solid State Ionics*, 1995, **78**, 79-85.
48. H. Inaba and H. Tagawa, *Solid State Ionics*, 1996, **83**, 1-16.
49. B. Dalslet, P. Blennow, P. Hendriksen, N. Bonanos, D. Lybye and M. Mogensen, *J. Solid State Electrochem.*, 2006, **10**, 547-561.
50. H. Yahiro, K. Eguchi and H. Arai, *Solid State Ionics*, 1989, **36**, 71-75.
51. J. M. Ralph, A. C. Schoeler and M. Krumpelt, *J. Mater. Sci.*, 2001, **36**, 1161-1172.
52. J. M. Ralph, C. Rossignol and R. Kumar, *J. Electrochem. Soc.*, 2003, **150**, A1518-A1522.
53. S. Charojrochkul, K.-L. Choy and B. C. H. Steele, *Solid State Ionics*, 1999, **121**, 107-113.
54. A. V. Joshi, J. J. Steppan, D. M. Taylor and S. Elangovan, *J. Electroceram.*, 2004, **13**, 619-625.
55. N. Liu, M. Shi, C. Wang, Y. Yuan, P. Majewski and F. Aldinger, *J. Mater. Sci.*, 2006, **41**, 4205-4213.
56. J. W. Stevenson, T. R. Armstrong, D. E. McCready, L. R. Pederson and W. J. Weber, *J. Electrochem. Soc.*, 1997, **144**, 3613-3620.
57. J. W. Stevenson, T. R. Armstrong, L. R. Pederson, J. Li, C. A. Lewinsohn and S. Baskaran, *Solid State Ionics*, 1998, **113-115**, 571-583.
58. J. W. Stevenson, K. Hasinska, N. L. Canfield and T. R. Armstrong, *J. Electrochem. Soc.*, 2000, **147**, 3213-3218.
59. D. W. Strickler and W. G. Carlson, *J. Am. Ceram. Soc.*, 1964, **47**, 122-127.
60. D. K. Hohnke, *J. Phys. Chem. Solids*, 1980, **41**, 777-784.

61. O. Yamamoto, Y. Arati, Y. Takeda, N. Imanishi, Y. Mizutani, M. Kawai and Y. Nakamura, *Solid State Ionics*, 1995, **79**, 137-142.

62. A. Sin, Y. Dubitsky, A. Zaopo, A. S. Arico, L. Gullo, D. La Rosa, S. Siracusano, V. Antonucci, C. Oliva and O. Ballabio, *Solid State Ionics*, 2004, **175**, 361-366.

63. S. J. Hong, K. Mehta and A. V. Virkar, *J. Electrochem. Soc.*, 1998, **145**, 638-647.

64. S. S. Pramana, T. J. White, M. K. Schreyer, C. Ferraris, P. R. Slater, A. Orera, T. J. Bastow, S. Mangold, S. Doyle, T. Liu, A. Fajar, M. Srinivasan and T. Baikie, *Dalton Trans.*, 2009, 8280-8291.

65. J. E. H. Sansom and P. R. Slater, *Solid State Ionics*, 2004, **167**, 23-27.

66. L. León-Reina, E. R. Losilla, M. Martínez-Lara, M. C. Martín-Sedeño, S. Bruque, P. Núñez, D. V. Sheptyakov and M. A. G. Aranda, *Chem. Mater.*, 2005, **17**, 596-600.

67. D. Mazza and S. Ronchetti, *Mater. Res. Bull.*, 1999, **34**, 1375-1382.

68. R. E. Ouenzerfi, C. Goutaudier, G. Panczer, B. Moine, M. T. Cohen-Adad, M. Trabelsi-Ayedi and N. Kbir-Ariguib, *Solid State Ionics*, 2003, **156**, 209-222.

69. M. Higuchi, Y. Masubuchi, S. Nakayama, S. Kikkawa and K. Kodaira, *Solid State Ionics*, 2004, **174**, 73-80.

70. I. A. Bondar and M. A. Petrova, *Inorg. Mater.*, 1970, **6**, 1128.

71. N. G. Gutkina, I. I. Kozhina and L. K. Shmatock, *Inorg. Mater.*, 1971, **7**, 1228.

72. NIST, *Phase Diagrams for Ceramists*, American Ceramic Society.

73. E. M. Levin, *J. Am. Ceram. Soc.*, 1974, **57**, 189-190.

74. A. S. Povarennykh, Plenum Press, New York/London, 1972, pp. 541-542.

75. T. J. White and D. ZhiLi, *Acta Crystallogr. B*, 2003, **59**, 1-16.

76. T. Baikie, M. M. Elcombe, P. H. J. Mercier, J. Y. Kim, Y. Le Page, L. D. Mitchell, T. J. White and P. S. Whitfield, *Acta Crystallogr. B*, 2007, **63**, 251-256.

77. Z. Dong and T. J. White, *Acta Crystallogr. B*, 2004, **60**, 146-154.

78. M. I. Kay and R. A. Young, *Nature*, 1964, **204**, 1050-1052.

79. Y.-S. Dai, J. M. Hughes and P. B. Moore, *Can. Mineral.*, 1991, **29**, 369-376.

80. H. Effenberger and F. Pertlik, *Tschermaks Min. Petr. Mitt.*, 1979, **26**, 95-107.

81. T. Baikie, C. Ferraris, W. T. Klooster, S. Madhavi, S. S. Pramana, A. Pring, G. Schmidt and T. J. White, *Acta Crystallogr. B*, 2008, **64**, 34-41.

82. M. E. Koumiri, S. Oishi, S. Sato, L. E. Ammari and B. Elouadi, *Mater. Res. Bull.*, 2000, **35**, 503-513.

83. T. Naddari, H. El Feki, J. M. Savariault, P. Salles and A. B. Salah, *Solid State Ionics*, 2003, **158**, 157-166.

84. M. Azrour, L. El Ammari, Y. Le Fur and B. Elouadi, *J. Solid State Chem.*, 1998, **141**, 373-377.

85. D.-H. Kang, J. Wontcheu and T. Schleid, *Solid State Sci.*, 2009, **11**, 299-304.

86. P. J.-P. Besse, G. Baud, G. Levasseur and R. Chevalier, *Acta Crystallogr. B*, 1979, **35**, 1756-1759.

87. A. Vegas and M. Jansen, *Acta Crystallogr. B*, 2002, **58**, 38-51.

88. H. E. Feki, J. M. Savariault and A. B. Salah, *J. Alloy Compd.*, 1999, **287**, 114-120.

89. L. León-Reina, E. R. Losilla, M. Martínez-Lara, S. Bruque and M. A. G. Aranda, *J. Mater. Chem.*, 2004, **14**, 1142-1149.

90. L. León-Reina, J. M. Porras-Vázquez, E. R. Losilla and M. A. G. Aranda, *Solid State Ionics*, 2006, **177**, 1307-1315.

91. L. León-Reina, E. R. Losilla, M. Martínez-Lara, S. Bruque, A. Llobet, D. V. Sheptyakov and M. A. G. Aranda, *J. Mater. Chem.*, 2005, **15**, 2489-2498.

92. Y. Masubuchi, M. Higuchi, T. Takeda and S. Kikkawa, *Solid State Ionics*, 2006, **177**, 263-268.

93. H. Okudera, Y. Masubuchi, S. Kikkawa and A. Yoshiasa, *Solid State Ionics*, 2005, **176**, 1473-1478.

94. E. Kendrick and P. R. Slater, *Mater. Res. Bull.*, 2008, **43**, 2509-2513.

95. M. O'Keeffe and B. G. Hyde, *Struct. Bonding*, 1985, **61**, 77-144.

96. A. Vegas, A. Romero and M. Martínez-Ripoll, *Acta Crystallogr.*, 1991, **47**, 17-23.

97. H. Wondratschek, L. Merker and K. Schubert, *Z. Kristallogr.*, 1964, **120**, 393-395.

98. M. S. Schriewer and W. Jeitschko, *J. Solid State Chem.*, 1993, **107**, 1-11.

99. T. Yamanaka, N. Hirai and Y. Komatsu, *Am. Mineral.*, 2002, **87**, 1183-1189.

100. A. Orera and P. R. Slater, *Solid State Ionics*, 2010, **181**, 110-114.

101. P. S. Whitfield, Y. L. Page, P. H. J. Mercier and J. Y. Kim, *J. Appl. Crystallogr.*, 2007, **40**, 1019-1026.

102. T. Baikie, S. S. Pramana, C. Ferraris, Y. Huang, E. Kendrick, K. S. Knight, Z. Ahmad and T. J. White, *Acta Crystallogr B.*, 2010, **66**, 1-16.

103. M. Pasero, A. R. Kampf, C. Ferraris, I. V. Pekov, J. Rakovan and T. J. White, *Eur. J. Mineral*, 2010, **22**, 163-179.

104. G. Giuseppetti, G. Rossi and C. Tadini, *Am. Mineral.*, 1971, **56**, 1174-1179.

105. J. E. H. Sansom, J. R. Tolchard, M. S. Islam, D. Apperley and P. R. Slater, *J. Mater. Chem.*, 2006, **16**, 1410-1413.

106. S. R. Hui, J. Roller, S. Yick, X. Zhang, C. Deces-Petit, Y. Xie, R. Maric and D. Ghosh, *J. Power Sources*, 2007, **172**, 493-502.

107. K. Yamashita, H. Owada, T. Umegaki, T. Kanazawa and T. Futagami, *Solid State Ionics*, 1988, **28-30**, 660-663.

108. S. Nakayama, M. Sakamoto, M. Higuchi, K. Kodaira, M. Sato, S. Kakita, T. Suzuki and K. Itoh, *J. Eur. Ceram. Soc.*, 1999, **19**, 507-510.

109. J. Felsche, *J. Solid State Chem.*, 1972, **5**, 266-275.

110. J. E. H. Sansom, E. Kendrick, J. R. Tolchard, M. S. Islam and P. R. Slater, *J. Solid State Electrochem.*, 2006, **10**, 562-568.

111. H. Arikawa, H. Nishiguchi, T. Ishihara and Y. Takita, *Solid State Ionics*, 2000, **136-137**, 31-37.

112. S. Lambert, A. Vincent, E. Bruneton, S. Beaudet-Savignat, F. Guillet, B. Minot and F. Bouree, *J. Solid State Chem.*, 2006, **179**, 2602-2608.

113. J. P. Besse, G. Baud, R. Chevalier and J. Zarembowitch, *Mat. Res. Bull*, 1980, **15**, 1255-1261.

114. J. R. Tolchard, J. E. H. Sansom, M. S. Islam and P. R. Slater, *Dalton Trans.*, 2005, 1273-1280.

115. S. Célérier, C. Laberty-Robert, J. W. Long, K. A. Pettigrew, R. M. Stroud, D. R. Rolison, F. Ansart and P. Stevens, *Adv. Mater.*, 2006, **18**, 615-618.

116. M. Dilip, Literature Seminar, The University of Alabama, Department of Chemistry, 2004.

117. D. E. Cox and A. P. Wilkinson, Elsevier Science, 1994, pp. 195-219.

118. C. Ferraris, T. White, J. Plévert and R. Wegner, *Phys. Chem. Minerals*, 2005, **32**, 485-492.

119. P. A. Stadelmann, *Ultramicroscopy*, 1987, **21**, 131-146.

120. S. Hovmoller, *Ultramicroscopy*, 1992, **41**, 121-135.
121. H. M. Rietveld, *Acta Crystallogr.*, 1967, **22**, 151-152.
122. H. Rietveld, *J. Appl. Crystallogr.*, 1969, **2**, 65-71.
123. Bruker, Bruker AXS Inc., Madison, Wisconsin, USA, 2005.
124. R. W. Cheary and A. Coelho, *J. Appl. Crystallogr.*, 1992, **25**, 109-121.
125. R. A. Young, *The Rietveld Method*, Oxford University Press, New York, 1993.
126. T. Iwata, K. Fukuda, E. Bechade, O. Masson, I. Julien, E. Champion and P. Thomas, *Solid State Ionics*, 2007, **178**, 1523-1529.
127. A. C. Larson and R. B. V. Dreele, *General Structure Analysis System (GSAS)*, Los Alamos National Laboratory, Los Alamos, 2004.
128. J. Gonzales-Platas and J. Rodriguez-Carvajal, Universidad de la Laguna, Tenerife, Spain, 2006.
129. J. Rodriguez-Carvajal, in *Abstracts of the Satellite Meeting on Powder Diffraction of the XVth Congress of the International Union of Crystallography, 127*, Toulouse, 1990.
130. S. S. Pramana, W. T. Klooster and T. J. White, *Acta Crystallogr. B*, 2007, **63**, 597-602.
131. T. Ressler, *J. Phys. IV*, 1997, **7**, C2-269-270.
132. I. Rehman and W. Bonfield, *J. Mater. Sci-Mater. M.*, 1997, **8**, 1-4.
133. P. Hartmann, C. Jäger, S. Barth, J. Vogel and K. Meyer, *J. Solid State Chem.*, 2001, **160**, 460-468.
134. E. Rodriguez-Reyna, A. F. Fuentes, M. Maczka, J. Hanuza, K. Boulahya and U. Amador, *Solid State Sci.*, 2006, **8**, 168-177.
135. A. Orera, E. Kendrick, D. C. Apperley, V. M. Orera and P. R. Slater, *Dalton Trans.*, 2008, 5296-5301.
136. Q.-A. Huang, R. Hui, B. Wang and J. Zhang, *Electrochim. Acta*, 2007, **52**, 8144-8164.
137. J. E. Bauerle, *J. Phys. Chem. Solids*, 1969, **30**, 2657-2670.
138. J. R. Macdonald, *Impedance spectroscopy emphasizing solid state materials and systems*, Wiley, New York, 1987.
139. J. E. H. Sansom, D. Richings and P. R. Slater, *Solid State Ionics*, 2001, **139**, 205-210.
140. A. Chesnaud, G. Dezanneau, C. Estournès, C. Bogicevic, F. Karolak, S. Geiger and G. Geneste, *Solid State Ionics*, 2008, **179**, 1929-1939.

141. B. G. Dick and A. W. Overhauser, *Phys. Rev.*, 1958, **112**, 90-103.
142. N. F. Mott and M. J. Littleton, *Trans. Faraday Soc.*, 1938, **34**, 485-499.
143. P. W. M. Jacobs and E. A. Kotomin, *J. Solid State Chem.*, 1993, **106**, 27-34.
144. E. Kendrick, M. S. Islam and P. R. Slater, *Chem. Commun.*, 2008, **8**, 715-717.
145. J. D. Gale, *J. Chem. Soc., Faraday Trans.*, 1997, **93**, 629-637.
146. G. Donnay and R. Allmann, *Am. Mineral.*, 1970, **55**, 1003-1015.
147. I. D. Brown, *The chemical bond in inorganic chemistry - the bond valence model*, Oxford University Press, New York, 2002.
148. S. Adams, *Acta Crystallogr. B*, 2001, **57**, 278-287.
149. N. E. Brese and M. O'Keeffe, *Acta Crystallogr. B*, 1991, **47**, 192-197.
150. I. D. Brown and D. Altermatt, *Acta Crystallogr. B*, 1985, **41**, 244-247.
151. S. Adams, *Solid State Ionics*, 2006, **177**, 1625-1630.
152. S. Adams, *J. Power Sources*, 2006, **159**, 200-204.
153. S. Adams and J. Maier, *Solid State Ionics*, 1998, **105**, 67-74.
154. L. León-Reina, J. M. Porras-Vázquez, E. R. Losilla and M. A. G. Aranda, *J. Solid State Chem.*, 2007, **180**, 1250-1258.
155. V. V. Kharton, A. L. Shaula, M. V. Patrakeev, J. C. Waerenborgh, D. P. Rojas, N. P. Vyshatko, E. V. Tsipis, A. A. Yaremchenko and F. M. B. Marques, *J. Electrochem. Soc.*, 2004, **151**, A1236-A1246.
156. Z. Dong and T. J. White, *Acta Crystallogr. B*, 2004, **60**, 138-145.
157. P. H. J. Mercier, Y. Le Page, P. S. Whitfield, L. D. Mitchell, I. J. Davidson and T. J. White, *Acta Crystallogr. B*, 2005, **61**, 635-655.
158. P. H. J. Mercier, Y. Le Page, P. S. Whitfield and L. D. Mitchell, *J. Appl. Crystallogr.*, 2006, **39**, 369-375.
159. J. R. Tolchard, P. R. Slater and M. S. Islam, *Adv. Funct. Mater.*, 2007, **17**, 2564-2571.
160. J. McFarlane, S. Barth, M. Swaffer, J. Sansom and P. Slater, *Ionics*, 2002, **8**, 149-154.
161. G. Laudisio and M. Catauro, *J. Eur. Ceram. Soc.*, 1998, **18**, 359-362.
162. Z. Lodziana, K. Parlinski and J. Hafner, *Phys. Rev. B*, 2001, **63**, 1341061-1341067.
163. E. F. Brès, J. C. Voegel, J. C. Barry, W. G. Waddington and R. M. Frank, *J. Appl. Crystallogr.*, 1986, **19**, 168-173.
164. D. M. Jones, *Acta Crystallogr. B*, 2007, **63**, 69-74.

165. B. Rowda, M. Avdeev, P. L. Lee, P. F. Henry and C. D. Ling, *Acta Crystallogr. B*, 2008, **64**, 154-159.

166. M. Yashima and R. Ali, *Solid State Ionics*, 2009, **180**, 120-126.

167. W. Yao, Z. Tang, Z. Zhang, S. Luo, J. Li and Q. Tan, *Mat. Sci. Eng. B-Solid*, 2003, **99**, 309-312.

168. P. R. Slater, J. T. S. Irvine, T. Ishihara and Y. Takita, *J. Solid State Chem.*, 1998, **139**, 135-143.

169. J. R. Tolchard and P. R. Slater, *J. Phys. Chem. Solids*, 2008, **69**, 2433-2439.

170. E. Kendrick, A. Orera and P. R. Slater, *J. Mater. Chem.*, 2009, **19**, 7955-7958.

171. S. Nakayama, M. Sakamoto, M. Higuchi and K. Kodaira, *J. Mater. Sci. Lett*, 2000, **19**, 91-93.

172. S. W. Tao and J. T. S. Irvine, *Ionics*, 2000, **6**, 389-396.

173. L. W. Schroeder and M. Mathew, *J. Solid State Chem.*, 1978, **26**, 383-387.

174. H. Takeda, M. Ohgaki, T. Kizuki, K. Hashimoto, Y. Toda, S. Udagawa and K. Yamashita, *J. Am. Ceram. Soc.*, 2000, **83**, 2884-2886.

175. E. Kendrick and P. R. Slater, *Solid State Ionics*, 2008, **179**, 981-984.

176. J. R. Tolchard, J. E. H. Sansom, P. R. Slater and M. S. Islam, *J. Solid State Electrochem.*, 2004, **8**, 668-673.

177. S. Beaudet-Savignat, A. Vincent, S. Lambert and F. Gervais, *J. Mater. Chem.*, 2007, **17**, 2078-2087.

178. T. Lister and J. Renshaw, *Understanding chemistry for advanced level*, Nelson Thornes, Cheltenham, 2000.

179. M. S. Islam, J. R. Tolchard and P. R. Slater, *Chem. Commun.*, 2003, 1486-1487.

180. L. Pauling, *The nature of the chemical bond and the structure of molecules and crystals*, Cornell University, New York, 1960.

181. L. Pauling, *J. Am. Chem. Soc.*, 1932, **54**, 3570-3582.

182. A. L. Allred, *J. Inorg. Nucl. Chem.*, 1961, **17**, 215-221.

183. T. Nakao, A. Mineshige, M. Kobune, T. Yazawa and H. Yoshioka, *Solid State Ionics*, 2008, **179**, 1567-1569.

184. M. O'Keeffe and B. G. Hyde, *Acta Crystallogr. B*, 1978, **34**, 27-32.

185. P. B. Moore, *Am. Mineral.*, 1970, **55**, 1146-1166.

186. S. M. Stishov and S. V. Popova, *Geokhimiya*, 1961, **10**, 837.

187. R. J. P. Lyon, *Nature*, 1962, **196**, 266-267.

188. G. Serghiou, R. Boehler and A. Chopelas, *High Pressure Res.*, 2003, **23**, 49-53.

189. F. Werner and F. Kubel, *Mater. Lett.*, 2005, **59**, 3660-3665.

190. G. R. Redhammer and G. Roth, *Acta Crystallogr. C*, 2003, **59**, i120-i124.

191. R. P. Gunawardane, R. A. Howie and F. P. Glasser, *Acta Cryst.*, 1982, **B38**, 1564-1566.

192. Y. Waseda, *Anomalous X-ray Scattering for Materials Characterisation: atomic-scale structure determination*, Springer, 2002.

193. R. S. Howland, T. H. Geballe, S. S. Laderman, A. Fischer-Colbrie, M. Scott, J. M. Tarascon and P. Barboux, *Phys. Rev.*, 1989, **B39**, 9017-9027.

194. J. P. Attfield, *Nature*, 1990, **343**, 46-49.

195. J. M. Joubert, R. Černý, M. Latroche, A. Percheron-Guégan and K. Yvon, *J. Appl. Cryst.*, 1998, **31**, 327-332.

196. S. Nakayama, H. Aono and Y. Sadaoka, *Chem. Lett.*, 1995, **24**, 431-432.

197. S. Nakayama and M. Sakamoto, *J. Eur. Ceram. Soc.*, 1998, **18**, 1413-1418.

198. R. D. Shannon, *Acta Crystallogr. A*, 1976, **32**, 751-767.

199. N. Q. Minh, *Solid State Ionics*, 2004, **174**, 271-277.

200. K. C. Wincewicz and J. S. Cooper, *J. Power Sources*, 2005, **140**, 280-296.

201. P. A. Lessing, *J. Mater. Sci.*, 2007, **42**, 3465–3476.

202. H. Yokokawa, H. Tu, B. Iwanschitz and A. Mai, *J. Power Sources*, 2008, **182**, 400-412.

203. C. Giacovazzo, H. L. Monaco, G. Artioli, D. Viterbo, M. Milanesio, G. Ferraris, G. Gilli, P. Gilli, G. Zanotti and M. Catti, in *Fundamentals of Crystallography*, ed. C. Giacovazzo, Oxford University Press, New York, 2011.

204. M. d. Graef and M. E. McHenry, *Structure of materials: An introduction to crystallography, diffraction and symmetry*, Cambridge University Press, Cambridge, 2007.

205. T. Hahn and A. Looijenga-Vos, in *International Table for Crystallography*, ed. T. Hahn, Springer, Heidelberg, 2006, vol. A.

206. A. R. Verma and O. N. Srivastava, *Crystallography applied to solid state physics*, New Age International, New Delhi, 2005.

207. R. Mirman, *Point groups, space groups, crystals, molecules*, World Scientific Publishing, Singapore, 1999.

208. V. K. Pecharsky and P. Y. Zavalij, *Fundamentals of powder diffraction and structural characterization of materials*, Springer, New York, 2005.

209. M. M. Woolfson, *An introduction to X-ray crystallography*, Cambridge University Press, Cambridge, 1997.

210. J. Philibert, *Atom movements: diffusion and mass transport in solids*, Éditions de Physique, Les Ulis, 1991.

211. H. Mehrer, *Diffusion in solids: fundamentals, methods, materials, diffusion-controlled processes*, Springer, Berlin, 2007.

212. R. E. Newnham, *Properties of materials: anisotropy, symmetry, structure*, Oxford University Press, Oxford, 2005.

213. W. Gao and N. M. Sammes, *An introduction to electronic and ionic materials*, World Scientific Publishing, Singapore, 2000.

214. A. Putnis, *Introduction to mineral sciences*, Cambridge University Press, Cambridge, 2003.

APPENDIX A

Crystallographic Concepts

Crystals are composed of repeated patterns of atoms, ions or molecules whose arrangement conforms to one of the 14 Bravais lattice and extends as an infinite array (Table A-1).[203,204] The fundamental atomic motif which contains all the components of the repeat is known as the unit cell, or the smallest volume that fills space completely when translated three-dimensionally. The unit cell shape will conform to one of seven crystal systems. The Bravais lattices may be primitive (P), body centered (I), face centered (F) or base centred (C), such that the arrangement of atoms around the centre are identical to those around the origin of the unit cell.

Table A-1: Summary of the 7 crystal systems and 14 Bravais lattices.

Crystal system	Bravais lattices	Axes and interaxial angles
Cubic	P, I, F	$a = b = c$ $\alpha = \beta = \gamma = 90°$
Tetragonal	P, I	$a = b \neq c$ $\alpha = \beta = \gamma = 90°$
Orthorhombic	P, C, I, F	$a \neq b \neq c$ $\alpha = \beta = \gamma = 90°$
Trigonal	P (or R)	$a = b = c$ $\alpha = \beta = \gamma \neq 90°$
Hexagonal	P	$a = b \neq c$ $\alpha = \beta = 90°; \gamma = 120°$
Monoclinic	P, C	$a \neq b \neq c$ $\alpha = \gamma = 90° \neq \beta$
Triclinic	P	$a \neq b \neq c$ $\alpha \neq \beta \neq \gamma \neq 90°$

Three dimensional crystals can be constructed from one dimensional point groups and two dimensional plane groups (Table A-2). In a point group, objects are generated about a point;[205] for example, the crystallographic point group *m* generates objects related by a mirror. In two dimensional or plane symmetry, mirror lines and rotation points (2-, 3-, 4-, 6- fold) combine, as in 2*mm* where a diad rotation and two perpendicular mirror planes act together. These when related by periodic translations create four 2D crystal systems (oblique, rectangular, square and hexagonal); by way of illustration *p*2*mm* is a primitive plane group[204-206] that utilizes the point group 2*mm*. Moreover, the compound operation called glide (reflection plus translation) is produced. In 3D, the mirror lines and rotation points becomes mirror planes and rotation axes, and these can be combined to produce axial glide, double glide, screw axes, and inversion operations.

Table A-2: Relationships between crystal systems, point groups, and space groups.

Crystal systems (x7)	**Point groups (x 32)**	**Space groups (x 230)**
Triclinic	1	P1
	$\bar{1}$	$P\bar{1}$
Monoclinic	2	*P*2, *P*2$_1$, *C*2
	m	*Pm*, *Pc*, *Cm*, *Cc*
	2/*m*	*P*2/*m*, *P*2$_1$/*m*, *C*2/*m*, *P*2/*c*, *P*2$_1$/*c*, *C*2/*c*
Orthorhombic	222	*P*222, *P*222$_1$, *P*2$_1$2$_1$2, *P*2$_1$2$_1$2$_1$, *C*222$_1$, *C*222, *F*222, *I*222, *I*2$_1$2$_1$2$_1$
	*mm*2	*Pmm*2, *Pmc*2$_1$, *Pcc*2, *Pma*2, *Pca*2$_1$, *Pnc*2, *Pmn*2$_1$, *Pba*2, *Pna*2$_1$, *Pnn*2, *Cmm*2, *Cmc*2$_1$, *Ccc*2, *Amm*2, *Aem*2, *Ama*2, *Aea*2, *Fmm*2, *Fdd*2, *Imm*2, *Iba*2, *Ima*2
	mmm	*Pmmm*, *Pnnn*, *Pccm*, *Pban*, *Pmma*, *Pnna*, *Pmna*, *Pcca*, *Pbam*, *Pccn*, *Pbcm*, *Pnnm*, *Pmmn*, *Pbcn*, *Pbca*, *Pnma*, *Cmcm*, *Cmce*, *Cmmm*, *Cccm*, *Cmme*, *Ccce*, *Fmmm*, *Fddd*, *Immm*, *Ibam*, *Ibca*, *Imma*
Tetragonal	4	*P*4, *P*4$_1$, *P*4$_2$, *P*4$_3$, *I*4, *I*4$_1$
	$\bar{4}$	$P\bar{4}$, $I\bar{4}$
	4/*m*	*P*4/*m*, *P*4$_2$/*m*, *P*4/*n*, *P*4$_2$/*n*, *I*4/*m*, *I*4$_1$/*a*
	422	*P*422, *P*42$_1$2, *P*4$_1$22, *P*4$_1$2$_1$2, *P*4$_2$22, *P*4$_2$2$_1$2, *P*4$_3$22, *P*4$_3$2$_1$2, *I*422, *I*4$_1$22
	4*mm*	*P*4*mm*, *P*4*bm*, *P*4$_2$*cm*, *P*4$_2$*nm*, *P*4*cc*, *P*4*nc*, *P*4$_2$*mc*, *P*4$_2$*bc*, *I*4*mm*, *I*4*cm*, *I*4$_1$*md*, *I*4$_1$*cd*
	$\bar{4}$ 2*m*	$P\bar{4}2m$, $P\bar{4}2c$, $P\bar{4}2_1m$, $P\bar{4}2_1c$, $P\bar{4}m2$, $P\bar{4}c2$, $P\bar{4}b2$, $P\bar{4}n2$, $I\bar{4}m2$, $I\bar{4}c2$, $I\bar{4}2m$, $I\bar{4}2d$
	4/*mmm*	*P*4/*mmm*, *P*4/*mcc*, *P*4/*nbm*, *P*4/*nnc*, *P*4/*mbm*, *P*4/*mnc*, *P*4/*nmm*, *P*4/*ncc*, *P*4$_2$/*mmc*, *P*4$_2$/*mcm*, *P*4$_2$/*nbc*, *P*4$_2$/*nnm*, *P*4$_2$/*mbc*, *P*4$_2$/*mnm*, *P*4$_2$/*nmc*, *P*4$_2$/*ncm*, *I*4/*mmm*, *I*4/*mcm*, *I*4$_1$/*amd*, *I*4$_1$/*acd*
Trigonal	3	*P*3, *P*31, *P*32, *R*3
	$\bar{3}$	$P\bar{3}$, $R\bar{3}$
	32	*P*312, *P*321, *P*3$_1$12, *P*3$_1$21, *P*3$_2$12, *P*3$_2$21, *R*32
	3*m*	*P*3*m*1, *P*31*m*, *P*3*c*1, *P*31*c*, *R*3*m*, *R*3*c*
	$\bar{3}$ *m*	$P\bar{3}1m$, $P\bar{3}1c$, $P\bar{3}m1$, $P\bar{3}c1$, $R\bar{3}m$, $R\bar{3}c$
Hexagonal	6	*P*6, *P*6$_1$, *P*6$_5$, *P*6$_2$, *P*6$_4$, *P*6$_3$
	$\bar{6}$	$P\bar{6}$
	6/*m*	*P*6/*m*, *P*6$_3$/*m*
	622	*P*622, *P*6$_1$22, *P*6$_5$22, *P*6$_2$22, *P*6$_4$22, *P*6$_3$22
	6*mm*	*P*6*mm*, *P*6*cc*, *P*6$_3$*cm*, *P*6$_3$*mc*
	$\bar{6}$ *m*2	$P\bar{6}m2$, $P\bar{6}c2$, $P\bar{6}2m$, $P\bar{6}2c$
	6/*mmm*	*P*6/*mmm*, *P*6/*mcc*, *P*6$_3$/*mcm*, *P*6$_3$/*mmc*
Cubic	23	*P*23, *F*23, *I*23, *P*2$_1$3, *I*2$_1$3
	m $\bar{3}$	*Pm*$\bar{3}$, *Pn*$\bar{3}$, *Fm*$\bar{3}$, *Fd*$\bar{3}$, *Im*$\bar{3}$, *Pa*$\bar{3}$, *Ia*$\bar{3}$
	432	*P*432, *P*4$_2$32, *F*432, *F*4$_1$32, *I*432, *P*4$_3$32, *P*4$_1$32, *I*4$_1$32
	$\bar{4}$ 3*m*	$P\bar{4}3m$, $F\bar{4}3m$, $I\bar{4}3m$, $P\bar{4}3n$, $F\bar{4}3c$, $I\bar{4}3d$
	m $\bar{3}$ *m*	*Pm*$\bar{3}$*m*, *Pn*$\bar{3}$*n*, *Pm*$\bar{3}$*n*, *Pn*$\bar{3}$*m*, *Fm*$\bar{3}$*m*, *Fm*$\bar{3}$*c*, *Fd*$\bar{3}$*m*, *Fd*$\bar{3}$*c*, *Im*$\bar{3}$*m*, *Ia*$\bar{3}$*d*

There are 2 1D point groups, 10 2D point groups and 32 3D point groups. These can be described by:

- Hermann-Mauguin or Schoenflies symbols,
- Stereographic projections,
- Symmetry operation matrices, or
- Actual crystals, showing faceted drawings.

The combination of 3D symmetry operators, Bravais lattices and translations allow the construction of 230 space groups.[205,207-209]

APPENDIX B

Diffusion Basics

When there is a concentration gradient in a substance, diffusion will occur. In solids, diffusion (or migration) takes place when atoms or ions conduct from one lattice point to the other. This phenomenon is described by Fick's first law[210,211] of diffusion that in a steady-state condition is given as

$$J = -D\frac{\partial C}{\partial x}$$

where J, D and C is the flux, diffusion coefficient or diffusivity, and concentration, respectively. Diffusion coefficients depend on temperature according to the Arrhenius equation:

$$D = D_0 \exp\left(\frac{-Q}{kT}\right)$$

where Q is the activation energy, k the Boltzmann constant and T the absolute temperature, while D_0 is the diffusion pre-exponential factor.

Fick's second law[210,211] explains the time-dependence of concentration of the diffusing species:

$$\frac{\partial C}{\partial t} = \frac{\partial}{\partial x}\left(D\frac{\partial C}{\partial x}\right)$$

and when D is independent of composition, it becomes:

$$\frac{\partial C}{\partial t} = D\frac{\partial^2 C}{\partial x^2}$$

Atoms can diffuse via several mechanisms:[212,213]

1. *Vacancy mechanism* where an atom migrates to a neighbouring vacancy, and the total number of diffusing atoms in a specific direction equals the vacancies migrating oppositely;
2. *Interstitial mechanism* where much smaller foreign dopants diffuse from one interstitial site to the others;
3. *Interstitialcy mechanism* that combines vacancy and interstitial mechanisms;
4. *Direct exchange mechanism* when two atoms move simultaneously in opposite directions; and

5. *Ring mechanism* described as a rotation of three or more atoms as a group and the lattice distortion is very little compared to the others.

APPENDIX C

Anisotropy and Crystal Structures

In solid state chemistry, anisotropy is the attribute of displaying dissimilar properties (e.g. ionic conduction) in discrete directions. In a polycrystalline material, where the crystals are inherently anisotropic in some manner, but randomly oriented, a physical property will appear isotropic. However, the same substance when examined as a single crystal and with measurements carried out in principal crystallographic directions will be seen to possess anisotropic attributes. Variation in physical properties in a crystal as a function of direction must adhere to the point group symmetry, in what is known as Neumann's principle. For example, in the case of diffusion of Ni at 1150°C through a single crystal of orthorhombic $(Mg,Fe)_2SiO_4$ olivine, the diffusion coefficients are along *x, y* and *z* are[214]:

$$D_x = 4.40 \times 10^{-14} \text{ cm}^2/\text{s}$$
$$D_y = 3.35 \times 10^{-14} \text{ cm}^2/\text{s}$$
$$D_z = 124.0 \times 10^{-14} \text{ cm}^2/\text{s}$$

Another example of anisotropic crystal is graphite which has a layered crystal structure. Along the layered plane, the carbon – carbon bond is very strong with the interatomic distance of 1.42 Å. However, in-between layers, the C-C are weakly bonded with a distance of 3.35 Å. This intrinsic difference translates electrical properties and results in graphite being a metallic conductor parallel to the layers ($\rho = 5 \times 10^{-6}$ Ωm) and semiconductor perpendicular to the layers ($\rho = 5 \times 10^{-3}$ Ωm). In addition, the coefficient of thermal expansion is expected to be different with ~ 0 and 28.3×10^{-6} K^{-1} parallel and perpendicular to the layers, respectively.[214] Similarly, apatites and zeolites, that contain channel, exhibit anisotropic properties with respect to the channel directions. Specifically, ion conduction will be superior along the tunnels.[25]

Anisotropy is not only a property of crystals, but can also be induced by the external force, e.g. applied electric field. Chemical anisotropy strictly explains the different growth or dissolution rate of a crystal on specific lattice planes, and usually can be recognized by external morphology, as for example, in tabular or acicular shapes. The

general phenomenological rule is that fast-growing faces disappear, while the slow-growing faces remain. However, the final morphology is frequently altered by surface roughness, dangling bonds and surface layers of foreign atoms or molecules.[212]